THE UNIVERSITY *of* EDINBURGH

Building M^{III} Clusters with Derivatised Salicylaldoximes

Kevin Mason

A Thesis submitted for the degree of Doctor of Philosophy

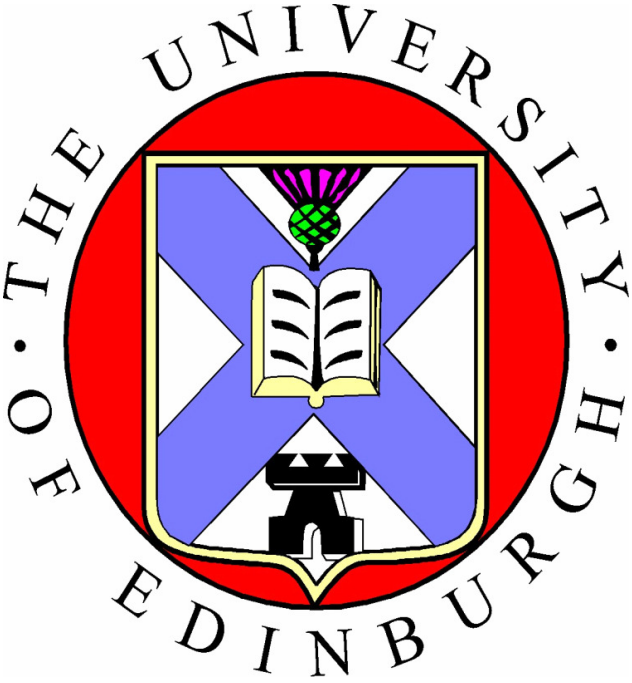

School of Chemistry

Faculty of Science and Engineering

University of Edinburgh

Edinburgh – January 2012

Abstract

This thesis describes the synthesis of a host of polynuclear iron complexes synthesised with phenolic oxime ligands, fundamentally developing the coordination chemistry of iron with these ligands. The metallic cores that occur within iron phenolic oxime clusters were found to contain almost exclusively oxo-centred triangles and oxo-centred tetrahedra. We found that we could alter the reaction conditions or derivatise the ligands and develop these basic building blocks into more elaborate arrays, exerting a degree of control over creating larger or smaller clusters. Chapter one describes the syntheses, structures and magnetic properties of new iron complexes alongside previously synthesised related complexes (**4**, **5**, **8**, **9** and **15**) containing salicylaldoxime ($saoH_2$) or derivatised salicylaldoximes (R-$saoH_2$). These are $[Fe_3O(OMe)(Ph\text{-}sao)_2Cl_2(py)_3]\cdot 2MeOH$ (**1**·2MeOH), $[Fe_3O(OMe)(Ph\text{-}sao)_2Br_2(py)_3]\cdot Et_2O$ (**2**·Et_2O), $[Fe_4(Ph\text{-}sao)_4F_4(py)_4]\cdot 1.5MeOH$ (**3**·1.5MeOH), $[Fe_6O_2(OH)_2(Et\text{-}sao)_2(Et\text{-}saoH)_2(O_2CPh)_6]$ (**4**), $[HNEt_3]_2[Fe_6O_2(OH)_2(Et\text{-}sao)_4(O_2CPh(Me)_2)_6]\cdot 2MeCN$ (**5**·2MeCN), $[Fe_6O_2(O_2CPh)_{10}(3\text{-}^tBut\text{-}5\text{-}NO_2\text{-}sao)_2(H_2O)_2]\cdot 2MeCN$ (**6**·2MeCN), $[Fe_6O_2(O_2CCH_2Ph)_{10}(3\text{-}^tBut\text{-}sao)_2(H_2O)_2]\cdot 5MeCN$ (**7**·5MeCN), $\{[Fe_6Na_3O(OH)_4(Me\text{-}sao)_6(OMe)_3(H_2O)_3(MeOH)_6]\cdot MeOH\}n$ (**8**·MeOH) and $[HNEt_3]_2[Fe_{12}Na_4O_2(OH)_8(sao)_{12}(OMe)_6(MeOH)_{10}]$ (**9**). The predominant building block appears to be the triangular $[Fe_3O(R\text{-}sao)_3]^+$ species which can self-assemble into more elaborate arrays depending on reaction conditions. The four hexanuclear and two octanuclear complexes of formulae $[Fe_8O_2(OMe)_4(Me\text{-}sao)_6Br_4(py)_4]\cdot 2Et_2O\cdot MeOH$ (**10**·2Et_2O·MeOH), $[Fe_8O_2(OMe)_{3.85}(N_3)_{4.15}(Me\text{-}sao)_6(py)_2]$ (**11**), $[Fe_6O_2(O_2CPh\text{-}4\text{-}NO_2)_4(Me\text{-}sao)_2(OMe)_4Cl_2(py)_2]$ (**12**), $[Fe_6O_2(O_2CPh\text{-}4\text{-}NO_2)_4(Et\text{-}sao)_2(OMe)_4Cl_2(py)_2]\cdot 2Et_2O\cdot MeOH$ (**13**·2Et_2O·MeOH), $[HNEt_3]_2[Fe_6O_2(Me\text{-}sao)_4(SO_4)_2(OMe)_4(MeOH)_2]$ (**14**) and $[HNEt_3]_2[Fe_6O_2(Et\text{-}sao)_4(SO_4)_2(OMe)_4(MeOH)_2]$ (**15**) all are built from series of edge-sharing $[Fe_4(\mu_4\text{-}O)]^{10+}$ tetrahedra. Complexes **10** and **11** display a new μ_4-coordination mode of the oxime ligand and join a small group of Fe-phenolic oxime complexes with nuclearity greater than six.

Chapter three then introduces co-ligands to the reaction scheme to compete with the salicylaldoxime ligands for metal coordination sites. Five tetranuclear and two nononuclear complexes are stabilised with salicylaldoxime ($saoH_2$) or derivatised salicylaldoximes (R-$saoH_2$) in conjunction with either 1,4,7-triazocyclononane (tacn), 2-hydroxymethyl pyridine (hmpH) or 2,6-pyridine dimethanol ($pdmH_2$), $[Fe_4O_2(sao)_4(tacn)_2]\cdot 2MeOH$ (**16**·MeOH), $[Fe_4O_2(Me\text{-}sao)_4(tacn)_2]\cdot 2MeCN$ (**17**·2MeCN), $[Fe_4O_2(Et\text{-}sao)_4(tacn)_2]\cdot MeOH$ (**18**·MeOH), $[Fe_9NaO_4(Et\text{-}sao)_6(hmp)_8]\cdot 3MeCN\cdot Et_2O$ (**19**·3MeCN·Et_2O), $[Fe_4(Et\text{-}sao)_4(hmp)_4]\cdot Et\text{-}saoH_2$ (**20**·Et-$saoH_2$), $[Fe_4(Ph\text{-}sao)_4(hmp)_4]\cdot 2MeCN$ (**21**·2MeCN) $[Fe_9O_3(sao)(pdm)_6(N_3)_7(H_2O)]$ (**22**).

Chapter four straps two salicylaldoxime units together in the 3-position, using ligands with aliphatic α,Ω-aminomethyl links, allowing the assembly of the polynuclear complexes $[Fe_7O_2(OH)_6(H_2L1)_3(py)_6](BF_4)_5\cdot 6H_2O\cdot 14MeOH$ (**23**·$6H_2O$·14MeOH), $[Fe_6O(OH)_7(H_2L2)_3][(BF_4)_3]\cdot 4H_2O\cdot 9MeOH$ (**24**·$4H_2O$·9MeOH) and $[Mn_6O_2(OH)_2(H_2L1)_3(py)_4(MeCN)_2](BF_4)_5(NO_3)\cdot 3MeCN\cdot H_2O\cdot 5py$ (**25**·3MeCN·H_2O·5py). In each case the metallic skeleton of the cluster is based on a trigonal prism in which two $[M^{III}{}_3O]$ triangles are tethered together *via* three helically twisted double-headed oximes. The latter are present as H_2L^{2-} in which the oximic and phenolic O-atoms are deprotonated and the amino N-atoms protonated, with the oxime moieties bridging across the edges of the metal triangles. Both the identity of the metal ion and the length of the straps connecting the salicylaldoxime units have a major impact on the nuclearity and topology of the resultant cage, with, perhaps counter-intuitively, the longer straps producing the "smallest" clusters.

Acknowledgements

I would like to begin by thanking my two supervisors, Prof. Euan Brechin and Prof. Peter Tasker. The encouragement and help Euan has provided from my final year project through to now has been truly remarkable and I must say a massive thank you to him for that. He has been a real pleasure to work for and has gone some way to changing my opinion of Aberdeen fans. Peter has been incredibly helpful with me as well, and I would like to say another massive thank you to him for everything he has done. I was constantly learning from him and can only hope that all the last minute stuff marked down as "character building" will leave me in good stead for the future. I have been very fortunate to have had two exceptional bosses supervising me.

I have worked with some great people throughout my PhD and will start by thanking former flatmate and fellow fire-fighter Ross Inglis, a big help at the start and always up for going big (even occasionally away from Opium). Thanks also go to Giorgos Karotsis for making the lab so lively and taking me to Greece; Alessandro Prescimone for putting up with all my structures (sorry again) and being so nice about it; Steph Taylor for always being good for a chat if I want a change from football; Tom Hooper for being our football teams only defender for 3 years (and only complaining once) and Sergio Sanz for livening up the place and flying the El Barrio flag on friday nights. The group has always been good and I will definitely miss working in it, you all know where to find me and you know you're more than welcome to visit.

The first person I met from the Tasker group upstairs was Dave Henderson and since then he was a great bastion of knowledge, always available for help and definitely left a *void* when he moved on. John Chang has been unbelievable with his efforts in making the organic ligands and I can't thank him enough. They along with the rest of the Tasker group of Matt, Jen, James, Ben and Karl have all been good fun and I always enjoy coming up on Friday afternoons to talk about serious chemistry and current affairs (I think that's what you call it!). I'd also like to thank anyone who has chosen to go big and not go home- it's always the right choice.

Thank you to the crystallography department of Simon Parsons, Anna Collins, Fraser White, Gary Nichol, Pete Byrne, Nick Funnell and Stephen “the pass master” Moggach. Thanks also to Alexandra Slawin at St. Andrews for one structure.

I must also thank the people at Silberline, who have all since left Silberline, David Aldous, Stewart Warrender, Rachel Cooper and Ian Wheeler.

Outside work done by Hiroyuki Nojiri and Stefano Carretta on the final chapter magnetism is very much appreciated.

Finally and most importantly I would like to thank my family, my dad, my mum, my brother Mark and my gran, I really appreciate everything you have done for me and the support you have shown. It’s not been the easiest thing to do and I couldn’t imagine having done it without you.

Declaration

I hereby declare that except where specific reference is made to other sources, the work contained in this thesis is the original work of the author. It has been composed by the candidate and has not been submitted, in whole or in part, for any other degree, diploma, or other qualification.

Kevin Mason

January 2012

Format of the Thesis

Each chapter of this thesis with the exception of chapter one is composed of published or to be published papers. To fulfil the requirements of the University of Edinburgh regarding the preparation and submission of a thesis for the degree of PhD, they have been reformatted accordingly.

Chapter 2

- K. Mason, I. A. Gass, S. Parsons, A. Collins, F. J. White, A. M. Z. Slawin, E. K. Brechin and P. A. Tasker, *Dalton Trans.*, 2010, 39, 2727.
- K. Mason, I. A. Gass, F. J. White, G. S. Papaefstathiou, E. K. Brechin and P. A. Tasker, *Dalton Trans.*, 2011, 40, 2875.

Chapter 3

- K. Mason, A. Prescimone, M. Schau-Magnussen, S. Piligkos, E. K. Brechin and P. A. Tasker, *Dalton Trans.*, 2012, In preparation.

Chapter 4

- K. Mason, J. Chang, E. Garlatti, A. Prescimone, S. Yoshii, H. Nojiri, J. Schnack, P. A. Tasker, S. Carretta and E. K. Brechin, *Chem. Commun.*, 2011, **47**, 6018.
- K. Mason, J. Chang, A. Prescimone, E. Garlatti, S. Carretta, P. A. Tasker and E. K. Brechin, *Dalton Trans.*, 2012, Submitted.

Measurements done by other people:

High field magnetic measurements performed by Hiroyuki Nojiri at Institute for Materials Research, Tohoku University.

Magnetic analysis on complexes **23**-**25** performed by Stefano Carretta at Dipartimento di Scienze Molecolari Applicate ai Biosistemi, Università di Milano

Publications

1 R. Inglis, L. F. Jones, **K. Mason**, A. Collins, S. A. Moggach, S. Parsons, S. P. Perlepes, W. Wernsdorfer and E. K. Brechin, *Chem. Eur. J.*, 2008, **14**, 9117.

2 L. F. Jones, R. Inglis, M. E. Cochrane, **K. Mason**, A. Collins, S. Parsons, S. P. Perlepes and E. K. Brechin, *Dalton Trans.*, 2008, **44**, 6205.

3 M. Wenzel, R. S. Forgan, A. Faure, **K. Mason**, P. A. Tasker, S. Piligkos, E. K. Brechin and P. G. Plieger, *Eur. J. Inorg. Chem.*, 2009, **2009**, 4613.

4 S. T. Meally, **K. Mason**, P. McArdle, E. K. Brechin, A. G. Ryder and L. F. Jones, *Chem. Commun.*, 2009, 7024.

5 **K. Mason**, I. A. Gass, S. Parsons, A. Collins, F. J. White, A. M. Z. Slawin, E. K. Brechin and P. A. Tasker, *Dalton Trans.*, 2010, **39**, 2727.

6 **K. Mason**, I. A. Gass, F. J. White, G. S. Papaefstathiou, E. K. Brechin and P. A. Tasker, *Dalton Trans.*, 2011, **40**, 2875.

7 **K. Mason**, J. Chang, E. Garlatti, A. Prescimone, S. Yoshii, H. Nojiri, J. Schnack, P. A. Tasker, S. Carretta and E. K. Brechin, *Chem. Commun.*, 2011, **47**, 6018.

8 **K. Mason**, A. Prescimone, M. Schau-Magnussen, S. Piligkos, E. K. Brechin and P. A. Tasker, *Dalton Trans.*, 2012, In preparation.

9 **K. Mason**, J. Chang, A. Prescimone, E. Garlatti, S. Carretta, P. A. Tasker and E. K. Brechin, *Dalton Trans.*, 2012, Submitted.

Conferences Attended

2010

- Scottish Dalton Meeting, (Glasgow, UK).
- ICMM 2010: The 12th International Conference on Molecule-based Magnets, (Beijing, China). *Poster presented.*

2011

- EICC-1: First EuCheMS Inorganic Chemistry Conference, (Manchester, UK).
- 94th Candian Chemistry Conference and Exhibition, (Montreal, Canada). *Poster Presented.*
- ECMM 2011: The 3rd European Conference on Molecular Magnetism, (Paris, France).

Contents

Abbreviations

ac	Alternating Current
AF	Antiferromagnetic Exchange
BVS	Bond Valence Sum
CCDC	Cambridge Crystallographic Data Centre
D	Zero Field Splitting Parameter
dc	Direct Current
FAB	Fast Atom Bombardment
hmpH	2-(hydroxymethyl)pyridine
Hr	Hemerythrin
INS	Inelastic Neutron Scattering
LRMS	Low Resolution Mass Spectrometry
MCE	Magnetocaloric Effect
MMO	Methane monooxygenase
μSR	Muon Spin Rotation
NMR	Nuclear Magnetic Resonance
P50	Acorga P5000 ligand
$pdmH_2$	2,6-pyridinedimethanol
py	Pyridine
QTM	Quantum Tunnelling of Magnetisation
RNR	Ribonucleotide reductase
$saoH_2$	Salicylaldoxime
s.e.	Symmetry Equivalent
SMM	Single Molecule Magnet
tacn	1,4,7-triazacyclononane

Chapter 1
Introduction

1.1 General aims of the thesis

The work in this thesis, partially funded by Silberline Ltd under a SPIRIT PhD studentship, concerns the synthesis and characterisation of polynuclear iron complexes of phenolic oxime ligands. The industrial partner's interest in these compounds arises from their potential application as pigmentary materials. There is also considerable interest in the magnetic properties of polynuclear complexes of phenolic oximes and in their formation when ligands of this type are used as corrosion inhibitors. The objectives of the work presented in the thesis are to define how the nuclearity and structures of iron (III) clusters can be varied using simple salicylaldoxime derivatives and "strapped" ligands in which two salicylaldoximes are linked to assemble larger clusters from smaller components.

The following sections of this chapter provide a brief review of the occurrence of polynuclear iron complexes within biology, in particular the attempts at modelling iron dimer sites in enzymes. A major factor of interest in these dinuclear iron compounds is their electronic structure and in particular delocalisation of electrons in the system. Such species also relate closely to understanding the origins of molecular magnetism. They provided an abundance of clusters whose magnetic properties could be studied; these properties are then discussed along with the role iron played in the development of important phenomena within molecular magnetism. The application of phenolic oxime ligands in industry is discussed, highlighting the corrosion inhibition of iron and how this might depend on the formation of stable polynuclear iron complexes.

1.2 Polynuclear iron complexes *in vivo*

Ferritins are iron-storage proteins found within most living organisms.[1, 2] They act as a reservoir for iron within the body of the organism, providing an available and soluble source (Fig. 1), effectively transporting pigmentary iron oxides. The problem of solubility appeared around 2.5 billion years ago when plants began to use H_2O as a source of hydrogen for photosynthesis. This created an O_2 by-product which would readily oxidise the soluble Fe^{II} into the relatively less soluble

Fe^{III}.[3] Organisms dependant on iron were now tasked with either moving to O_2 free areas or adapting to the lower solubility of Fe^{III}. They chose the latter and accommodated iron within a soluble shell membrane called apoferritin. This spherical shell is formed from 24 polypeptide chains and contains channels at the interfaces between neighbouring chains through which the iron can enter and exit. A central cavity of ~80 Å diameter is created and the mineral like core formed within can contain up to 4500 Fe^{III} centres in a $(FeOOH)_8FeO{\cdot}H_2PO_4$ form.[4]

The distinct role of the ferritin protein can vary in different cells, be it a specialized function such as recycling iron in macrophages or more general upkeep functions such as making iron available for cytochromes, nitrogenase, ribonucleotide reductase, hemoglobin myoglobin, etc.[5] Unusual versions of ferritin exist, for example *Listeria innocua* ferritin which is half the size of the general ferritin structure and can only contain ~500 Fe^{III} centres.[6] Synthesis of larger oxy-hydroxy stabilised iron clusters can thus give an insight into the formation of such systems within the core.[4, 7]

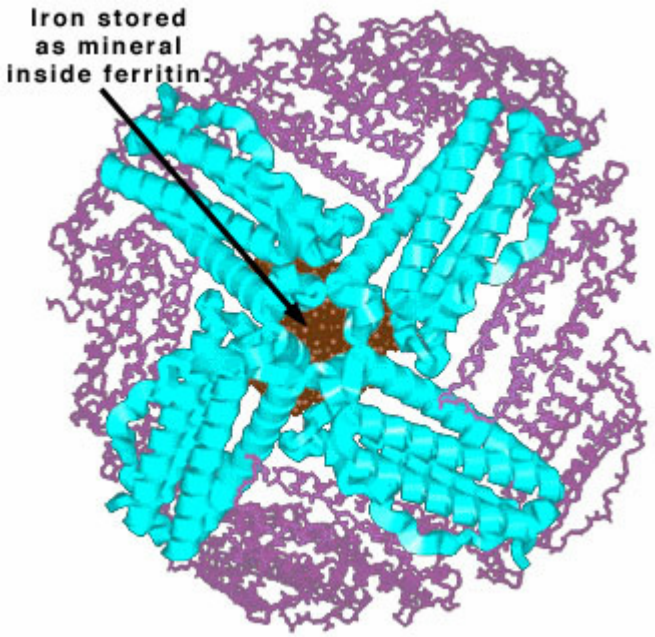

Fig. 1 The iron storage protein Ferritin.[8]

Smaller polynuclear clusters of iron are also important, particularly those containing dinuclear iron sites. Examples include methane monooxygenase, which can oxidise the C-H bond in methane to make methanol;[9] hemerythrin, which transports O_2 within certain marine invertebrates;[10, 11] and ribonucleotide reductase, a catalyst in the conversion of ribonucleotides to deoxyribonucleotides (precursors to DNA).[12]

Methane monooxygenase occurs within some bacterial entities in two forms, the soluble version (sMMO) and the particulate version (pMMO).[13] The active site within sMMO is an iron dimer[14] whereas pMMO has an active site with a copper dimer.[15] The three protein units contained in sMMO are hydroxylase (MMOH), the β unit (MMOB) and the reductase (MMOR). It is within MMOH that the diiron site is located; the molecular structure of its various forms can be seen in Fig. 2 along with a proposed mechanism by Basch et al.[16] It exists in a number of oxidation states, at rest it is present as [Fe^{III}-Fe^{III}] (MMOHox) but can reduce to [Fe^{II}-Fe^{III}] and [Fe^{II}-Fe^{II}]. The diferrous state [MMOHred] is the only one to react with the O_2 and starts the catalytic cycle. Upon reacting with O_2 it will form intermediate P and then readily convert to a high spin [Fe^{IV}-Fe^{IV}] intermediate Q.[17-19] It is here where the C-H bond in methane is activated preceding its oxidation to methanol and questions are raised concerning the exact mechanism.[16] Radical and non-radical routes are proposed and attempts to synthesise artificial analogues and map the reaction *via* spectroscopic techniques are ongoing.[20]

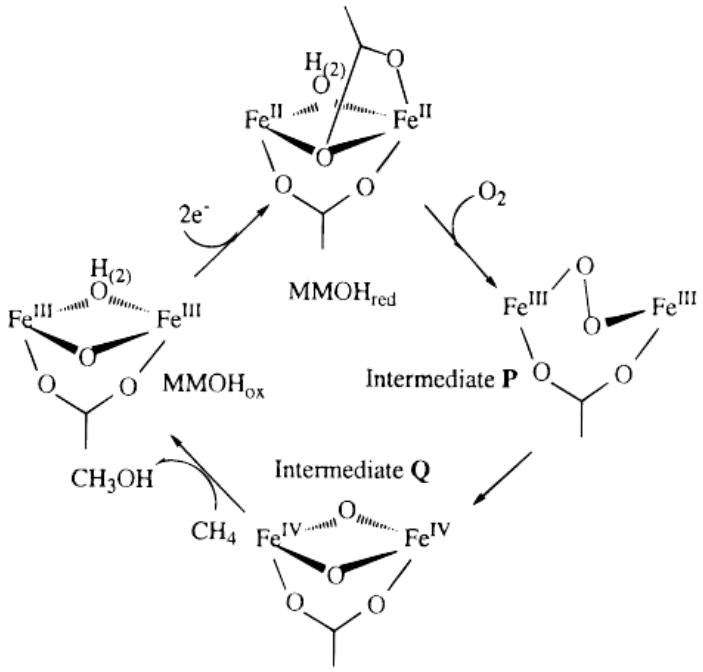

Fig. 2 The catalytic cycle of MMO.[16]

Found within a number of marine invertebrate phyla, hemerythrin (Fig. 3) is a protein responsible for O_2 transport.[21, 22] Despite the name and function it does not contain a heme group; instead it operates *via* a diiron core. When unbound to O_2 (deoxyHr) the two irons are linked through the carboxylate groups of glutamate and aspartate and a hydroxyl group. All the remaining coordination sites are taken up by the imidazole groups of histidine residues.[23] One Fe^{II} centre is in an octahedral geometry and the other is trigonal bipyramidal, it is at this five coordinate site that the reversible O_2 binding occurs. Rather than bind as the dioxygen ligand it is terminally bound as a hydroperoxide ligand, with the hydroxyl bridge between the Fe centres converted to a μ-O^{2-} ligand and then hydrogen bonded to the hydroperoxide,[24] the redox reaction can be seen in Fig. 3. In the oxygenated form (oxyHr) the iron centres are both ferric, six coordinate and in an octahedral geometry.

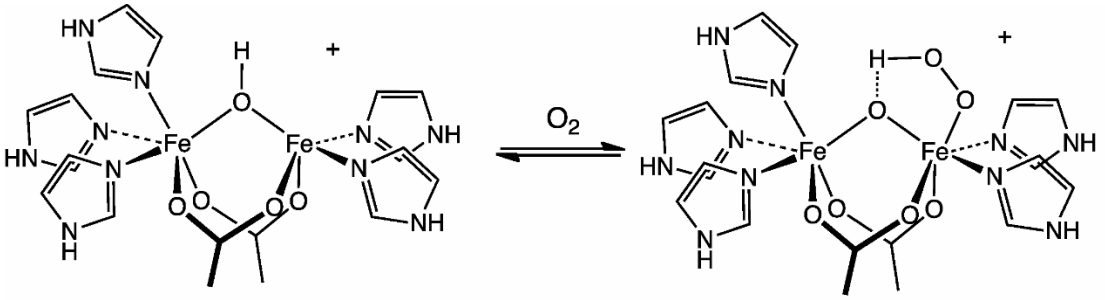

Fig. 3 Reversible O_2 transport reaction of Hemrythrin.[21]

The rate-determining step in the biosynthesis of DNA is the conversion of nucleotides to deoxynucleotides. The catalysts of this reaction are the ribonucleotide reductases (RNRs) (Fig. 4).[25, 26] There are two subunits present within RNRs, R1 and R2, and it is within R1 that the reduction takes place *via* redox active cysteines[27] catalyzed by a dithiol group of thioredoxin.[28] It is within R2 however that the diiron centre is located, stabilising the tyrosyl radical that is thought to initiate the radical-based reaction.[27] It is the formation of a diiron intermediate that oxidises the radical cofactor to the tyrosyl radical.[29, 30]

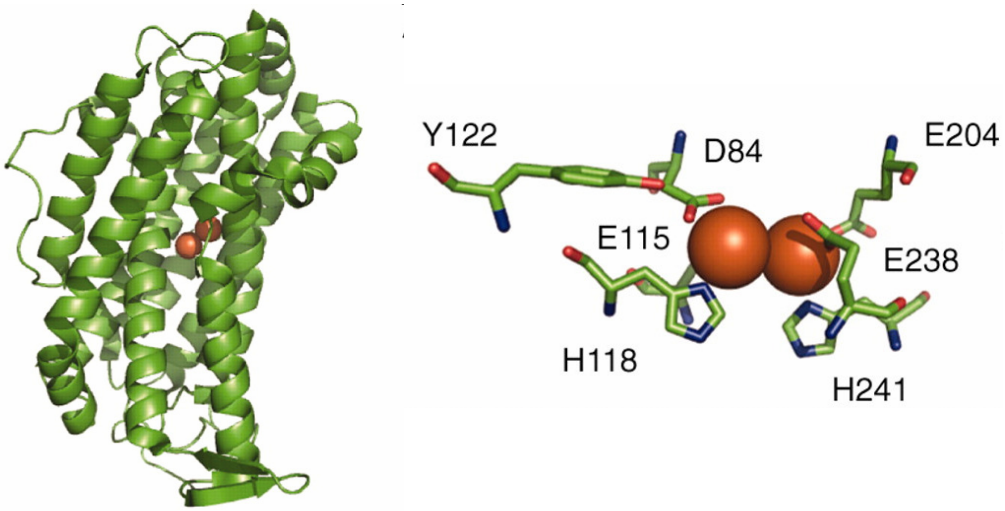

Fig. 4 RNR molecule with diiron site in orange.[31]

The examples shown above are only an illustration of the importance of iron to living organisms. This importance can be relayed in the efforts being made by synthetic chemists to model these systems. Synthetic analogues of the diiron enzymes could not only shed light on the proposed mechanisms but also befit industrial tasks in their own right, such as catalyzing the conversion of methane to methanol (mimicking MMO).[20] The synthesis of polynuclear clusters in an effort to understand the biomineralisation that occurs within ferritin is commonplace now. The process provides a polynuclear oxyhydroxide core within the apoferritin sheath akin to the ferrihydrite mineral found on the Earth's surface.[4, 7]

Ferrihydrite ($Fe_5HO_8 \cdot 4H_2O$) is one of the more prevalent minerals found on the Earth's surface,[32] but it is goethite (α-FeOOH), hematite (α-Fe_2O_3) and magnetite (Fe_3O_4) that are by far the most abundant. Their abundance and low cost have led to their use as inorganic pigments (Fig 5.) and as the raw materials for iron and steel production.[33] The pigmentary properties of the minerals could be realised in molecular form, with an added ability to fine tune the properties through ligand interactions.

Fig 5. Examples of pigmentary iron oxides currently in use.[34]

Magnetite is perhaps the most interesting mineral due to its magnetic properties and role within nature. When occurring as a naturally magnetised mineral in the form of lodestone it can attract small pieces of iron, and its properties were utilised by early civilisations as primitive compasses.[35] Crystals of magnetite can

also be found in the brains of certain animals that present magnetoreception abilities, providing an internal compass for the animal.[36] Unsurprisingly molecular analogues have been synthesised attempting to replicate the remarkable natural properties, yet more frequently have been found to exhibit more complex intra- and inter- molecular properties. These molecules are the basis of the ever expanding field of molecular magnetism, creating a platform for interests entwined within all fields of science.[37, 38]

1.3 Magneto-structural correlations

At the origins of magnetic interest in iron clusters were the iron dimers synthesised whilst modelling the biological sites. The vast number of molecules available gave researchers a means to correlate the structure to the magnetic properties. The degree of magnetic exchange between two coupled paramagnetic centres will rely on the nature of the bridge (the ligand) and the angles and bond lengths of that bridge; with enough coherent data a magneto-structural correlation can be attributed to the system. By analysing 36 Fe-O(R)-Fe interactions contained within iron dimers and a few trimers, Gorun and Lippard[39] were able to derive a correlation between the magnitude of antiferromagnetic exchange, J, and a parameter, P given in equation 1 below:

$$-J = A\exp(BP) \quad \text{where } A = 8.763\text{x}10^{11}\text{cm}^{-1} \text{ and } B = -12.663\ \text{Å}^{-1} \qquad (1)$$

P is half the superexchange pathway between two iron centres and is given units in Å as a unit of distance. The correlation stands for all clusters analysed containing additional bridges such as a carboxylate but fails with singly bridged clusters. They attempted to further correlate by factoring in the angles involved in the bridging but were ultimately unsuccessful. It was Weihe and Güde[40] who introduced an angular and radial overlap model to account for the Fe-O-Fe distance as well as the Fe-O-Fe angle. The mean Fe-O distance is defined r and the Fe-O-Fe angle defined ϕ, giving equation 2 below:

$$J = 1.337\times10^{8}(3.536 + 2.488\cos\phi + \cos^{2}\phi)\times\exp(-7.909r) \qquad (2)$$

By introducing the angular overlap they were able to differentiate between the sσ and pσ contributions from the oxide ligand. The correlation was more dependant on the bond distance rather than the angle and in fact the angular dependence decreased as the bond angle increased.

Werner *et al* later built on these studies to gain a magenetostructural correlation for the diiron complexes containing a phenoxo-, alkoxo- or hydroxo- bridge with one other ligand.[41] They argue that due to the high spin d^5 electron configuration yielding a spherical electron distribution, the variable angular dependencies will compensate each other and there will be no definitive angular dependence. For this reason they consider a solely radial correlation, given in equation 3, where *d* is the average Fe-O distance between the phenoxo-, alkoxo or hydroxo bridges:

$$J = -10^7 \exp(-6.8d) \qquad (3)$$

By introducing a radial and angular overlap parameter as well they found similar results to the single term equation 3, stressing that the significance lies predominantly with the Fe-O distance.

Molecules with larger nuclearity can be expected to be far more complicated as the amount of orbitals, distances, angles etc. increase. Nevertheless some of the underlying principles, such as the importance of Fe-O bond length and the differences in Fe-O-Fe to Fe-OR-Fe, can be applied to larger clusters; an example being the Fe_4 butterfly complexes whose generic core can be seen in Fig. 6.

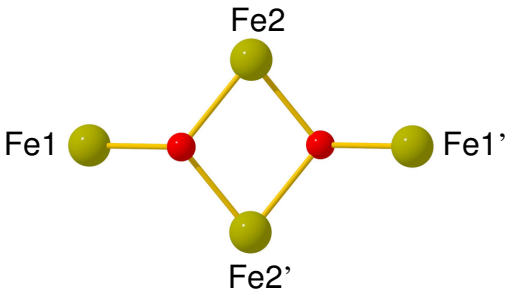

Fig 6. Molecular structure of a generic Fe_4 "butterfly" cluster where Fe1 and Fe1' are 'wingtip' and Fe2 and Fe2' are 'body' irons.

Christou and co-workers were able to show that the averaged Fe-O bond lengths of the body to wing Fe1-Fe2 interactions (J_{wb}) being shorter than the body to body Fe2-Fe2' interactions (J_{bb}) gave a more negative J value, in accordance with the correlations detailed above. A minimum in error of J_{wb} was found at -45 cm^{-1} but no minimum could be found for J_{bb}. By keeping J_{wb} constant they were able to produce near identical theoretical simulations for J_{bb} values of -10 cm^{-1}, +50 cm^{-1} and +100cm^{-1}, the last two being very large ferromagnetic interactions. It was clear then that J_{wb} was dominant and there was essentially no dependence on J_{bb} other than it was more positive than -15 cm^{-1}. The basis of this anomaly was attributed to spin frustration, a concept that will be discussed further in the following text.[42]

1.4 Magnetic properties of Iron

The most common oxidation state of iron is Fe^{III}, which provides a high spin ground state of S = 5/2, giving it great potential to display interesting magnetic properties. The exchange between neighbouring centres of Fe^{III} within clusters is dominated by antiferromagnetic interactions. This makes the synthesis of large spin ground state molecules difficult so a lot of importance rests on the geometric shape of the molecule. It is important to recognise that aligning the spins of interacting Fe^{III} centres antiparallel to each other is much more favourable than parallel. Molecules displaying bipartiteness will almost certainly exhibit a zero spin ground state, as there is a pathway within the molecule that will appease the alignment of antiparallel spins. Molecules without this pathway cannot concisely distribute the spins in a manner where each individual interaction is antiparallel. We can explain this with the simple example of a triangular μ_3-oxo bridge unit shown in Fig. 7.

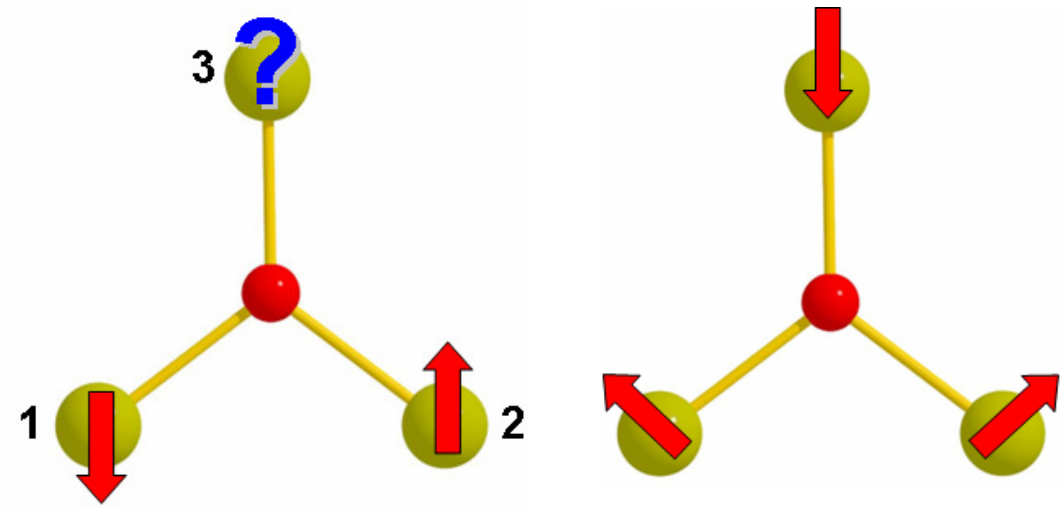

Fig. 7 Schematic representation of triangular μ_3-oxo bridge unit alignment of spins. Colour code: Fe = olive green; O = red.

The interaction between atoms 1 and 2 is antiferromagnetic and the interaction of each of these with atom 3 should also be antiferromagnetic. However if 3 is to satisfy an antiferromagnetic interaction with 1 its spin aligns parallel with that of 2 creating an energetically unfavourable ferromagnetic interaction. It is this conflict that is the basis of spin frustration. The molecule will most likely align the spins with atypical angles, as seen on the right of Fig. 7, garnering a non zero ground state.[43, 44]

Triangles sharing vertices are present in 2D lattices which display spin frustration, for example the kagome lattice found in the mineral Jarosite (Fig. 8).[45, 46] Frustrated 3D lattices, such as the pyrochlore lattice (named after the mineral $(Na,Ca)_2Nb_2O_6(OH,F)$ that it is found in), are also possible from the hexagonal arrangement of tetrahedral units.[47]

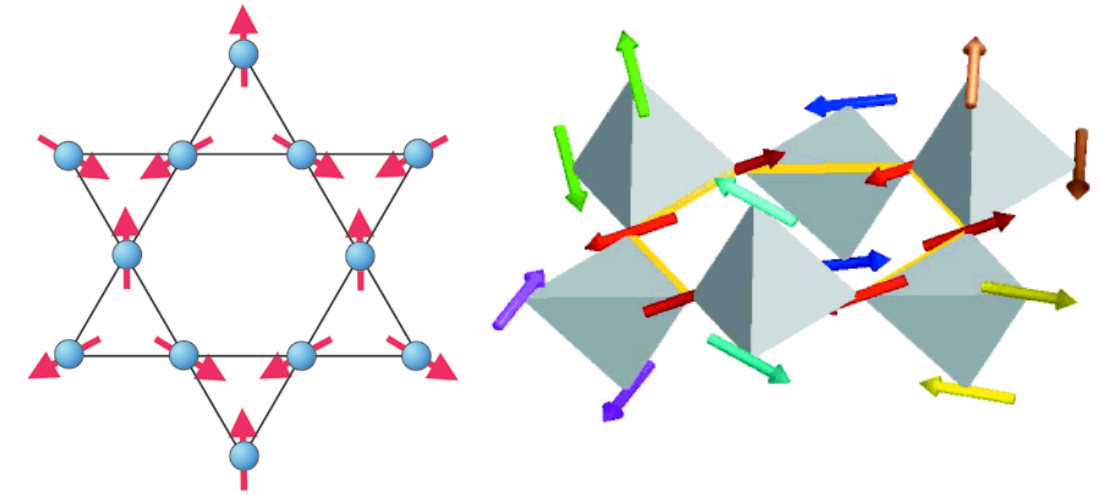

Fig. 8 Kagome and pyrochlore lattices with arrows indicating the frustrated spins.[48, 49]

Realisation of these perfect lattices within molecular entities is a major field of molecular magnetism. Frustration within a molecule can have a marked effect on the energy spectrum creating instances of low lying excited states and magnetization jumps or plateaux. Near degenerate ground states can be witnessed in simple triangles.[50] Hendrickson[51] analyses the magnitude of the exchange within the triangle and how the ratios between competing interactions can relate to the frustration within the system. In all of the triangles modelled at the time of the work they used two J values, considering Fig. 6, $J_{12} = J_{13} = J_1$ and $J_{23} = J_2$. Hendrickson found that the ratio between these two exchange parameters, J_1/J_2, was the major contributing factor to the total spin ground state of the complex. Empirically this is defined as follows: if $J_1/J_2 \leq 0.3$ then $S = 5/2$; if $0.3 \leq J_1/J_2 \leq 0.55$ then $S = 3/2$; and if $0.55 \leq J_1/J_2 \leq 1.0$ then $S = 1/2$. The trend then reverses as the ratio is increased until we see ratios greater than 2 displaying $S = 5/2$ ground states as the J_1 interaction now dominates causing the Fe2-Fe3 interaction to become frustrated and align parallel to each other. The small changes in the J_1/J_2 ratio imposing such a control over the spin ground state show the evident frustration within the system. More elaborate spectra are seen when the nuclearity is increased. The tridecanuclear compound $(C_5H_6N^+)_5[Fe_{13}F_{24}(OCH_3)_{12}O_4]\cdot CH_3OH\cdot 4H_2O$ displays a high spin ground state, $S =$

23/2, with excited states (in order of decreasing spin from S = 21/2 to S = 15/2) separated by a mere 2.15 cm^{-1}.[52] The molecule which has encountered the most interest in its frustrated spin system has been the giant Keplerate Fe_{30} compound.[53] Synthesised by Achim Müller's group, it is an Archimedean solid of icosidodecahedron geometry contained within a diamagnetic core. The molecule as a whole has the formula, $[Mo_{72}Fe_{30}O_{252}(Mo_2O_7(H_2O))_2(Mo_2O_8H_2(H_2O))(CH_3COO)_{12}(H_2O)_{91}]$ • 150 H_2O, and it provides the best model of the Kagome lattice to date.[54] A highly frustrated molecule, it has three spin sublattices (Fig. 9) each of 10 spins with all spins within that sublattice aligned in the same direction. The nearest neighbour spin vectors are offset 120° in their angular orientation.[55]

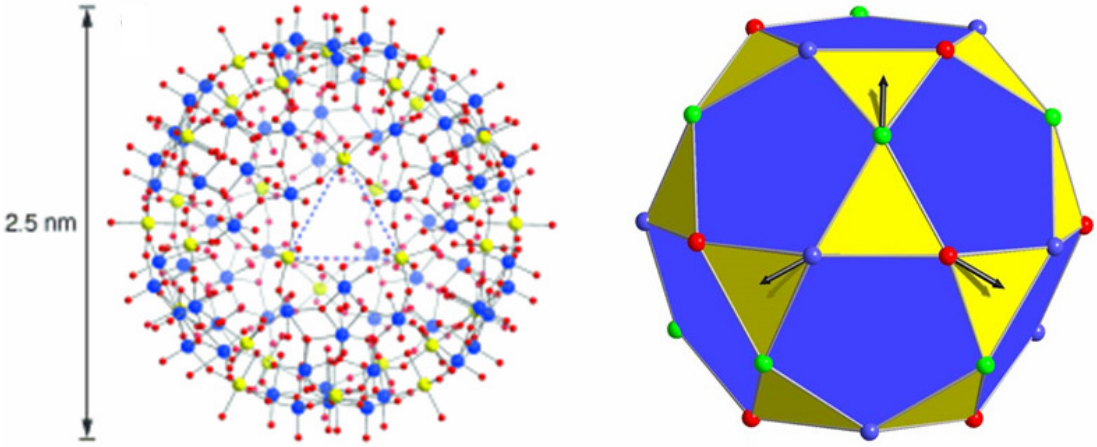

Fig. 9 The $\{Mo_{72}Fe_{30}\}$ spin ball with three spin lattices coloured red, blue and green. Arrows indicate the nearest neighbour spin vector alignment.[55]

The molecule is a zerodimensional system that at low temperature will exhibit magnetic ordering. There have been a lot of studies performed on the molecule as it continues to provide a platform for interests in mesoscopic sized magnetic molecules.[54, 56-59] The studies include analysing the classical and quantum properties over a range of temperatures, establishing that a deviation from classical to quantum occurs only below 50 mK.[56] INS, NMR and μSR investigations have taken

place in an effort to probe the spin dynamics of the system. The INS studies showed that excitations between the S = 0 ground state and S = 1 state were the most prevalent. For the allowed transitions they calculate a $J/5$ intraband mode transition and a higher $26/5J$ interband mode transition, which relate to 0.22 cm^{-1} and 5.56 cm^{-1} respectively. The intraband mode is not observable due to a large quasielectric background but the higher energy interband can be roughly aligned with the observable neutron excitations at ~4.83 cm^{-1}.[57] A quantum rotational band model can also be applied and the energy difference between the two lowest lying bands determined as 5.64 cm^{-1}.[54] Another phenomenon within the Fe_{30} molecule is the presence of unusual jumps in the magnetization as seen in the theoretical model of a S = ½ icosidodecahedron (Fig. 10). The minimal energies of the highest spins form a straight line in relation to the total spin, this then appears as a jump in the magnetisation (seen at the red arrow in Fig. 10).[58]

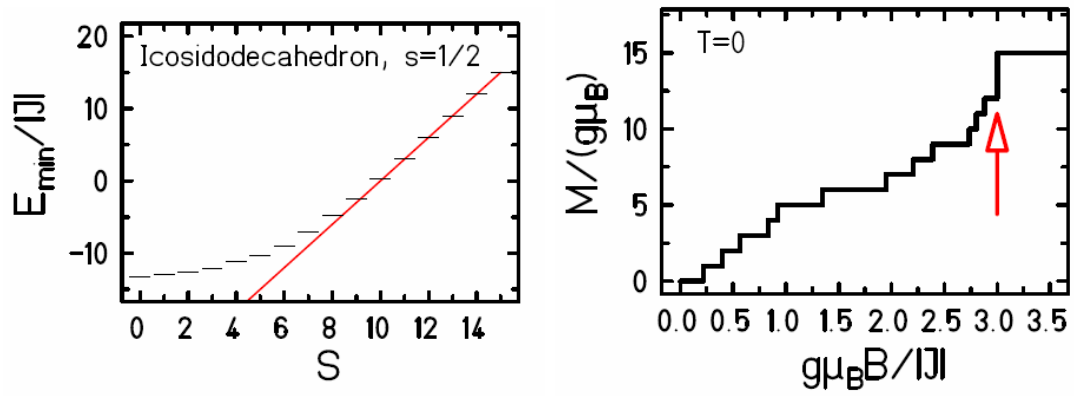

Fig. 10 (Left) Energy v Total Spin for the Fe_{30} molecule, the red line highlighting linear relationship between lowest lying energy states of highest spins. (Right) The magnetisation plot indicating the related jump in magnetisation at the red arrow.[58]

1.5 Single Molecule Magnets

Molecules that display hysteresis below a certain blocking temperature, T_B, are called single molecule magnets (SMM).[60, 61] The nanoscale size of these SMMs makes them attractive for computational purposes; in information storage or within quantum computation.[62] The molecules usually contain a metallic core stabilised by organic ligands which allow the core to behave as a discrete nanomagnet. For a

molecule to display such properties it must first have a large spin ground state, *S*. The large spin will have 2*S*+1 microstates, M_s, which will lose degeneracy with no applied field due to spin-orbit coupling or magnetodipolar interactions. This splitting is the nature of the zero-field splitting parameter, *D*, and it creates an energy barrier, *U*, to the reversal of the spin. Considering an *S* = 10 ground state as in Fig. 11 with $M_s = \pm S$ lying lowest in energy and $M_s = 0$ highest in energy, for the molecule to change from $M_s = +10$ to $M_s = -10$ it must overcome *U*. The energy barrier is calculated as $U = S^2|D|$ for integer spins and $U = (S^2-¼)|D|$ for half-integer spins.

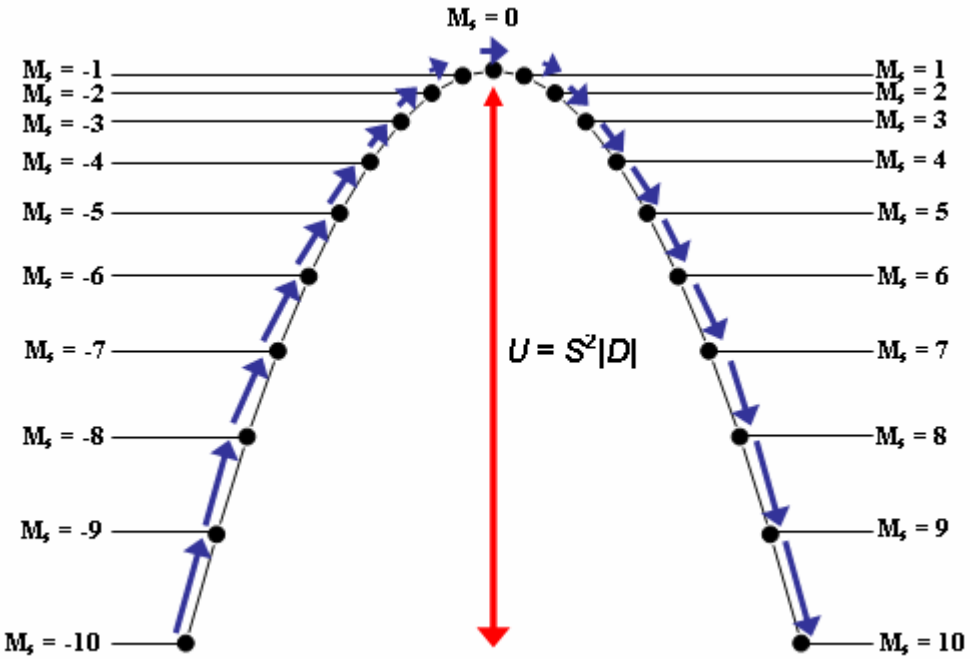

Fig. 11 Energy diagram of the zero-field splitting in a theoretical *S* = 10 spin ground state molecule. The red arrow indicates the energy barrier, *U*, and the blue arrows indicate the thermal pathway to reorientate from $-M_s$ to $+M_s$.

It is evident that when applying an external field to populate one microstate energy well, upon removal of this external field the molecule will retain its magnetisation. The time it takes to lose, or relax, this magnetisation is given by the Arrhenius equation 4 below:

$$\tau = \tau_0 \exp(U_{eff}/(kT)) \qquad (4)$$

τ is the relaxation time, τ_o is the pre-exponential factor and k is the Boltzmann constant. In some cases it can take years for this reversal to occur. This barrier equates only to the thermal activation over the barrier but the nanoscale of the molecules permits quantum phenomena to occur. Such phenomena are the quantum tunnelling of magnetisation (QTM) and the quantum phase interference (QPI).[37] QTM is the phenomena of the magnetisation reversing through the barrier rather than overcoming the energy and going over the barrier. This takes place when two M_s levels separated by the barrier align at the same energy. This can easily occur at zero-field as can be seen in Fig. 12 but it can also happen if an axial field is applied so that $H = nD/g\mu_B$, where g is the g-value and μ_B is the Bohr magneton.[63]

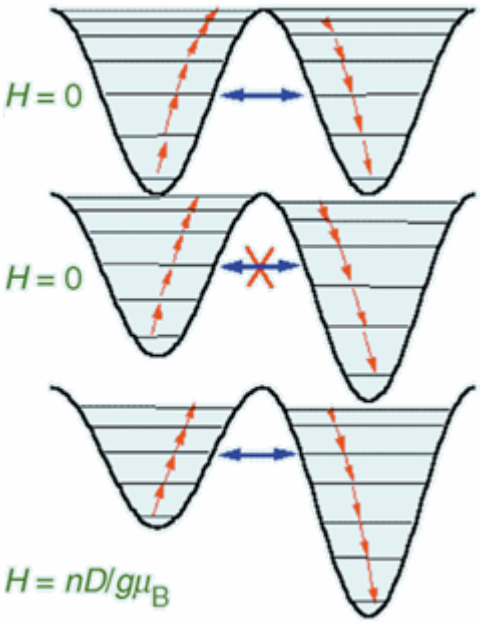

Fig. 12 Double well diagram where horizontal lines indicate M_s levels, red arrows indicate thermal activation 'over' the barrier and blue arrows indicate QTM 'through' the barrier.[63]

The first two pioneering examples of single molecule magnetism (SMM) were $[Mn_{12}O_{12}(O_2CMe)_{16}(H_2O)_4]$ and $[Fe_8O_2(tacn)_6(OH)_{12}]^{8+}$, referred to as Mn_{12} and Fe_8 for simplicity. The Mn_{12} molecule (Fig. 13) initiated interest in SMMs in 1991 when its "puzzling" magnetic properties were tentatively aligned with the properties of a superparamagnet.[64, 65] The molecule was shown to have a frequency

dependent out of phase component, $\chi_m T''$, in zero-field after studying its alternating current magnetic properties. This was attributed to the slow relaxation of the magnetisation, an effect never seen before in a molecule, which was later confirmed after hysteresis was observed below a blocking temperature, $T_B \approx 3$ K. Further studies defined an $S = 10$ spin ground state[66] and $D = -0.5$ cm^{-1} which results in an effective energy barrier of $U_{eff} \approx 60$ K.[64]

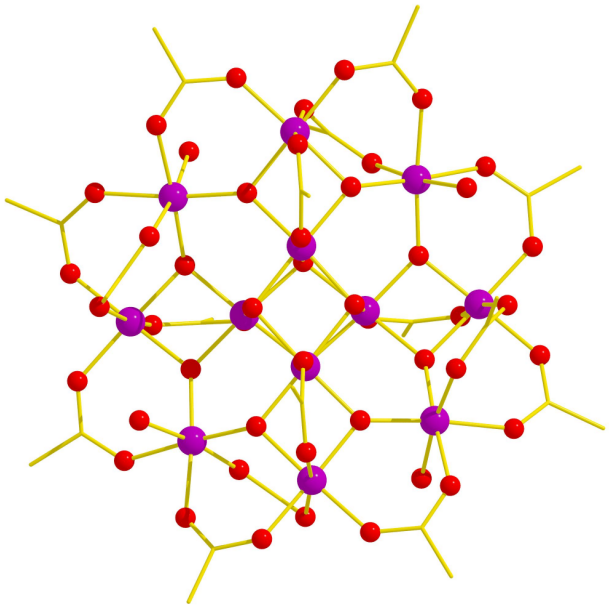

Fig. 13 The molecular structure of $[Mn_{12}O_{12}(O_2CMe)_{16}(H_2O)_4]$, the first SMM. Colour code: Mn = purple, O = red, C = gold. H atoms have been omitted for clarity.

A decade after the Fe_8 molecule (Fig. 14) was identified[67] its magnetic properties where analysed and found[68] to display an $S = 10$ ground state and an anisotropy $D = -0.34$ cm^{-1}. The molecule has provided many exciting and intriguing quantum results and was one of the first to display QTM. It also provides a clear example of how the structure and symmetry of a molecule can impact its magnetic properties, as the tunnelling effects are greatly enhanced due to the large transverse anisotropy created by the crystal symmetry.[69-72]

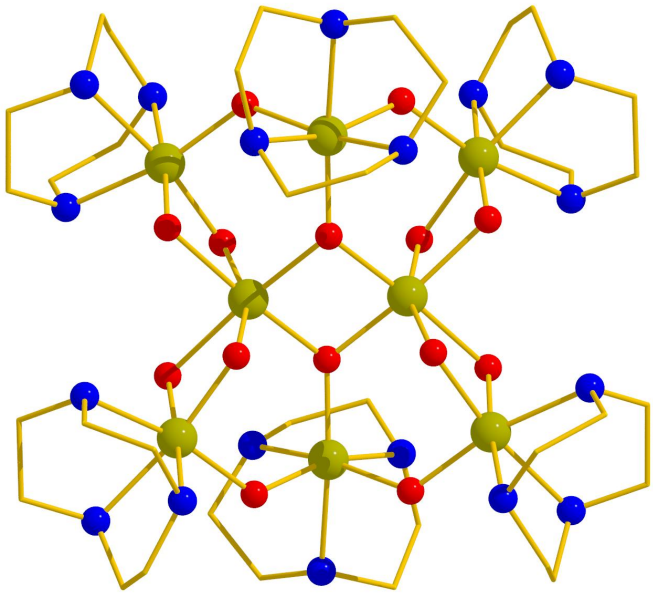

Fig. 14 Molecular structure of $[Fe^{III}_8O_2(OH)_{12}(tacn)_6]^{8+}$. Colour code: Fe = green, O = red, N = blue and C = gold. H atoms have been omitted for clarity

1.6 Magnetocaloric Effect

An impressive feature of molecules with degenerate or low-lying excited spin states is the presence of an enhanced magnetocaloric effect (MCE).[73-75] Molecules displaying the MCE can be used as magnetic refrigerants at low temperatures. When a magnetic field is applied the magnetic entropy of a system will decrease, this forms the basis for MCE. Within adiabatic conditions this can be exploited to create a temperature change giving a cooling effect (see Fig. 14). The magnetic entropy of a system is defined in equation 5 as:

$$S_m = R\ln(2S+1) \qquad (5)$$

where R is the gas constant equal to $N_A k_B$ and S the spin ground state of the system. The magnetic order of a material will change when a magnetic field is applied resulting in a change of magnetic entropy. Thus, in Fig. 15 if we start at the initial state A with temperature T_i and field H_i and if the system is in an adiabatic state, the total entropy of the system must be conserved, so a change in magnetic entropy will

result in a counter change in the lattice entropy. This will give a temperature change in the material, ΔT_{ad}, so by changing the field from H_i to H_f the temperature will change in moving from point A to point B. Position C in Fig. 15 is attained if the field is changed isothermally and a change in magnetic entropy, ΔS_m, results rather than a change in temperature. If there is a reduction in entropy associated with a change in field then there will be an increase in temperature but if there is an increase in entropy there will be a reduction in temperature.[74]

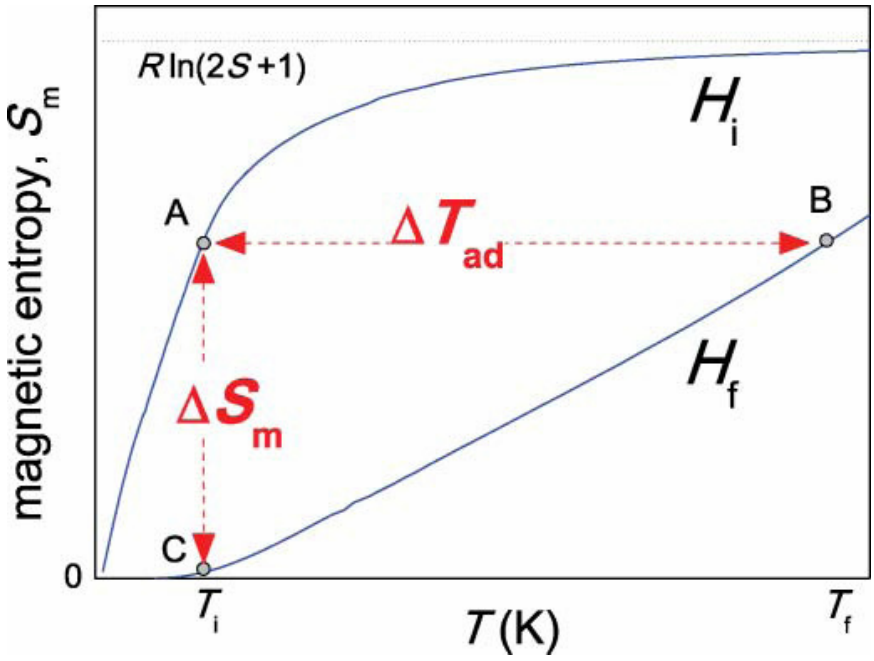

Fig. 15 A theoretical plot of magnetic entropy *vs* temperature highlighting the adiabatic magnetization, A to B, and isothermal magnetisation, A to C, processes.[74]

The low lying excited states of a frustrated molecule provide added degrees of freedom resulting in a larger magnetic entropy. One such example of this is the tetradecametallic Fe^{III} molecule, $[Fe_{14}(L)_6O_6(OMe)_{18}Cl_6]$ (L = 1,2,3-triazolate or derivatives), dc magnetic susceptibility studies reveal a ground spin state of $S = 25$ with low lying excited states and a concurrent negligible zero-field splitting parameter. This results in an isothermal magnetic entropy change $-\Delta S_m = 20.3$ J kg^{-1} K^{-1} with a magnetic field change of 0-7 T and at a temperature of 6 K for the

molecule with L = 1,2,3-triazolate.[76] This was one of the first highly symmetric molecules with a large spin ground state to be studied and it provided a great progression in the field with the largest MCE calculated below 10 K.[76-78]

1.7 Phenolic Oximes

Phenolic oxime ligands (a in Fig 16) have been selected for study in this thesis. They have been used extensively in industry as metal solvent extractants. When mono-deprotonated the molecules form a *pseudo*-macrocyclic ring which provides the ideally sized cavity for a Cu^{II} ion (c in Fig. 16). This ensures high selectivity for Cu^{II} over other transition metal ions, most notably iron (III) which can be present in pregnant leach solutions in equal or greater concentrations. The sequence of reactions (equations 6 to 10) involved in sulphuric acid leaching of oxidic ore, extraction of copper into a hydrocarbon solution, stripping back into sulphuric acid and electrowinning to generate conductivity grade metal:

Leach:	$CuO_{(s)} + H_2SO_4$	$\longrightarrow$	$CuSO_4 + H_2O$	(6)
Extract:	$CuSO_4 + 2\mathbf{L}H_{(org)}$	$\longrightarrow$	$Cu\mathbf{L}_{2\,(org)} + H_2SO_4$	(7)
Strip:	$Cu\mathbf{L}_{2\,(org)} + H_2SO_4$	$\longrightarrow$	$CuSO_4 + 2\mathbf{L}H_{(org)}$	(8)
Electrowin:	$CuSO_4 + H_2O$	$\longrightarrow$	$Cu_{(s)} + ½O_{2\,(g)} + H_2SO_4$	(9)

recycles all reagents and gives an excellent molecular balance.

$$CuO \longrightarrow Cu_{(s)} + ½O_{2\,(g)} \qquad (10)$$

Phenolic oximes used in extractive hydrometallurgy now account for around 20-30% of the worlds copper production.[79-81] Such extensive use has led to a large volume of research into the coordination chemistry of these ligands, to understand the complexation with trace metals in feed solutions to ensure that these are not extracted or irreversibly bound.[82-85] Also, as they are now manufactured on a large scale it is of interest to establish whether they can be used in other areas of coordination chemistry which do not involve metal extraction (see later in this section).

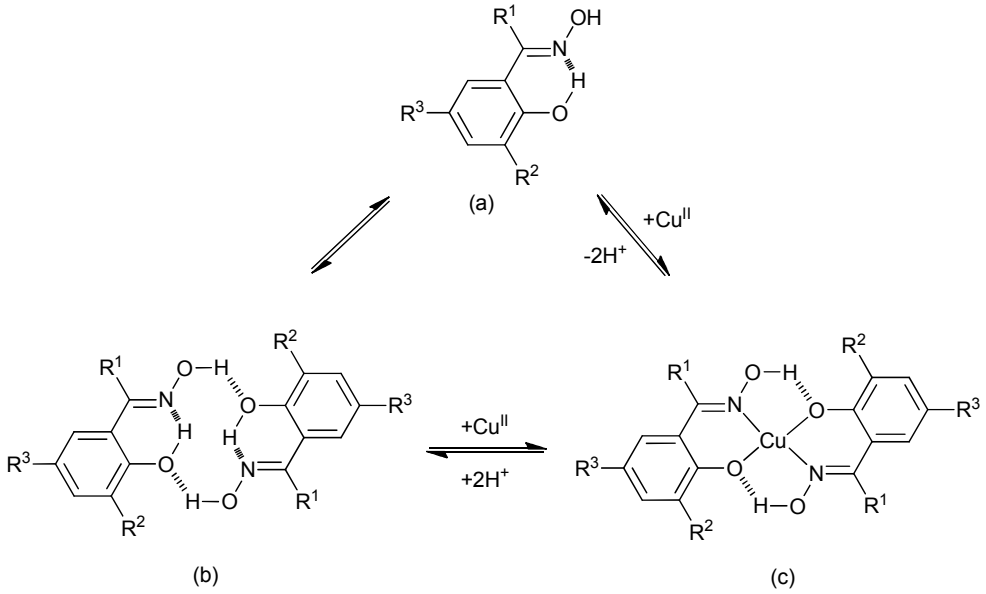

Fig. 16 (a) The general structure of the phenolic oxime showing H-bonding present. R groups are defined later. (b) The free ligand dimer. (c) The neutral *pseudo*-macrocyclic complex formed on complexation of Cu^{II} and deprotonation at the phenol group.

Similar mononuclear complexes with Ni^{II}, Zn^{II}, Pd^{II} and Co^{III} exist[86] in which the phenolic oxime ligand is mono-deprotonated creating the fourteen membered *pseudo*-macrocyclic ring with hydrogen bonding between the oxime unit and the deprotonated phenol group.

If a substituent is introduced at position R^2 it will affect the H-bonding between the two ligands. A substituent with H-bond acceptor properties, such as a halogen atom, will buttress the H-bonding and increase stability and extractant strength. Conversely a bulkier group with poorer H-bonding properties will have an adverse effect on the stability and the extractant strength will decrease.[83]

The examples shown above have only been concerned with the phenolic oxime mono-deprotonated at the phenol group, if we also deprotonate the oxime group we open up the possibility for polynuclear metal complexation. The most common binding mode of the phenolic oxime when doubly deprotonated is the dinucleating species seen in Fig. 17 which allows for three metal cations to assemble in a triangle around a μ_3-oxo atom.

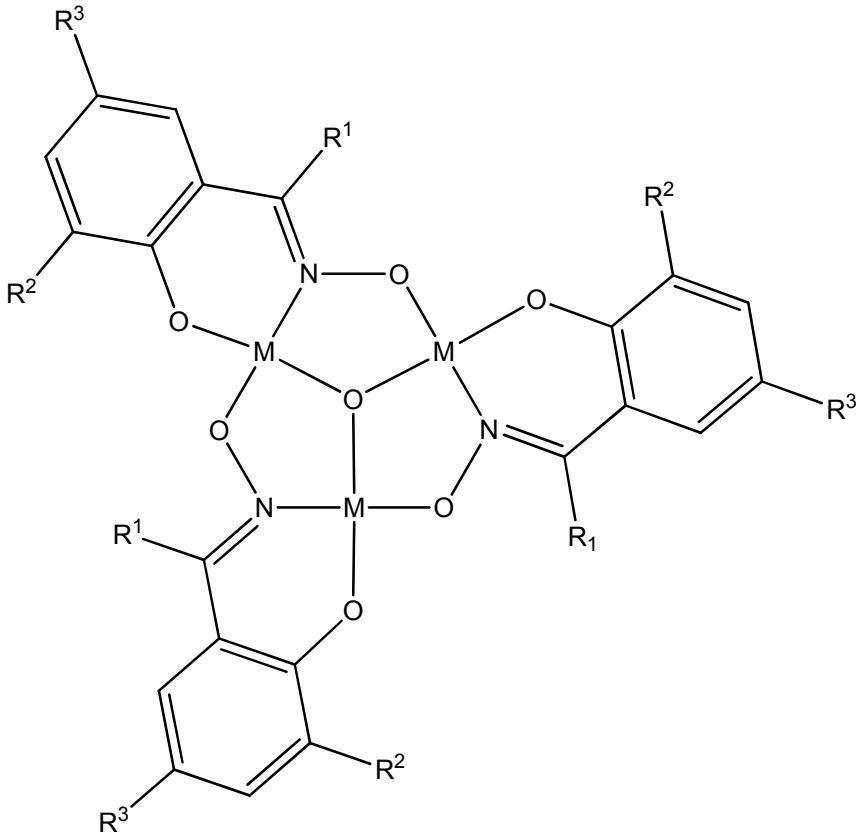

Fig. 17 The $[M_3O(oximate)_3]^+$ moiety which is the most common building block seen in polynuclear complexes of phenolic oximes.

The ligands still have free electron pairs available for complexation (a in Fig. 18) and these triangular units can readily assemble into hexanuclear units (see later text) by means of binding modes c and d in figure 18. The ligands offer the potential to theoretically bind to five metal ion centres, the literature preceding this work however only describes complexation to a maximum of three metal centres, the most common of which are shown in Fig. 18. During the course of this work a new binding mode, $\eta^2\eta^1\eta^2{:}\mu_4$, (e in Fig. 18) was discovered with Fe^{III} and has subsequently been seen with Mn^{III}.[87, 88]

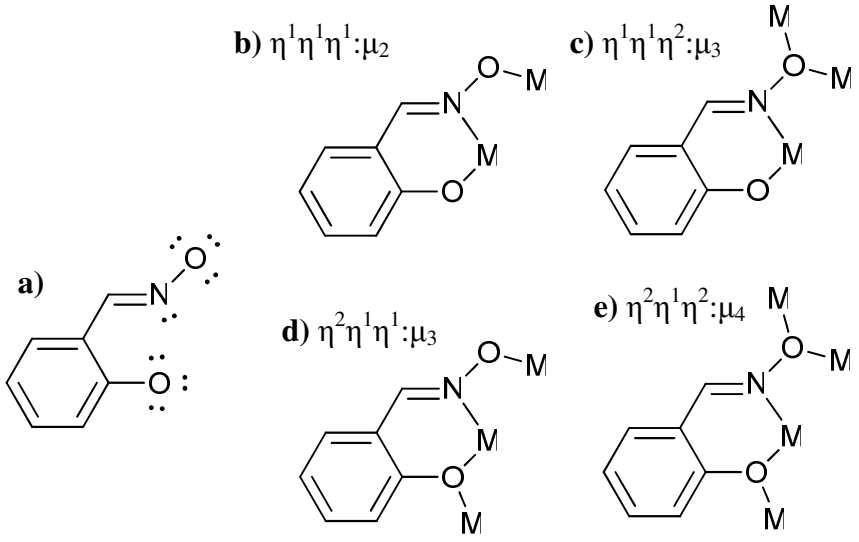

Fig. 18 a) The available binding sites of a phenolic oxime ligand. b) The most common μ_2 binding mode. c) and d) are the most common μ_3 binding modes and e) is the largest polynucleating binding mode seen in the literature.

As can be seen from Fig. 16 and 17 there are a multitude of different derivatives that can be synthesised by varying the R groups. The main derivatives described within this thesis are seen in Fig. 19 below.

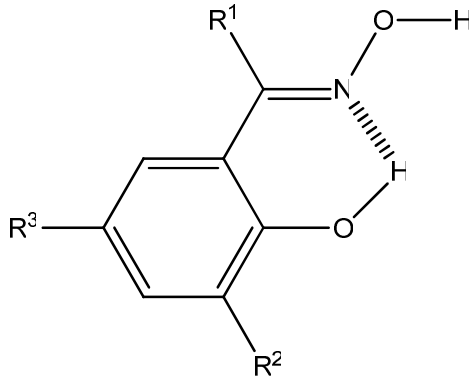

	R^1	R^2	R^3
$saoH_2$	H	H	H
Me-$saoH_2$	Me	H	H
Et-$saoH_2$	Et	H	H
Ph-$saoH_2$	Ph	H	H
^{t}But-$saoH_2$	H	^{t}But	H
Acorga P5000	H	H	C_9H_{19}
3-^{t}But-5-NO_2-$saoH_2$	H	^{t}But	NO_2

Fig. 19 General structure of derivatised phenolic oximes, where sao is an abbreviation of salicylaldoxime.

As stated previously the triangular $[M^{III}_3O(sao)_3]$ units will readily assemble into hexanuclear complexes *via* four μ_3-sao^{2-} ligands, the core of which can be seen in Fig. 20. An example of this can be seen with Cr^{III} in $[Cr_6O_2(sao)_6(OOCC_2H_5)_2(OH_2)_2(C_2H_5CN)_2]$ but it is within Mn^{III} chemistry where the most research has taken place.[89, 90] The reason for the interest in the Mn^{III}-salicylaldoxime chemistry is due to SMMs. The Brechin group first synthesised SMMs of general formula $[Mn^{III}_6O_2(sao)_6(O_2CR)_2L_4]$ (where R = H, Me, Ph etc, and L = MeOH or EtOH) with $S = 4$ spin ground states and $U_{eff} = 28$ K in 2005, and these were based on the original work of Perlepes and Escuer from 2004.[91] By substituting the aldoxime, $saoH_2$, for a ketoxime such as Me-$saoH_2$ or Et-$saoH_2$, they were able to switch the magnetic exchange between the metal centres from antiferromagnetic to ferromagnetic, enabling a $S = 12$ ground state.[92, 93] A whole family of these clusters was synthesised and the research team was able to conclude that the difference in exchange was due to the variations of the oxime bound Mn-N-O-Mn torsion angle caused by variations of the bulk of these R^1 groups in figure 19. The approximate angle at which the magnetic exchange switched was found to be 31.3°. The molecule found to have the highest barrier to magnetisation reversal for any SMM (at the time but since bettered)[94] was found within this family of clusters as $[Mn^{III}_6O_2(Et\text{-}sao)_6(O_2CPh(Me)_2)(EtOH)_6]$, with $U_{eff} = 86.4$ K and $T_B = 5$ K (seen in figure 20).[95]

An extensive range of clusters has since been synthesised with slight dfferences from the Mn_6 family. The Mn_6 unit can be 'halved' by capping the triangular faces with bulkier ligands such as pyridine or by distorting the triangular face from planarity *via* a ClO_4 ligand to give $[Mn_3O(sao)_3]^+$ cores.[96-98] This family of Mn_3 clusters were shown to follow the same Mn-N-O-Mn torsion angle dependency as their Mn_6 counterparts.[98] Other ligands were introduced including halides and phosphinates but despite changes to the reaction conditions and variations of oxime the work is dominated by these Mn_3 and Mn_6 moeities.[99, 100] The difference between Mn^{III} and Fe^{III} phenolic oxime complexes is a feature of interest which is explored throughout this thesis.

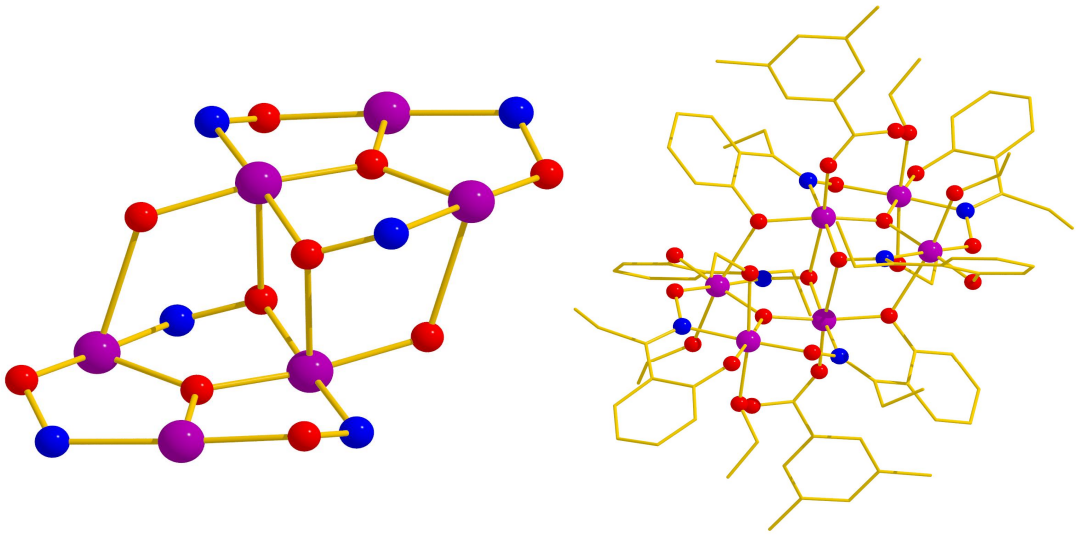

Fig. 20 (Left) The generic core of a $[M^{III}_6O_2(sao)_6]^{2+}$ core where M = Cr or Mn. (right) The molecular structure of $[Mn^{III}_6O_2(Et\text{-}sao)_6(O_2CPh(Me)_2)(EtOH)_6]$. Colour code: M = purple; O = red; N = blue and C = gold.

When R^3 is a multiply branched, mixed isomer, C_9H_{19} chain with R^1 and R^2 = H (Fig. 19), the ligand is known industrially as Acorga P5000 (referred to as P50) which is a major component of many formulations of copper extractants (see above). It has also been used as a corrosion inhibitor for lightly oxidised iron surfaces.[101]

Corrosion is an everyday occurrence and very familiar through the highly visible nature of rust in many aging steel structures. There are a number of techniques employed to combat corrosion currently in use: passive film formation; chromating; cathodic protection; anodic inhibitors; paints or plastic resin coatings and benign organic corrosion inhibitors.[102-104] Each technique has its advantages and disadvantages but we are concerned with organic corrosion inhibition *via* the phenolic oxime ligands. The principle here is that these ligands will adsorb to a lightly oxidised iron surface through an anionic head, as in X in Fig. 21, and have a hydrophobic tail trailing that will prevent any aqueous solutions, as in R in Fig. 21, from attacking the surface. The concentration of the ligand administered to the surface will have to be in such abundance as to cover all vulnerable areas. No two iron surfaces will be the same and upon each surface there will be crevasses and pits not observable to the eye, this creates problems when attempting to analyse the mode-of-action of the ligands.

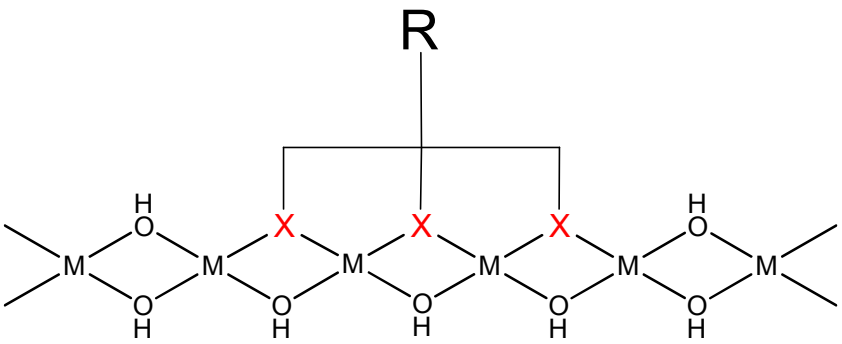

Fig. 21 Scheme representing a ligand bound to an oxidized surface where X denotes the anodic head group and R denotes a hydrophobic tail group.

To identify the binding modes of the ligand it is helpful to synthesise molecular clusters of metal and ligand. Previous work with carboxylates has shown that with enough crystallographic evidence, computational methods can be used to provide theoretical binding modes of the ligand.[105] Prior to this thesis there were nineteen examples of Fe-salicylaldoxime clusters in the CCDC database, and in fact prior to the work of Gass and Brechin there were only eleven.[101, 106-113] These clusters ranged in nuclearity from Fe_2-Fe_9. One of these clusters was a tetranuclear iron molecule, $[Fe_4(sao)_4(saoH)_4]\cdot saoH_2\cdot C_8H_{10}$, that formed the theory that the protection offered to iron surfaces by P50 was due to polynuclear iron cluster formation at the surface rather than the ligand binding directly to the surface as in Fig. 21.[101] The techniques utilised in the paper appear to point to the tetranuclear species being present on the surface of a salycylaldoxime treated iron surface. It is noted within the text that there are other nuclearities possible, and within differing conditions it is probable that they will also exist. It is clear then that a more comprehensive knowledge of the coordination chemistry of the phenolic oximes with iron will divulge insights into the modes-of-action of the corrosion inhibition ability.

1.8 Summary

The remaining chapters of this thesis describe the synthesis of a host of polynuclear iron complexes with derivatised phenolic oxime ligands of the types shown in Fig. 19. Chapter two considers the common building blocks of triangular $[Fe_3O]^{7+}$ and tetrahedral $[Fe_4O]^{11+}$ units and how these can be manipulated by varying reaction conditions to give more elaborate clusters. In chapter three co-ligands that have successfully resulted in isolation of iron clusters previously in the literature are employed alongside the phenolic oxime ligands in an attempt to determine the role that the phenolic oxime ligand plays in dictating the structure of the iron core. Two 'simple' phenolic oxime units cross-linked by an organic strap are used in chapter four to bring together the polynuclear units described in the other chapters to create interesting cage complexes with a lot of scope for future work.

1.9 References

1. S. C. Andrews, P. Arosio, W. Bottke, J.-F. Briat, M. von Darl, P. M. Harrison, J.-P. Laulhère, S. Levi, S. Lobreaux and S. J. Yewdall, *J. Inorg. Biochem.*, 1992, **161**.
2. I. G. Macara, T. G. Hoy and P. M. Harrison, *Biochem. J.*, 1972, **126**, 14.
3. B. Xu and N. D. Chasteen, *J. Biol. Chem.*, 1991, **266**, 19965.
4. S. A. Malone, A. Lewin, M. A. Kilic, D. A. Svistunenko, C. E. Cooper, M. T. Wilson, N. E. Le Brun, S. Spiro and G. R. Moore, *J. Am. Chem. Soc.*, 2004, **126**, 496.
5. E. C. Theil, *Annu. Rev. Biochem.*, 1987, **57**, 289.
6. A. Ilari, S. Stefanini, E. Chiancone and D. Tsernoglou, *Nat. Struct. Biol.*, 2000, **7**, 6.
7. S. M. Gorun, G. C. Papaefthymiou, R. B. Frankel and S. J. Lippard, *J. Am. Chem. Soc.*, 1987, **109**, 3337.
8. R. Frey, M. Donlin and J. Bashkin, *Ferritin Molecular-Graphics Tutorial*, Washington University, St. Louis, MO, 1995.
9. A. C. Rosenzweig, C. A. Frederick, S. J. Lippard, P. Nordlund and auml, *Nature*, 1993, **366**, 537.
10. R. E. Stenkamp, *Chem. Rev.*, 1994, **94**, 715.
11. J. L. York and A. J. Bearden, *Biochemistry*, 1970, **9**, 4549.
12. A. L. Feig and S. J. Lippard, *Chem. Rev.*, 1994, **94**, 759.
13. M.-H. Baik, M. Newcomb, R. A. Friesner and S. J. Lippard, *Chem. Rev.*, 2003, **103**, 2385.
14. J. D. Lipscomb, *Annu. Rev. Microbiol.*, 1994, **48**, 371.
15. R. L. Lieberman and A. C. Rosenzweig, *Nature*, 2005, **434**, 177.

16. H. Basch, K. Mogi, D. G. Musaev and K. Morokuma, *J. Am. Chem. Soc.*, 1999, **121**, 7249.
17. A. M. Valentine, S. S. Stahl and S. J. Lippard, *J. Am. Chem. Soc.*, 1999, **121**, 3876.
18. K. E. Liu, A. M. Valentine, D. Qiu, D. E. Edmondson, E. H. Appelman, T. G. Spiro and S. J. Lippard, *J. Am. Chem. Soc.*, 1995, **117**, 4997.
19. K. E. Liu, A. M. Valentine, D. Wang, B. H. Huynh, D. E. Edmondson, A. Salifoglou and S. J. Lippard, *J. Am. Chem. Soc.*, 1995, **117**, 10174.
20. I. Siewert and C. Limberg, *Chem. Eur. J*, 2009, **15**, 10316.
21. R. A. Friesner, M.-H. Baik, B. F. Gherman, V. Guallar, M. Wirstam, R. B. Murphy and S. J. Lippard, *Coord. Chem. Rev.*, 2003, **238-239**.
22. R. E. Stenkamp, L. C. Sieker and L. H. Jensen, *J. Am. Chem. Soc.*, 1984, **106**, 618.
23. M. Wirstam, S. J. Lippard and R. A. Friesner, *J. Am. Chem. Soc.*, 2003, **125**, 3980.
24. T. C. Brunold and E. I. Solomon, *J. Am. Chem. Soc.*, 1999, **121**, 8277.
25. J. Stubbe, *J. Biol. Chem.*, 1990, **265**, 5329.
26. W. H. Tong, S. Chen, S. G. Lloyd, D. E. Edmondson, B. H. Huynh and J. Stubbe, *J. Am. Chem. Soc.*, 1996, **118**, 2107.
27. P. Nordlund, B.-M. Sjoberg and H. Eklund, *Nature*, 1990, **345**, 593.
28. B. M. Sjöberg and P. Reichard, *J. Biol. Chem.*, 1977, **252**, 536.
29. D. Burdi, B. E. Sturgeon, W. H. Tong, J. Stubbe and B. M. Hoffman, *J. Am. Chem. Soc.*, 1996, **118**, 281.
30. B. E. Sturgeon, D. Burdi, S. Chen, B.-H. Huynh, D. E. Edmondson, J. Stubbe and B. M. Hoffman, *J. Am. Chem. Soc.*, 1996, **118**, 7551.
31. A. Schirmer, M. A. Rude, X. Li, E. Popova and S. B. del Cardayre, *Science*, 2010, **329**, 559.
32. J. L. Jambor and J. E. Dutrizac, *Chem. Rev.*, 1998, **98**, 2549.
33. M. A. Legodi and D. de Waal, *Dyes Pigm.*, 2007, **74**, 161.
34. Image courtesy of http://www.rockwoodspecialties.com.
35. M. Cyrot and E. D. Trémolet de Lacheisserie, *Magnetism: Fundamentals, Volume 1*, Springer, 2002.
36. W. Wiltschko and R. Wiltschko, *Journal of Comparative Physiology A: Neuroethology, Sensory, Neural, and Behavioral Physiology*, 2005, **191**, 675.
37. D. Gatteschi and R. Sessoli, *Angew. Chem. Int. Ed*, 2003, **42**, 268.
38. G. W. Powell, H. N. Lancashire, E. K. Brechin, D. Collison, S. L. Heath, T. Mallah and W. Wernsdorfer, *Angew. Chem. Int. Ed*, 2004, **43**, 5772.
39. S. M. Gorun and S. J. Lippard, *Inorg. Chem.*, 1991, **30**, 1625.
40. H. Weihe and H. U. Güdel, *J. Am. Chem. Soc.*, 1997, **119**, 6539.
41. R. d. Werner, S. Ostrovsky, K. Griesar and W. Haase, *Inorg. Chim. Acta*, 2001, **326**, 78.
42. J. K. McCusker, J. B. Vincent, E. A. Schmitt, M. L. Mino, K. Shin, D. K. Coggin, P. M. Hagen, J. C. Huffman, G. Christou and D. N. Hendrickson, *J. Am. Chem. Soc.*, 1991, **113**, 3012.
43. J. Schnack, *Dalton Trans.*, 2010, **39**, 4677.
44. O. Kahn, *Chem. Phys. Lett.*, 1997, **265**, 109.
45. J. L. Atwood, *Nat. Mater.*, 2002, **1**, 91.

46. K. Matan, B. M. Bartlett, J. S. Helton, V. Sikolenko, S. Matt'aš, K. Prokeš, Y. Chen, J. W. Lynn, D. Grohol, T. J. Sato, M. Tokunaga, D. G. Nocera and Y. S. Lee, *Phys. Rev. B*, 2011, **83**, 214406.
47. J. E. Greedan, *J. Mater. Chem.*, 2001, **11**, 37.
48. J. S. Helton, K. Matan, M. P. Shores, E. A. Nytko, B. M. Bartlett, Y. Yoshida, Y. Takano, A. Suslov, Y. Qiu, J. H. Chung, D. G. Nocera and Y. S. Lee, *Phys. Rev. Lett.*, 2007, **98**, 107204.
49. S.-H. Lee, Q. Huang, C. Broholm, G. Gasparovic, W. Ratcliff, S.-W. Cheong and T. H. Kim, *Emergent Excitations in a Geometrically Frustrated Magnet, NCNR 2002 Annual Report*, 2002.
50. M. Fardis, G. Diamantopoulos, M. Karayianni, G. Papavassiliou, V. Tangoulis and A. Konsta, *Phys. Rev. B*, 2001, **65**, 014412.
51. D. N. Hendrickson, *Spin Frustration in Polynuclear Complexes*, World Scientific Publishing, 1993.
52. J. van Slageren, P. Rosa, A. Caneschi, R. Sessoli, H. l. n. Casellas, Y. V. Rakitin, L. Cianchi, F. D. Giallo, G. Spina, A. Bino, A.-L. Barra, T. Guidi, S. Carretta and R. Caciuffo, *Phys. Rev. B*, 2006, **73**, 014422.
53. A. Müller, S. Sarkar, S. Q. N. Shah, H. Bögge, M. Schmidtmann, S. Sarkar, P. Kögerler, B. Hauptfleisch, A. X. Trautwein and V. Schünemann, *Angew. Chem. Int. Ed*, 1999, **38**, 3238.
54. J. Schnack, M. Luban and R. Modler, *Europhys. Lett.*, 2001, **56**, 863.
55. A. Müller, M. Luban, C. Schröder, R. Modler, P. Kögerler, M. Axenovich, J. Schnack, P. Canfield, S. Bud'ko and N. Harrison, *ChemPhysChem*, 2001, **2**, 517.
56. M. Axenovich and M. Luban, *Phys. Rev. B*, 2001, **63**, 100407.
57. V. O. Garlea, S. E. Nagler, J. L. Zarestky, C. Stassis, D. Vaknin, P. Kögerler, D. F. McMorrow, C. Niedermayer, D. A. Tennant, B. Lake, Y. Qiu, M. Exler, J. Schnack and M. Luban, *Phys. Rev. B*, 2006, **73**, 024414.
58. J. Schnack, *C. R. Chim.*, 2008, **10**, 15.
59. C. Schröder, H. Nojiri, J. Schnack, P. Hage, M. Luban and P. Kögerler, *Phys. Rev. Lett.*, 2005, **94**, 017205.
60. D. Gatteschi, R. Sessoli and J. Villain, *Molecular Nanomagnets*, Oxford University Press, 2006.
61. R. E. P. Winpenny, *Single-Molecule Magnets and Related Phenomena*, Springer, 2006.
62. M. N. Leuenberger and D. Loss, *Nature*, 2001, **410**, 789.
63. D. Gatteschi, R. Sessoli and A. Cornia, *Chem. Commun.*, 2000, 725.
64. A. Caneschi, D. Gatteschi, R. Sessoli, A. L. Barra, L. C. Brunel and M. Guillot, *J. Am. Chem. Soc.*, 1991, **113**, 5873.
65. R. Sessoli, H. L. Tsai, A. R. Schake, S. Wang, J. B. Vincent, K. Folting, D. Gatteschi, G. Christou and D. N. Hendrickson, *J. Am. Chem. Soc.*, 1993, **115**, 1804.
66. R. Sessoli, D. Gatteschi, A. Caneschi and M. A. Novak, *Nature*, 1993, **365**, 141.
67. K. Weighardt, K. Pohl, I. Jibril and G. Huttner, *Angew. Chem. Int. Ed*, 1984, **23**, 77.
68. C. Delfs, D. Gatteschi, L. Pardi, R. Sessoli, K. Wieghardt and D. Hanke, *Inorg. Chem.*, 1993, **32**, 3099.

69. T. Ohm, C. Sangregorio and C. Paulsen, *Eur. Phys. J. B*, 1998, **6**, 195.
70. T. Ohm, C. Sangregorio and C. Paulsen, *J. Low Temp. Phys.*, 1998, **113**, 1141.
71. C. Sangregorio, T. Ohm, C. Paulsen, R. Sessoli and D. Gatteschi, *Phys. Rev. Lett.*, 1997, **78**, 4645.
72. W. Wernsdorfer, T. Ohm, C. Sangregorio, R. Sessoli, D. Mailly and C. Paulsen, *Phys. Rev. Lett.*, 1999, **82**, 3903.
73. P. Debye, *Annalen der Physik*, 1926, **386**, 1154.
74. M. Evangelisti and E. K. Brechin, *Dalton Trans.*, 2010, **39**, 4672.
75. W. F. Giauque, *J. Am. Chem. Soc.*, 1927, **49**, 1864.
76. R. Shaw, R. H. Laye, L. F. Jones, D. M. Low, C. Talbot-Eeckelaers, Q. Wei, C. J. Milios, S. Teat, M. Helliwell, J. Raftery, M. Evangelisti, M. Affronte, D. Collison, E. K. Brechin and E. J. L. McInnes, *Inorg. Chem.*, 2007, **46**, 4968.
77. M. Evangelisti, A. Candini, A. Ghirri, M. Affronte, E. K. Brechin and E. J. L. McInnes, *Appl. Phys. Lett.*, 2005, **87**, 072504.
78. D. M. Low, L. F. Jones, A. Bell, E. K. Brechin, T. Mallah, E. Rivière, S. J. Teat and E. J. L. McInnes, *Angew. Chem. Int. Ed*, 2003, **42**, 3781.
79. P. A. Tasker, C. C. Tong and A. N. Westra, *Coord. Chem. Rev.*, 2007, **251**, 1868.
80. G. A. Kordosky, *Proc. Int. Solvent Extr. Conf.* , 2002, 853.
81. P. J. Mackey, *CIM Mag.*, 2007, **2**, 35.
82. R. S. Forgan, B. D. Roach, P. A. Wood, F. J. White, J. Campbell, D. K. Henderson, E. Kamenetzky, F. E. McAllister, S. Parsons, E. Pidcock, P. Richardson, R. M. Swart and P. A. Tasker, *Inorg. Chem.*, **50**, 4515.
83. R. S. Forgan, P. A. Wood, J. Campbell, D. K. Henderson, F. E. McAllister, S. Parsons, E. Pidcock, R. M. Swart and P. A. Tasker, *Chem. Commun.*, 2007, 4940.
84. M. Wenzel, R. S. Forgan, A. Faure, K. Mason, P. A. Tasker, S. Piligkos, E. K. Brechin and P. G. Plieger, *Eur. J. Inorg. Chem.*, 2009, **2009**, 4613.
85. M. Wenzel, Q. W. Knapp and P. G. Plieger, *Chem. Commun.*, 2011, **47**, 499.
86. A. G. Smith, P. A. Tasker and D. J. White, *Coord. Chem. Rev.*, 2003, **241**, 61.
87. M. Manoli, R. Inglis, M. J. Manos, V. Nastopoulos, W. Wernsdorfer, E. K. Brechin and A. J. Tasiopoulos, *Angew. Chem. Int. Ed*, 2011, **50**, 4441.
88. K. Mason, I. A. Gass, F. J. White, G. S. Papaefstathiou, E. K. Brechin and P. A. Tasker, *Dalton Trans.*, 2011, **40**, 2875.
89. P. Chaudhuri, M. Hess, E. Rentschler, T. Weyhermuller and U. Flörke, *New J. Chem.*, 1998, **22**, 553.
90. R. Inglis, C. J. Milios, L. F. Jones, S. Piligkos and E. K. Brechin, *Chem. Commun.*, 2011, *Advanced Article*. And references therein.
91. C. J. Milios, C. P. Raptopoulou, A. Terzis, F. Lloret, R. Vicente, S. P. Perlepes and A. Escuer, *Angew. Chem. Int. Ed*, 2004, **43**, 210.
92. C. J. Milios, R. Inglis, A. Vinslava, R. Bagai, W. Wernsdorfer, S. Parsons, S. P. Perlepes, G. Christou and E. K. Brechin, *J. Am. Chem. Soc.*, 2007, **129**, 12505.
93. C. J. Milios, A. Vinslava, W. Wernsdorfer, A. Prescimone, P. A. Wood, S. Parsons, S. P. Perlepes, G. Christou and E. K. Brechin, *J. Am. Chem. Soc.*, 2007, **129**, 6547.
94. J. D. Rinehart, M. Fang, W. J. Evans and J. R. Long, *Nat Chem*, 2011, **3**, 538.

95. C. J. Milios, A. Vinslava, W. Wernsdorfer, S. Moggach, S. Parsons, S. P. Perlepes, G. Christou and E. K. Brechin, *J. Am. Chem. Soc.*, 2007, **129**, 2754.
96. R. Inglis, L. F. Jones, G. Karotsis, A. Collins, S. Parsons, S. P. Perlepes, W. Wernsdorfer and E. K. Brechin, *Chem. Commun.*, 2008, 5924.
97. R. Inglis, L. F. Jones, K. Mason, A. Collins, S. A. Moggach, S. Parsons, S. P. Perlepes, W. Wernsdorfer and E. K. Brechin, *Chem. Eur. J*, 2008, **14**, 9117.
98. R. Inglis, S. M. Taylor, L. F. Jones, G. S. Papaefstathiou, S. P. Perlepes, S. Datta, S. Hill, W. Wernsdorfer and E. K. Brechin, *Dalton Trans.*, 2009, **42**, 9157.
99. R. Inglis, S. J. Dalgarno and E. K. Brechin, *Dalton Trans.*, 2010, **39**, 4826.
100. L. F. Jones, R. Inglis, M. E. Cochrane, K. Mason, A. Collins, S. Parsons, S. P. Perlepes and E. K. Brechin, *Dalton Trans.*, 2008, **44**, 6205.
101. J. M. Thorpe, R. L. Beddoes, D. Collison, C. D. Garner, M. Helliwell, J. M. Holmes and P. A. Tasker, *Angew. Chem. Int. Ed*, 1999, **38**, 1119.
102. C. W. Bennett and W. S. Burnham, *J. Phys. Chem.*, 1916, **21**, 107.
103. D. A. Jones, *Principles and Prevention of Corrosion*, Prentice-Hall International (UK) Ltd, 1996.
104. P. A. Schweitzer, *Corrosion and corrosion protection handbook*, M. Dekker, 1989.
105. F. J. White, PhD Thesis, University of Edinburgh, 2008.
106. E. Bill, C. Krebs, M. Winter, M. Gerdan, A. X. Trautwein, U. Flörke, H.-J. Haupt and P. Chaudhuri, *Chem. Eur. J*, 1997, **3**, 193.
107. P. Chaudhuri, E. Rentschler, F. Birkelbach, C. Krebs, E. Bill, T. Weyhermüller and U. Flörke, *Eur. J. Inorg. Chem.*, 2003, **2003**, 541.
108. P. Chaudhuri, M. Winter, P. Fleischhauer, W. Haase, U. Flörke and H.-J. r. Haupt, *Inorg. Chim. Acta*, 1993, **212**, 241.
109. I. A. Gass, C. J. Milios, A. Collins, F. J. White, L. Budd, S. Parsons, M. Murrie, S. P. Perlepes and E. K. Brechin, *Dalton Trans.*, 2008, **15**, 2043.
110. I. A. Gass, C. J. Milios, A. G. Whittaker, F. P. A. Fabiani, S. Parsons, M. Murrie, S. P. Perlepes and E. K. Brechin, *Inorg. Chem.*, 2006, **45**, 5281.
111. C. P. Raptopoulou, A. K. Boudalis, Y. Sanakis, V. Psycharis, J. M. Clemente-Juan, M. Fardis, G. Diamantopoulos and G. Papavassiliou, *Inorg. Chem.*, 2006, **45**, 2317.
112. C. P. Raptopoulou, Y. Sanakis, A. K. Boudalis and V. Psycharis, *Polyhedron*, 2005, **24**, 711.
113. C. N. Verani, E. Bothe, D. Burdinski, T. Weyhermüller, U. Flörke and P. Chaudhuri, *Eur. J. Inorg. Chem.*, 2001, **2001**, 2161.

Chapter 2
Building Fe^{III} clusters with Derivatised Salicylaldoximes

2.1 Introduction

As stated in the previous chapter polymetallic clusters of iron are being synthesised and studied for a host of reasons. This chapter will describe the synthesis, structures and magnetic properties of fifteen iron clusters stabilised by derivatised salicylaldoximes (Scheme 1). Previous work with manganese and these ligands has identified $[Mn_3O(sao)_3]^+$ as the predominant building block, which is not perturbed by increasingly complex reaction conditions.[1-6] The literature on Fe-salicylaldoxime complexes preceding this work and the work of the Brechin group is relatively limited, with only eleven crystallographically identified structures and no derivatised salicyladoxime complexes.[7-16] The aim of this work therefore is to expand the current family of Fe-salicylaldoxime structures and investigate the coordination modes and magnetism of the complexes. The role that the ketoxime group has in controlling the structure and core growth of the cluster will be examined. This will provide us with an understanding of specific metal cores and ligand binding modes attainable with the different salicylaldoxime ligands.

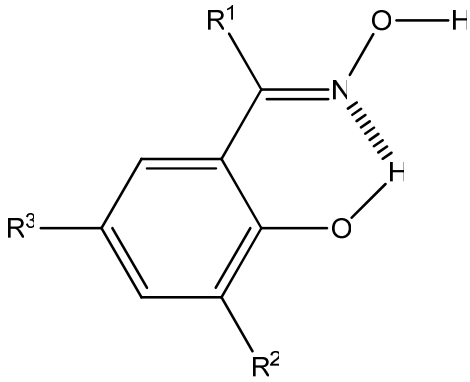

	R^1	R^2	R^3
$saoH_2$	H	H	H
Me-$saoH_2$	Me	H	H
Et-$saoH_2$	Et	H	H
Ph-$saoH_2$	Ph	H	H
^{t}But-$saoH_2$	H	^{t}But	H
3-^{t}But-5-NO_2-$saoH_2$	H	^{t}But	NO_2

Scheme 1 General structure of derivatised salicylaldoximes discussed in this chapter.

2.2 Experimental

2.2.1 Syntheses

All manipulations were performed under aerobic conditions using chemicals as received, unless otherwise stated.

CAUTION! Care should be taken when using the potentially explosive perchlorate anion. 2-Hydroxyacetophenone oxime (Me-saoH_2), 2-hydroxypropiophenone oxime (Et-saoH_2) and 2-hydroxybenzophenone oxime (Ph-saoH_2) were synthesised *via* the reaction of the appropriate ketone with hydroxylamine and sodium acetate in EtOH, as described in the literature.[17] Complexes **4**, **5**, **8**, **9** and **14** have been reported previously[10, 18] but are included here to aid discussion.

[Fe_3O(OMe)(Ph-sao)$_2Cl_2$(py)$_3$]·2MeOH (**1**·2MeOH).

$FeCl_3.6H_2O$ (405 mg, 1.50 mmol) and Ph-saoH_2 (213 mg, 1.00 mmol) were dissolved in a mixture of MeOH (25 ml) and pyridine (5 ml). After 120 mins stirring the solution was filtered and left to evaporate slowly, producing X-ray quality crystals after 3 days in approximately 50% yield. The dried sample analysed as **1**·MeOH. Found (calc.%): $C_{43}H_{40}Cl_2Fe_3N_5O_7$; C 52.39 (52.85), H 3.91 (4.13), N 7.45 (7.17). IR data (KBr pellet; cm^{-1}): 1593s, 1557m, 1514m, 1487s, 1429s, 1314s, 1249m, 1148m, 1037s, 959s, 855m, 758s, 699s, 665s, 582m, 462m.

[Fe_3O(OMe)(Ph-sao)$_2Br_2$(py)$_3$]·Et_2O (**2**·Et_2O).

$FeBr_3$ (296mg, 1.00 mmol) and Ph-saoH_2 (213 mg, 1.00 mmol) were dissolved in a mixture of MeOH (25 ml) and pyridine (5 ml). After 120 mins stirring the solution was filtered and diffused with Et_2O, producing X-ray quality crystals after 2 weeks in approximately 30% yield. The dried sample analysed as **2**. Found (calc.%): $C_{42}H_{36}Br_2Fe_3N_5O_6$; C 49.15 (48.78), H 3.94 (3.51), N 6.55 (6.77). IR data (KBr pellet; cm^{-1}): 1592s, 1558m, 1514m, 1487s, 1428s, 1310s, 1248m, 1148m, 1037s, 958s, 854m, 758s, 700s, 665s, 582m, 462m.

$[Fe_4(Ph\text{-}sao)_4F_4(py)_4]\cdot 1.5MeOH$ (**3**·1.5MeOH).

$FeF_3.3H_2O$ (167 mg, 1.00 mmol) and Ph-saoH_2 (213 mg, 1.00mmol) were dissolved in a mixture of MeOH (25 ml) and pyridine (5 ml). After 180 mins stirring, the solution was filtered and left to evaporate slowly, producing X-ray quality crystals after 1 week, in approximately 30% yield. The dried sample analysed as **3**. Found (calc.%): $C_{72}H_{56}F_4Fe_4N_8O_8$; C 58.95 (59.21), H 3.47 (3.86), N 7.45 (7.67). IR data (KBr pellet; cm^{-1}): 1592s, 1560m, 1521m, 1488m, 1433s, 1319s, 1255m, 1147m, 1039s, 957s, 855m, 750s, 696s, 660s, 546m, 460m.

$[Fe_6O_2(OH)_2(Et\text{-}sao)_2(Et\text{-}saoH)_2(O_2CPh)_6]$ (**4**).[18, 19]

$FeCl_3\cdot 6H_2O$ (135 mg, 0.5 mmol), Et-saoH_2 (82.5 mg, 0.5 mmol), NaO_2CPh (216 mg, 1.5 mmol) were dissolved in MeCN (25 ml) in the presence of NEt_3 (0.25 ml, 0.2 mmol) and heated to 50°C. After 90 mins stirring the solution was filtered and then layered with Et_2O to produce X-ray quality crystals in 2 weeks. The crystals were collected by filtration and dried *in vacuo.* The yield was approximately 55%. The dried sample analysed as **4**. Found (calc.%): $C_{84}H_{85}Fe_6N_5O_{24}$; C 53.87 (53.56), H 4.72 (4.55), N 3.96 (3.72). IR data (KBr pellet; cm^{-1}): 1599s, 1560s, 1400s, 1313m, 1254m, 1070m, 1016m, 935m, 839m, 793m, 752m, 717s, 671m, 638m, 586m, 513m, 467s.

$[HNEt_3]_2[Fe_6O_2(OH)_2(Et\text{-}sao)_4(O_2CPh(Me)_2)_6]\cdot 2MeCN$ (**5**·2MeCN).[18, 19]

$FeCl_3\cdot 6H_2O$ (270 mg, 1.0 mmol), Et-saoH_2 (165 mg, 1.0 mmol) and $NaO_2CPh(Me)_2$ (sodium 3,5-dimethylbenzoate, 158 mg, 1.0 mmol) were dissolved in MeCN (30 ml) in the presence of NEt_3 (1.0 ml, 8.0 mmol) and heated to 50°C. After 120 mins stirring the solution was filtered and the solution left to evaporate slowly at room temperature. X-ray quality crystals formed in 2 weeks. The crystals were collected by filtration and dried *in vacuo.* The yield was approximately 30%. The dried sample analysed as **5**·MeCN. Found (calc.%): $C_{104}H_{127}Fe_6N_7O_{24}$; C 56.49 (56.93), H 5.81 (5.83), N 4.72 (4.47). IR data (KBr pellet; cm^{-1}): 1568s, 1431s, 1398s, 1309m, 1267m, 1076m, 1053m, 931m, 841m, 789m, 752s, 648m, 598m, 509m, 465s.

$[Fe_6O_2(O_2CPh)_{10}(3\text{-}^tBut\text{-}5\text{-}NO_2\text{-}sao)_2(H_2O)_2]\cdot 4MeCN$ (**6**·4MeCN).

$[Fe_3O(O_2CPh)_6(H_2O)_3]NO_3$ (500 mg, 0.48 mmol), ^{t}But-saoH_2 (94 mg, 0.48 mmol) were dissolved in MeCN (25 ml). After 120 minutes stirring the solution was filtered and left to evaporate slowly producing X-ray quality crystals after 1 week in approximately 30% yield. The dried sample analysed as **6**·MeCN. Found (calc.%): $C_{92}H_{78}Fe_6N_4O_{32}$; C 52.69 (52.95), H 3.74 (3.77), N 2.87 (2.68). IR data (KBr pellet; cm^{-1}): 1599s, 1554s, 1493s, 1408s, 1306s, 1176m, 1113m, 1026m, 843m, 717s, 673m, 615m, 480s.

$[Fe_6O_2(O_2CCH_2Ph)_{10}(3\text{-}^tBut\text{-}sao)_2(H_2O)_2]\cdot 5MeCN$ (**7**·5MeCN).

$[Fe_3O(O_2CCH_2Ph)_6(H_2O)_3]NO_3$ (100 mg, 0.09 mmol), 3-^{t}But-saoH_2 (18 mg, 0.09 mmol) were dissolved in MeCN (25 ml). After 180 mins stirring the solution was filtered and left to evaporate slowly producing X-ray quality crystals after 1 week in approximately 30% yield. The dried sample analysed as **7**·MeCN. Found (calc.%): $C_{102}H_{100}Fe_6N_2O_{28}$; C 56.98 (57.33), H 4.25 (4.72), N 1.68 (1.31). IR data (KBr pellet; cm^{-1}): 1576s, 1496m, 1410s, 1298m, 1194m, 999m, 962m, 876m, 752m, 727m, 642m, 575m, 546m, 501m.

$\{[Fe_6Na_3O(OH)_4(Me\text{-}sao)_6(OMe)_3(H_2O)_3(MeOH)_6]\cdot MeOH\}_n$ (**8**·MeOH).[18, 19]

Method 1: $Fe(ClO_4)_2\cdot 6H_2O$ (182.5 mg, 0.5 mmol), Me-saoH_2 (151 mg, 1.0 mmol) and NaO_2CCHCl_3 (185 mg, 1.0 mmol) were dissolved in MeOH (25 ml) in the presence of NEt_3 (1.0 ml, 8 mmol). After 180 mins stirring the solution was filtered and then left to slowly evaporate, producing X-ray quality crystals in 4 days. The crystals were collected by filtration and dried *in vacuo.* The yield was approximately 65%. The dried sample analysed as **8**. Found (calc. %): $C_{57}H_{84}Fe_6Na_3N_6O_{29}$; C 39.43 (39.77), H 4.54 (4.92), N 5.18 (4.88). IR data (KBr pellet; cm^{-1}): 1630m, 1593m, 1568m, 1531m, 1473m, 1435s, 1306s, 1250m, 1130m, 1024s, 962m, 856m, 752s, 665s, 611m, 449m, 415m.

Method 2: $Fe(O_2CMe)_2\cdot 6H_2O$ (174 mg, 1.0 mmol), Me-saoH_2 (151 mg, 1.0 mmol), NaOMe (324 mg, 6.0 mmol) were dissolved in MeOH (25 ml). After 120 mins

stirring the solution was filtered and then left to evaporate slowly, producing X-ray quality crystals in 3 days. The crystals were collected by filtration and dried *in vacuo.* The yield was approximately 50%. The dried sample analysed satisfactorily as solvent free **8**.

Method 3: $FeCl_3 \cdot 6H_2O$ (270 mg, 1.0 mmol), Me-saoH_2 (302 mg, 2.0 mmol), NaOMe (216 mg, 4.0 mmol) were dissolved in MeOH (25 ml). After 120 mins stirring the solution was filtered and then left to evaporate slowly, producing X-ray quality crystals in 4 days. The crystals were collected by filtration and dried *in vacuo.* The yield was approximately 50%. The dried sample analysed satisfactorily as solvent free **8**.

Method 4: $Fe(ClO_4)_2 \cdot 6H_2O$ (182.5 mg, 0.5 mmol), Me-saoH_2 (151 mg, 1.0 mmol), NaO_2CCHBr_3 (319 mg, 1.0 mmol) were dissolved in MeOH (25 ml) in the presence of NEt_4OH (1.0M in water; 0.125 ml, 0.125 mmol). After 120 mins stirring the solution was filtered and then left to evaporate slowly, producing X-ray quality crystals in 3 days. The crystals were collected by filtration and dried *in vacuo.* The yield was approximately 55%. The dried sample analysed satisfactorily as solvent free **8**.

$[HNEt_3]_2[Fe_{12}Na_4O_2(OH)_8(sao)_{12}(OMe)_6(MeOH)_{10}]$ (9).[18, 19]

$Fe(ClO_4)_2 \cdot 6H_2O$ (365 mg, 1.0 mmol), saoH_2 (137 mg, 1.0 mmol), NaO_2CHBr_3 (319 mg, 1.0 mmol) were dissolved in MeOH in the presence of NEt_3 (0.125 ml, 1 mmol). After 180 mins stirring the solution was filtered and then left to evaporate slowly producing X-ray quality crystals in 3 days. The crystals were collected by filtration and dried *in vacuo.* The yield was approximately 30%. The dried sample analysed as **9**. Found (calc. %): $C_{112}H_{156}Fe_{12}Na_4N_{14}O_{50}$; CHN; C 40.92 (41.26), H 4.46 (4.82), N 5.83 (6.01). IR data (KBr pellet; cm^{-1}): 1593s, 1543m, 1473m, 1437m, 1321m, 1290s, 1200m, 1153m, 1120m, 1018m, 916s, 818m, 764s, 665m, 607m.

$[Fe_8O_2(OMe)_4(Me\text{-}sao)_6Br_4(py)_4]\cdot 2Et_2O\cdot MeOH$ (**10**·$2Et_2O$·MeOH).

$FeBr_3$ (148 mg, 0.50 mmol) and Me-saoH_2 (226.5 mg, 1.50 mmol) were dissolved in MeOH (25ml) in the presence of pyridine (2ml). The dark red solution was stirred for 2 hours, filtered and then diffused with Et_2O, producing X-ray quality crystals after 1 week, in approximately 20% yield. Elemental analysis found (calc. %) for $C_{81}H_{98}Br_4Fe_8N_{10}O_{21}$: C 41.73 (42.04), H 4.16 (4.27), N 5.97 (6.05).

$[Fe_8O_2(OMe)_{3.85}(N_3)_{4.15}(Me\text{-}sao)_6(py)_2]$ (**11**).

$FeF_3\cdot 3H_20$ (167 mg, 1.00 mmol) and Me-saoH_2 (151mg, 1.00 mmol) were dissolved in a mixture of MeOH (25ml) and pyridine (2 ml) and stirred for 5 mins. NaN_3 (130 mg, 2.00 mmol) was then added and the dark red solution stirred for a further 120 minutes. The solution was filtered and left to evaporate slowly, producing X-ray quality crystals after 3 days in approximately 20% yield. Elemental analysis found (calc. %) for $C_{72}H_{73}Fe_8N_{23}O_{18}$: C 43.14 (43.34), H 3.42 (3.69), N 16.02 (16.15).

$[Fe_6O_2(OMe)_4(O_2CPh\text{-}4\text{-}NO_2)_4(Me\text{-}sao)_2Cl_2(py)_2]$ (**12**).

$FeCl_3\cdot 6H_2O$ (270 mg, 1.00 mmol), Me-saoH_2 (151 mg, 1.00 mmol) and NaO_2CPh-4-NO_2 (189 mg, 1.00 mmol) were dissolved in MeOH (25 ml) in the presence of pyridine (2ml). The dark red solution was stirred for 2 hours, filtered and then diffused with Et_2O, producing X-ray quality crystals after 1 week. The yield was aproximately 30%. Elemental analysis found (calc. %) for $C_{61}H_{61}Cl_2Fe_6N_8O_{28}$: C 40.94 (41.26), H 3.05 (3.49), N 6.26 (6.37).

$[Fe_6O_2(OMe)_4(O_2CPh\text{-}4\text{-}NO_2)_4(Et\text{-}sao)_2Cl_2(py)_2]\cdot 2Et_2O\cdot MeOH$ (**13**·$2Et_2O$·MeOH).

Synthesis was identical to that of compound **12** using Et-saoH_2 (165 mg, 1.00 mmol) instead of Me-saoH_2. The yield was approximately 30%. Elemental analysis found (calc. %) for $C_{69}H_{80}Cl_2Fe_6N_8O_{29}$: C 43.45 (43.82), H 4.04 (4.26), N 5.77 (5.92).

$[HNEt_3]_2[Fe_6O_2(OMe)_4(Me\text{-}sao)_4(SO_4)_2(MeOH)_2]$ (14).[10, 18]

$Fe_2(SO_4)_3 \cdot 6H_2O$ (508 mg, 1.00 mmol) and Me-saoH_2 (151 mg, 1.00 mmol) were dissolved in a solution of MeOH (30 ml) in the presence of NEt_3 (404 mg, 4 mmol). The solution was stirred for 1 hour and then diffused with Et_2O, producing X-ray quality crystals after 3 days. The yield was approximately 30%. Elemental analysis found (calc. %) for $C_{50}H_{80}Fe_6N_6O_{24}S_2$: C 38.96 (38.78), H 5.10 (5.21), N 5.38 (5.43).

$[HNEt_3]_2[Fe_6O_2(OMe)_4(Et\text{-}sao)_4(SO_4)_2(MeOH)_2]$ (15).

Synthesis was identical to **14** using Et-saoH_2 (165 mg, 1.00 mmol) instead of Me-saoH_2. The yield was approximately 30%. Elemental analysis found (calc. %) for $C_{54}H_{88}Fe_6N_6O_{24}S_2$: C 40.38 (40.42), H 5.24 (5.53), N 5.20 (5.24).

2.2.2 X-Ray crystallography and structure solution

Diffraction data were collected on a Bruker Smart Apex CCD diffractometer equipped with an Oxford Cryosystems LT device, using Mo-Kα radiation. Data collection parameters and structure solution and refinement details are listed in Tables 1a, 1b and 1c. Full details can be found in the CIF files provided in the attached CD.

2.2.3 Physical Measurements

Elemental analyses (C, H, N) were performed by the EaStCHEM microanalysis service. IR spectra were recorded as KBr pellets in the 4000-400 cm^{-1} range on a JASCO FT/IR-410 spectrometer. Variable temperature magnetic susceptibility measurements were made on a Quantum Design MPMS-XL SQUID magnetometer equipped with a 7 T magnet. Data were collected on powdered samples restrained in eicosane to prevent torquing. Diamagnetic corrections were applied using Pascal's constants.

2.3 Results and Discussion

2.3.1 Synthesis

The reaction of $FeCl_3.6H_2O$ with Ph-saoH_2 in a 3:2 molar ratio in a MeOH/pyridine solution yields the trinuclear complex [Fe_3O(OMe)(Ph-sao)$_2Cl_2(py)_3$] (**1**). Repeating the reaction with $FeBr_3$ in place of $FeCl_3.6H_2O$ affords the bromide analogue [Fe_3O(MeO)(Ph-sao)$_2Br_2(py)_3$] (**2**), but the use of $FeF_3.3H_2O$ in the same reaction leads to the tetranuclear complex [Fe_4(Ph-sao)$_4F_4(py)_4$] (**3**), in which the halide ions bridge between metals rather than bonding terminally as in **1** and **2**. A combination of the bulky Ph-sao^{2-} ligand and the coordinating pyridine appears to favour the production of low nuclearity complexes, but the introduction of carboxylates tends to favour larger species. For example reaction of $FeCl_3.6H_2O$ with Et-saoH_2 and NaO_2CPh in the presence of NEt_3 yields the hexanuclear complex [Fe_6O_2(OH)$_2$(Et-sao)$_2$(Et-saoH)$_2(O_2CPh)_6$] (**4**). The low ratio of base employed results in **4** containing two singly deprotonated Et-saoH$^-$ lgands. Increasing this ratio allows us to fully deprotonate all four ligands yielding the hexanuclear complex [$HNEt_3$]$_2$[Fe_6O_2(OH)$_2$(Et-sao)$_4(O_2CPh(Me)_2)_6$] (**5**). The increase in the amount of base employed also leads to the presence of two bridging hydroxides which link the two triangles (*vide infra*). This type of structure has been seen in previously reported carboxylate-only [Fe^{III}_6] clusters, suggesting that oximes could potentially be employed as direct replacements for carboxylates in many other known polymetallic Fe-carboxylate clusters.[12, 13] The similarity between the carboxylate coordination in **4** and **5** and the basic Fe(III) carboxylates of general formula [$Fe_3O(O_2CR)_6L_3$]$^+$ (L = solvent) led to the idea that we could start with pre-made iron carboxylate triangles and replace the carboxylates with oximes, to create similar complexes. Indeed treatment of [$Fe_3O(O_2CPh)_6(H_2O)_3$]NO_3 with 3-^{t}But-saoH_2 yields the complex [$Fe_6O_2(O_2CPh)_{10}$(3-^{t}But-5-NO_2-sao)$_2(H_2O)_2$] (**6**). Four carboxylates have been replaced with two oximes which crosslink the two triangles (vide infra), in a manner identical to work previously reported by Boudalis et al.[12] A peculiar anomaly in this instance is that the 3-^{t}But-sao^{2-} ligand has undergone an *in situ* nitration at the 5 position. Although never seen before in our work there is precedent for this in organic literature.[20, 21] Repeating this reaction with [$Fe_3O(O_2CCH_2Ph)_6(H_2O)_3$]$NO_3$

yields the analogous complex $[Fe_6O_2(O_2CCH_2Ph)_{10}(3\text{-}^tBut\text{-}sao)_2(H_2O)_2]$ (**7**) in which there is no ligand nitration.

The reaction of $Fe(ClO_4)_2.4H_2O$ with Me-saoH_2 and NaO_2CCCl_3 and NEt_3 yields the polymeric $([Fe_6Na_3O(OH)_4(Me\text{-}sao)_6(OMe)_3(H_2O)_3(MeOH)_6]\cdot MeOH)_n$ (**8**·MeOH), in which carboxylate does not feature. This is presumably a result of its highly acidic nature, acting solely as a source of Na. Indeed the complex can also be obtained by introducing the Na^+ using excess NaOMe. Repeating the reaction but reducing the bulk of the oxime produces the related, but unusual, molecular complex $[HNEt_3]_2[Fe_{12}Na_4O_2(OH)_8(sao)_{12}(OMe)_6(MeOH)_{10}]$ (**9**).

Reacting $FeBr_3$ with Me-saoH_2 in a 1:3 ratio in a MeOH/pyridine solution yields the octanuclear complex $[Fe_8O_2(OMe)_4(Me\text{-}sao)_6Br_4(py)_4]$ (**10**), which has a metallic skeleton of two edge-sharing $[Fe_4O]$ tetrahedra, edge-capped by two additional Fe^{3+} ions. The oxime ligand displays a μ_4-coordination mode - the first time this has been observed. The reaction is the same as **1**, **2** and **3** but changing from Ph-saoH_2 to the less bulky Me-saoH_2, demonstrating the importance of the bulkier ketoxime group in restricting the size of the cluster. We can replace the terminal bromide ligands with terminal azides by simply introducing NaN_3 into the reaction mixture. This also has the effect of partially substituting a μ-methoxide bridge with an end-on μ-azide bridge affording the complex $[Fe_8O_2(OMe)_{3.85}(N_3)_{4.15}(Me\text{-}sao)_6(py)_2]$ (**11**). Further attempts to fully substitute the μ-methoxide bridges have proved unsuccessful, even when employing a large excess of NaN_3. Attempts to repeat these reactions with other iron halide salts have failed thus far. It is interesting to note that (in Fe^{3+} chemistry) only two examples of end-on bridging azides appear in the CCDC database – and both display ferromagnetic exchange coupling between the Fe^{3+} centres.[22, 23]

Introducing carboxylates (in the form of $Na(O_2CPh\text{-}4\text{-}NO_2)$) to the reaction of $FeCl_3\cdot 6H_2O$ and Me-saoH_2 in a 1:1:1 ratio in a MeOH/py solution leads to the related but lower nuclearity hexanuclear complex $[Fe_6O_2(OMe)_4Cl_2(O_2CPh\text{-}4\text{-}NO_2)_4(Me\text{-}sao)_2(py)_2]$ (**12**). The core again consists of two edge sharing tetrahedra but the replacement of the μ_4-bridging oximes with μ-bridging carboxylates prevents

the addition of two additional edge-capping Fe^{3+} ions. Repeating the same reaction with Et-saoH_2 instead of Me-saoH_2 simply gives the analogous compound, $[Fe_6O_2(OMe)_4(O_2CPh\text{-}4\text{-}NO_2)_4(Et\text{-}sao)_2Cl_2(py)_2]$ (**13**). Despite many attempts, we failed to isolate compounds with carboxylates other than 4-NO_2-benzoate. It is unclear why this should be so, but we presume it to be due to the steric bulk of the 4-substituent and/or the stabilising inter-molecular interactions propagated between neighbouring NO_2 groups (*vide infra*).

The introduction of co-ligands, such as carboxylates, thus appears to favour the formation of smaller clusters and μ-coordination of the phenolic oxime. This is corroborated when sulfate anions are introduced to the reaction mixture. The reaction of $Fe_2(SO_4)_3{\cdot}6H_2O$ with Me-saoH_2 or Et-saoH_2 in the presence of NEt_3 in MeOH produces the hexanuclear complexes $[HNEt_3]_2[Fe_6O_2(Me\text{-}sao)_4(SO_4)_2(OMe)_4(MeOH)_2]$ (**14**) and $[HNEt_3]_2[Fe_6O_2(Et\text{-}sao)_4(SO_4)_2(OMe)_4(MeOH)_2]$ (**15**). The metallic core of both (analogous) molecules again comprises two edge-sharing $[Fe_4O]$ tetrahedra but on this occasion each tripodal SO_4^{2-} anion caps one of the triangular faces of the tetrahedron, preventing further growth.

2.3.2 Description of Structures

Complexes **1-15** are shown in Figures 1-11. Full details of the bond lengths and angles are given in the CIF files provided in the attached CD. Complexes **1** and **2** are isostructural, differing only in the identity of the halide and so here we describe only complex **1** in detail. This crystallises in the monoclinic space group $P2_1/c$ with four molecules in the unit cell. It consists of a $[Fe^{III}_3(\mu_3\text{-}O)]$ triangular unit where the Fe1-Fe2 and Fe1-Fe3 edges are each bridged by a fully deprotonated Ph-sao^{2-} ligand in a η^1: η^1: η^1: μ_2 fashion. The Fe2-Fe3 edge is bridged by one μ-MeO^- ion (Fe2-O1F-Fe3, 98.84(13)°). The remaining coordination sites on Fe1 are occupied by three pyridine molecules. Fe2 and Fe3 are five coordinate and the remaining site in each is occupied by a halide (**1**=Cl, **2**=Br). The Fe···Fe separations and Fe- μ_3-O-Fe angles are unequal (3.3552(8) Å, 3.3834(8) Å, 3.0133(8) Å, 128.1(2)°, 126.6(2)°,

105.3(1)°) and so the triangle is truly scalene rather than isosceles. Fe1 is in a distorted octahedral geometry with *cis* angles in the range 81.7(1)-97.4(1)°, and *trans* angles in the range 166.5(1)-176.6(1)°. Fe2 and Fe3 are both in a distorted square based pyramidal geometry with a τ value of 0.190 (where τ = (β-α)/60),[24] their oxidation states assigned using charge balance considerations, bond lengths and BVS calculations.[25, 26] In the crystal lattice there are no intermolecular hydrogen bonds, with the closest contacts being between a pyridine ligand and the phenolic O-atom (C···O, 3.347(7) Å); Cl and the solvent MeOH (Cl···O, 3.365(6) Å); MeOH and a phenyl ring of the Ph-sao^{2-} ligand (O···C, 3.457(8) Å).

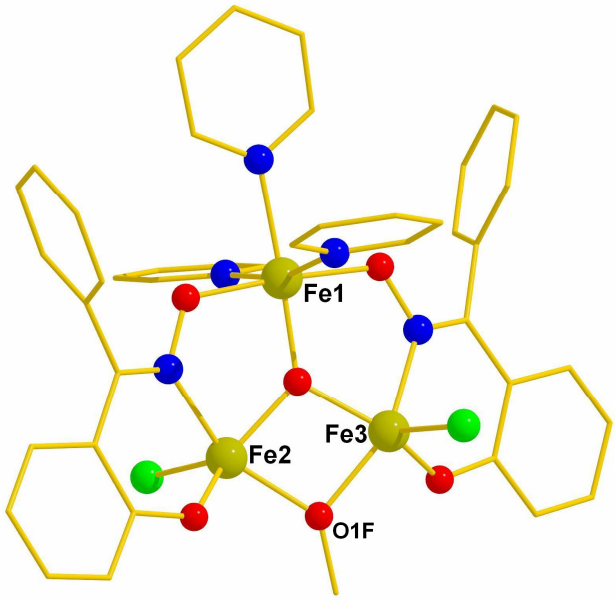

Fig. 1 The molecular structure of **1**. Colour code: Fe = olive green; O = red; N = blue; C = gold; Cl = bright green

Complex **3** (Fig. 2) crystallises in the monoclinic space group $P2_1/c$ with eight molecules in the unit cell, it contains two independent molecules in the asymmetric unit which vary slightly in bond lengths and angles but are structurally equivalent. The Fe^{III} ions are connected by a combination of four fully deprotonated Ph-sao^{2-} ligands in a η^1: η^1: η^1: μ_2-fashion and four μ_2-F^- ions creating an unusual [Fe_4] square. The remaining coordination site on each Fe^{III} is occupied by a pyridine

molecule. Each Fe^{III} ion is in a distorted octahedral geometry (*cis*, 82.1(2)-102.1(2)°; *trans,* 166.9(2)-178.3(2)°). The structure is unique in that it is the first case of a Fe^{III} square bridged through flouride, and to the best of our knowledge is one of only five fluoride-bridged first row transition metal squares.[27-31] In the crystal lattice there are no intermolecular hydrogen bonds, with the closest contacts being between pyridine ligands and phenolic O-atoms (C···O, 3.008(8)- 3.380(1) Å).

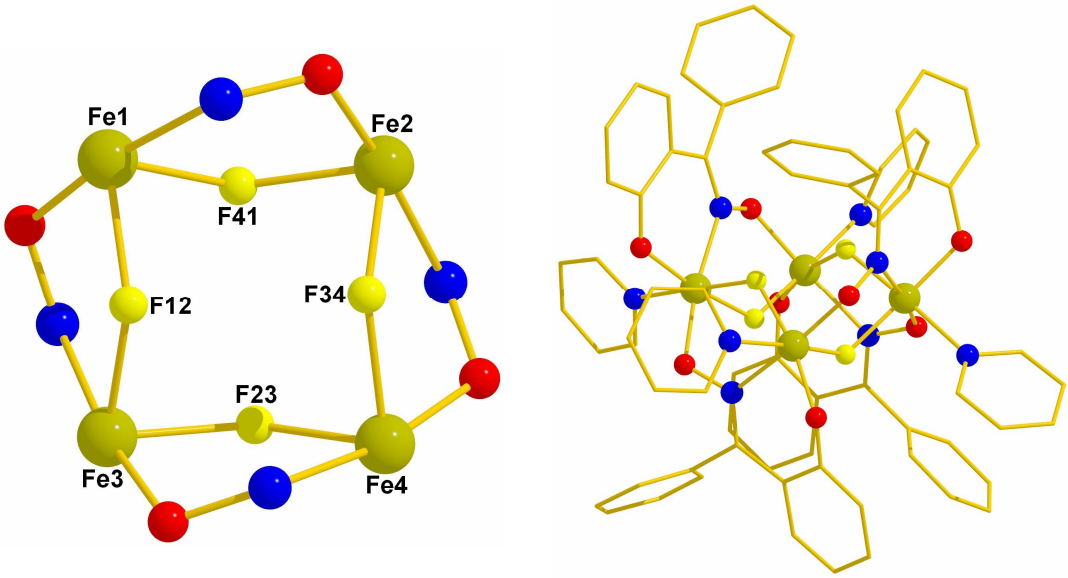

Fig. 2 The molecular structure of **3** (top) and its magnetic core (bottom). Colour code: Fe = olive green; O = red; N = blue; C = gold; F = yellow.

Complex **4** crystallises in the triclinic space group *P-1* with one molecule in the unit cell (Fig. 3). The molecule contains a $[Fe^{III}_6(\mu_3\text{-}O)_2(\mu\text{-}OH)_2]^{12+}$ core, whose topology consists of two centrosymmetricaly related off-set $[Fe^{III}_3(\mu_3\text{-}O)]$ triangular units linked at one Fe_2 edge (Fe1-Fe3) by two μ-OH^- ions and two oximate O atoms from two $\eta^1{:}\eta^1{:}\eta^2{:}\mu_3$-Et-saoH$^-$ ligands. Two Fe_2 edges (Fe2-Fe3) are each bridged by one oximate oxygen atom from one $\eta^1{:}\eta^1{:}\eta^1{:}\mu_2$-Et-sao^{2-} and one $PhCO_2^-$ ligand in its familiar syn, syn, μ_2-mode. The remaining two Fe_2 edges (Fe1-Fe2) are bridged by two $PhCO_2^-$ ligands. Each Fe^{III} ion lies in a distorted octahedral geometry (*cis*, 81.47(16)-105.51(17)°; *trans*, 161.79(16)-178.37(18)°). In the crystal lattice there are

no intermolecular hydrogen bonds, with the closest contacts being between two Et-sao^{2-} ligands and two phenolic O- atoms (C···O, 3.406(7) Å) which result in the formation of pseudo 1D chains in the bc-plane.

5 has a similar structure to **4** with the following differences: the two singly deprotonated Et-$saoH^-$ ligands in **4** are replaced by two fully (doubly) deprotonated Et-sao^{2-} ligands, which is perhaps to be expected given the larger amount of base used in the synthesis, with charge balance being maintained with the presence of two $[HNEt_3]^+$ cations. Again, the Fe^{III} ions lie in distorted octahedral geometries with *cis* angles in the range 80.46(15)-103.24(15)° and *trans* angles in the range 164.76(16)-177.27(15)°). In the crystal lattice there are inter molecular hydrogen bonding interactions between two phenolic O-atoms and the two cations (N···O, 2.793(8) Å) and close contacts between a phenolic O-atom and the cation (C···O, 3.533(8) Å) and between a $(Me)_2PhCO_2^-$ ligand and the cation (C···O, 3.271(11) Å). This results in the formation of 2D sheets lying in the *bc* plane, with the closest intermolecular Fe···Fe distance being 8.925(10) Å.

Complex **6** (Fig. 3) crystallises in the triclinic space group *P-1* with two molecules in the unit cell. The molecule is similar in structure to **4** except that the bridging between the two $[Fe^{III}_3(\mu_3\text{-}O)_2]$ triangular units occurs only through the two oximate O atoms, *i.e.* there are no μ-OH^- ions present, as in **4**. The oxime used in **6** was 3-^{t}But-$saoH_2$, but under the reaction conditions the benzene ring has become nitrated at the 5 position giving 3-^{t}But-5-NO_2-sao^{2-}.[20, 21] There are only two oximes present in **6** compared to the four in **4**, the edges that were bridged by one $\eta^1{:}\eta^1{:}\eta^1{:}\mu_2$-Et-$sao^{2-}$ and one $PhCO_2^-$ ligand in **4**, are now bridged by two $PhCO_2^-$ ligands in their familiar, syn, syn, μ-mode in **6**. In the crystal lattice there are intermolecular hydrogen bonds between the NO_2 salicylaldoxime and the H_2O (O···O, 2.803(1) Å) and between the H_2O and the MeCN solvent (N···O, 2.924(2) Å). Complex **7** crystallises in the monoclinic space group $P2_1/c$ and has a similar structure to **6** except there has been no nitration of the benzene ring. In the crystal lattice there are again intermolecular hydrogen bonds between the H_2O and the

MeCN solvent (N···O, 2.875(9) Å) and also between the H_2O and a carboxylate O-atom (O···O, 2.963(6) Å).

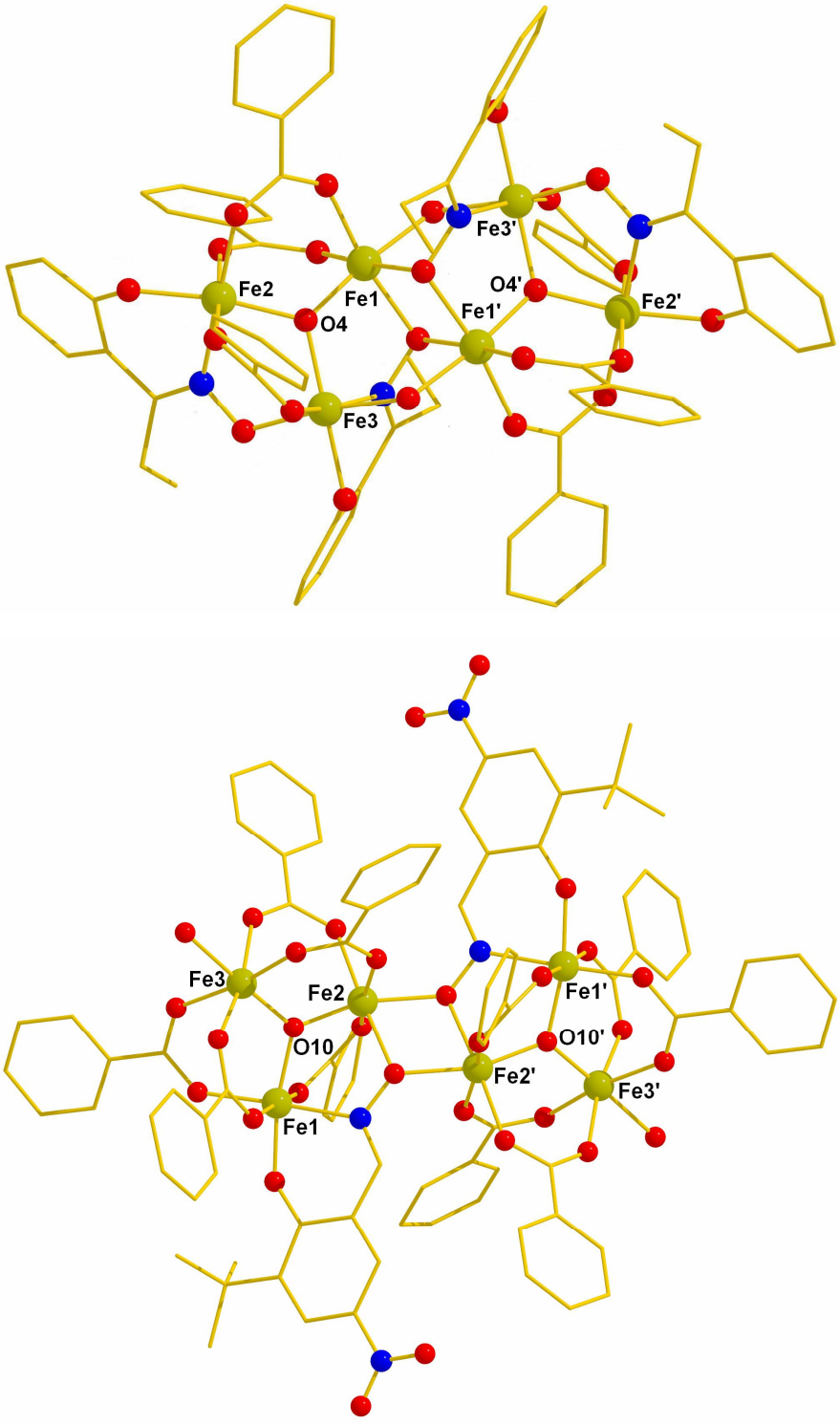

Fig. 3 The molecular structures of **4** (top) and **6** (bottom). Colour code as previous Figures.

8 crystallises in the hexagonal space group *P*63/m with two molecules in the unit cell and has a 2D framework structure (Fig. 4). The metallic skeleton of the $[Fe_6]$ unit (composed of two linked $[Fe_3(\mu_3\text{-}O)_{0.5}(\mu_3\text{-}OH)_{0.5}]^{7.5+}$ triangles) (Fig. 4) within the 2D framework describes a trigonal prism of Fe^{III} ions connected along the square faces via three $\mu_3\text{-}OH^-$ ions and three $\mu\text{-}MeO^-$ ions to form an $[Fe^{III}_6(\mu_3\text{-}O)(\mu_3\text{-}OH)_4(\mu\text{-}OMe)_3]^{9+}$ core. BVS calculations on O3 and symmetry equivalent (s.e) of the $[Fe_3(\mu_3\text{-}O)_{0.5}(\mu_3\text{-}OH)_{0.5}]^{+7.5}$ triangles reveal values that lie between those expected for O^{2-} and OH^- suggesting that a proton is shared between O3 and s.e. This is reasonable considering the short O···O distance of 2.472(3) Å between O3 and s.e indicative of a hydrogen bonding interaction. The six Fe_2 edges (Fe1-Fe1′ and s.e) of the triangular faces of the trigonal prism are each linked by a fully deprotonated Me-sao^{2-} ligand bridging in a $\eta^1{:}\eta^1{:}\eta^1{:}\mu_2$ fashion. Each Fe ion has a distorted octahedral geometry (*cis*, 76.94(6)-97.07(7)°; *trans*, 169.42(6)-172.01(6)°) with a 3+ oxidation state assigned using charge balance considerations, bond lengths and BVS calculations. The triangle of Na^+ ions in the $[Na_3]$ unit (Fig. 4) within the framework is connected via three $\mu\text{-}H_2O$ molecules on each edge. Each Na^+ ion is linked to the $[Fe_6]$ unit via a $\mu_3\text{-}OH^-$ ion; with six terminal methanol molecules completing the coordination sphere. The Na^+ ions define a distorted trigonal bipyramid with a τ value of 0.955.[24] Each $[Fe^{III}_6O(OH)_4(Me\text{-}sao)_6(OMe)_4]$ unit is linked to three $[Na_3(\mu_2\text{-}H_2O)_3(MeOH)_6]$ units forming a non interpenetrated 2D network with the centroid of O3 and s.e of the $[Fe^{III}_6O(OH)_4(Me\text{-}sao)_6(OMe)_4]$ unit and the centroid of the three Na^+ ions of the $[Na_3(\mu\text{-}OH_2)_3(MeOH)_6]$ unit forming two 3-connecting nodes of a (6,3) 2D net in the *ab*-plane. In the crystal lattice there are significant numbers of complementary hydrogen bonds: two between the terminally bound MeOH molecules and the oximato O-atoms (O···O, 2.742(3) Å); two between the phenolic O-atoms and bridging H_2O molecules; and one between a OH^- ion and a bridging MeO^- ion.

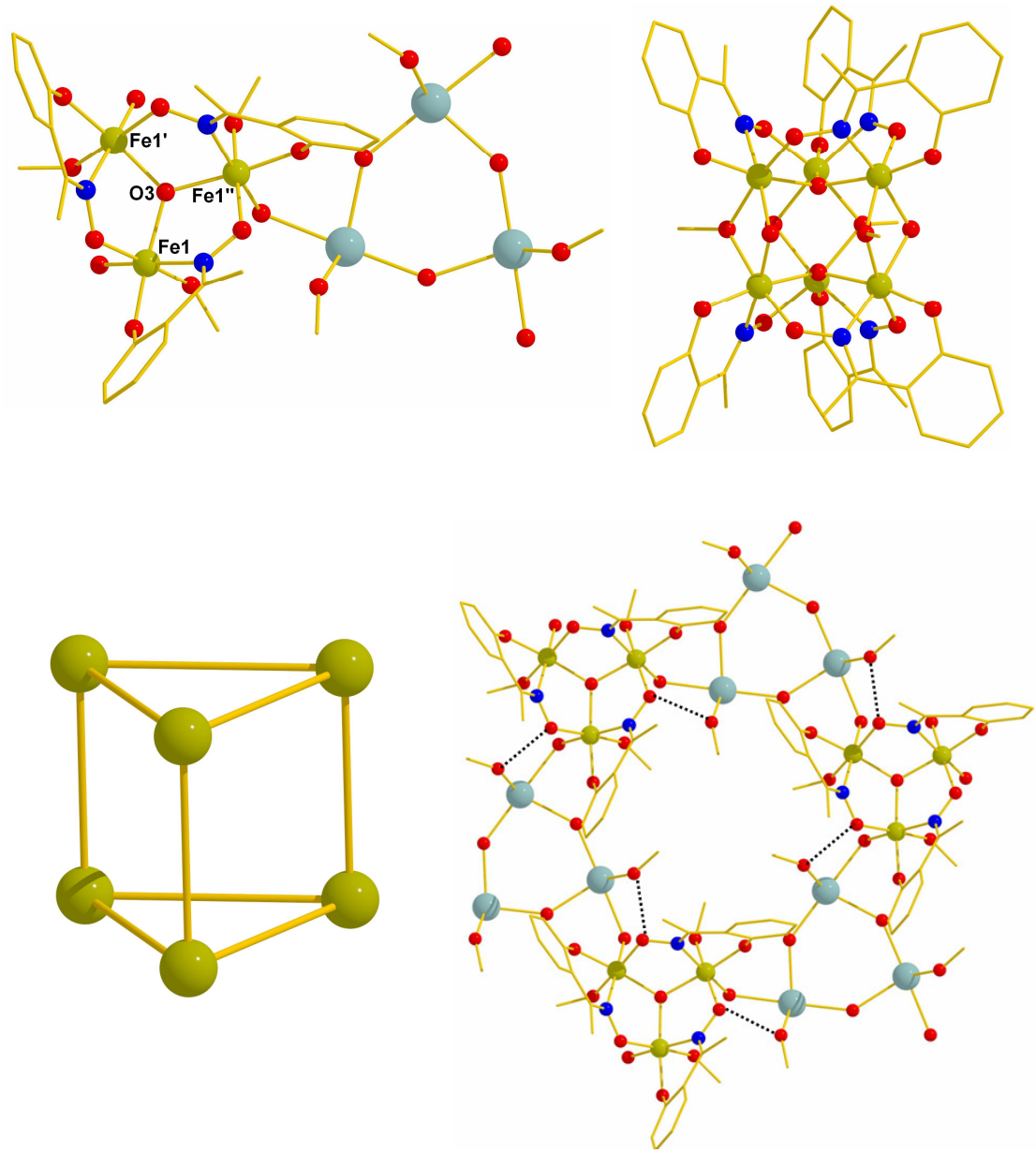

Fig. 4 The structure of the $[Fe_3Na_3]$ unit in **8** (top left), the $[Fe_6]$ trigonal prismatic unit viewed parallel to the $[Fe_3]$ planes (top right), the $[Fe_6]$ trigonal prismatic metal core (bottom left and the respective packing in the crystal as viewed down c-axis (bottom right). Colour code: Fe = green; Na = cyan O = red; N = blue; C = gold.

9 crystallises in the monoclinic space group $P2_1/c$ with two molecules in the unit cell (Fig. 5). The molecule contains two $[Fe_6Na]$ units linked by a single central $[Na_2]$ unit forming an unusual S-shaped molecule. This is structurally very similar to

8 except that a single Na^+ is connected to one edge of the trigonal prism via one μ_3-OH^- and two sao^{2-} ligands bridging in a $\eta^2:\eta^1:\eta^1:\mu_3$-fashion forming the $[Fe_6Na]$ unit. Three Fe_2 edges (Fe1-Fe2, Fe2-Fe3, Fe5-Fe6) of the triangular faces of the trigonal prism are linked by fully deprotonated sao^{2-} ligands bridging in a $\eta^1:\eta^1:\eta^1:\mu_2$-fashion, while the remaining three Fe_2 edges (Fe1-Fe3, Fe4-Fe5, Fe4-Fe6) are linked by a fully deprotonated sao^{2-} ligand bridging in a $\eta^2:\eta^1:\eta^1:\mu_3$-fashion. Each Fe^{III} ion has a distorted octahedral geometry (*cis*, 76.4(3) – 100.6(3)°; *trans*, 166.4(3)-173.9(3)°). In **8** the $[Fe_6]$ units are connected by $[Na_3]$ units whereas in **9** the linkers are $[Na_2]$ units. These are connected via two μ-MeOH molecules which are then connected to each of the two $[Fe_6Na]$ units via one μ_3-OH^- ion and the phenolate oxygen of a $\eta^2:\eta^1:\eta^1:\mu_3$ sao^{2-} ligand (Fig. 5). Terminal MeOH molecules complete the coordination of the Na^+ ions in the $[Na_2]$ unit forming a discrete molecular complex in contrast to the coordination polymer found in **9**. The Na^+ ions in the $[Fe_6Na]$ unit have a distorted octahedral geometry (*cis*, 68.1(3) – 117.7(11)°; *trans*, 147.66(3)-170.57(3)°), while the Na^+ ions in the $[Na_2]$ unit are square pyramidal with a τ value of 0.119.[24] In the crystal lattice there are significant numbers of intra-molecular hydrogen bonds: two between oximic O-atoms and bridging MeOH molecules (O···O, 2.615(0) Å); two between phenolate O-atoms and terminal MeOH molecules (O···O, 2.814(11) Å); four between μ_3-OH^- ions and bridging OMe^- ions (O···O, 2.693(7), 2.633(0) Å); and two between μ_3-OH^- ions and μ_3-O^{2-} ions (O···O, 2.526(7) Å). The closest intermolecular Fe···Fe distance is 8.751 (2) Å.

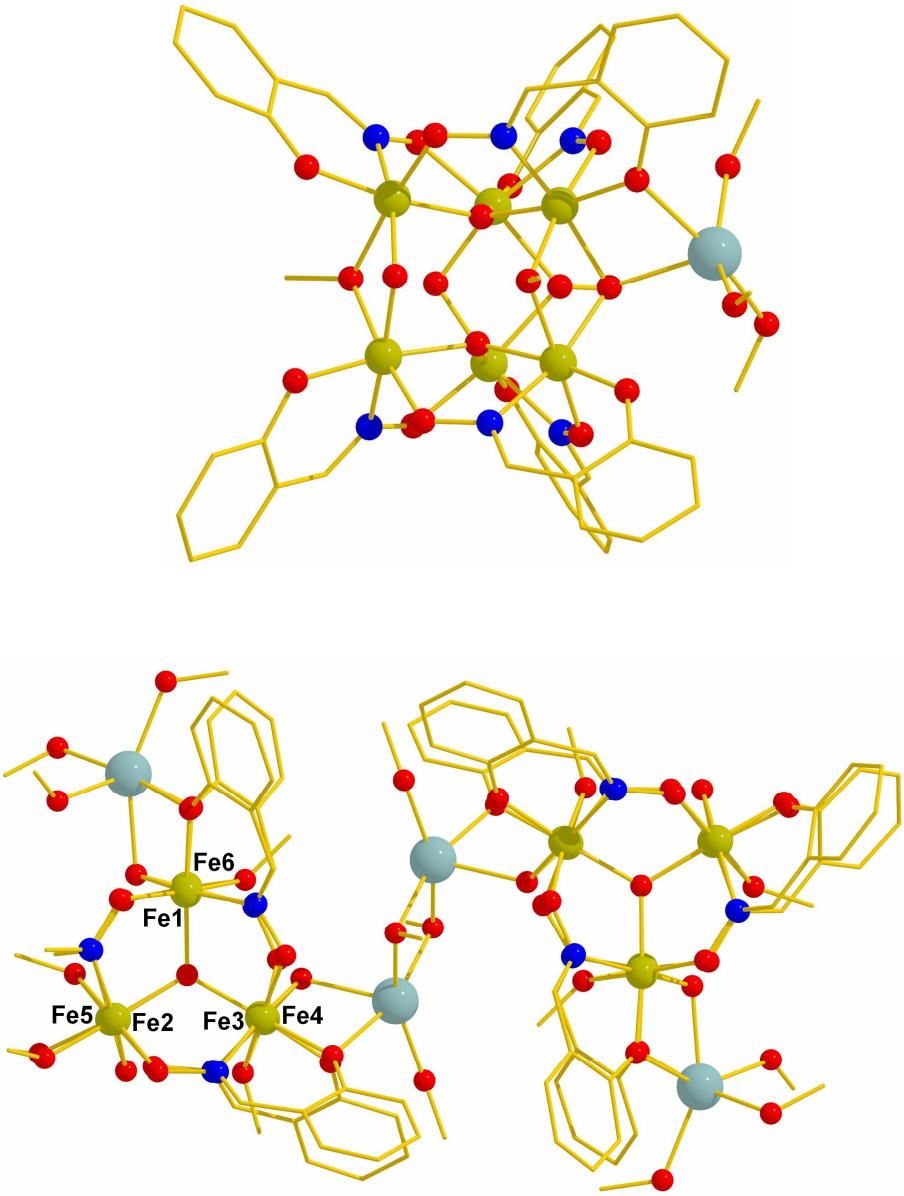

Fig. 6 The molecular structure of **9** viewed perpendicular (top) and parallel to the [Fe_3] planes. The lower picture shows only the [Fe_6Na] unit. Colour code: Fe = green; Na = cyan O = red; N = blue; C = gold.

Complex **10** crystallises in the trigonal space group *R-3* with nine molecules in the unit cell (Fig. 7). The metallic skeleton consists of two edge-sharing tetrahedra (Fe1-Fe2-Fe2'-Fe3 and symmetry equivalent, s.e.) with the Fe1..Fe3 (and s.e) vertices capped by another Fe^{3+} ion (Fe4). The shared edge of the tetrahedra is defined by Fe2-Fe2'. Each [Fe^{III}_4] tetrahedron houses a central μ_4-O^{2-} ion (O123 and symmetry

equivalent), with the bonding along the edges consisting of a combination of single O-atom bridges from μ-OMe^- ions and double N-O atom bridges from Me-sao^{2-} ligands. The latter display three different bonding modes: $\eta^2:\eta^1:\eta^2:\mu_4$, $\eta^1:\eta^1:\eta^2:\mu_3$ and $\eta^1:\eta^1:\eta^1:\mu$. The μ-Me-sao^{2-} ligands bridge Fe2'-Fe3 (and s.e.) through the NO oximic group; the μ_3-Me-sao^{2-} ligands bridge Fe1-Fe4 and Fe3-Fe4 through the two atom N-O bridge and Fe1-Fe3 through the μ-oximic O-atom; and the μ_4-Me-sao^{2-} ligand – seen here for the first time – bridges Fe1, Fe4 and Fe4 through the NO double atom bridge and Fe1 and Fe2 through the phenolic O-atom. This tetranucleating motif for the salicylaldoxime may provide an explanation for how such ligands attach to lightly corroded iron surfaces when they are used as anti-corrosives.[14]

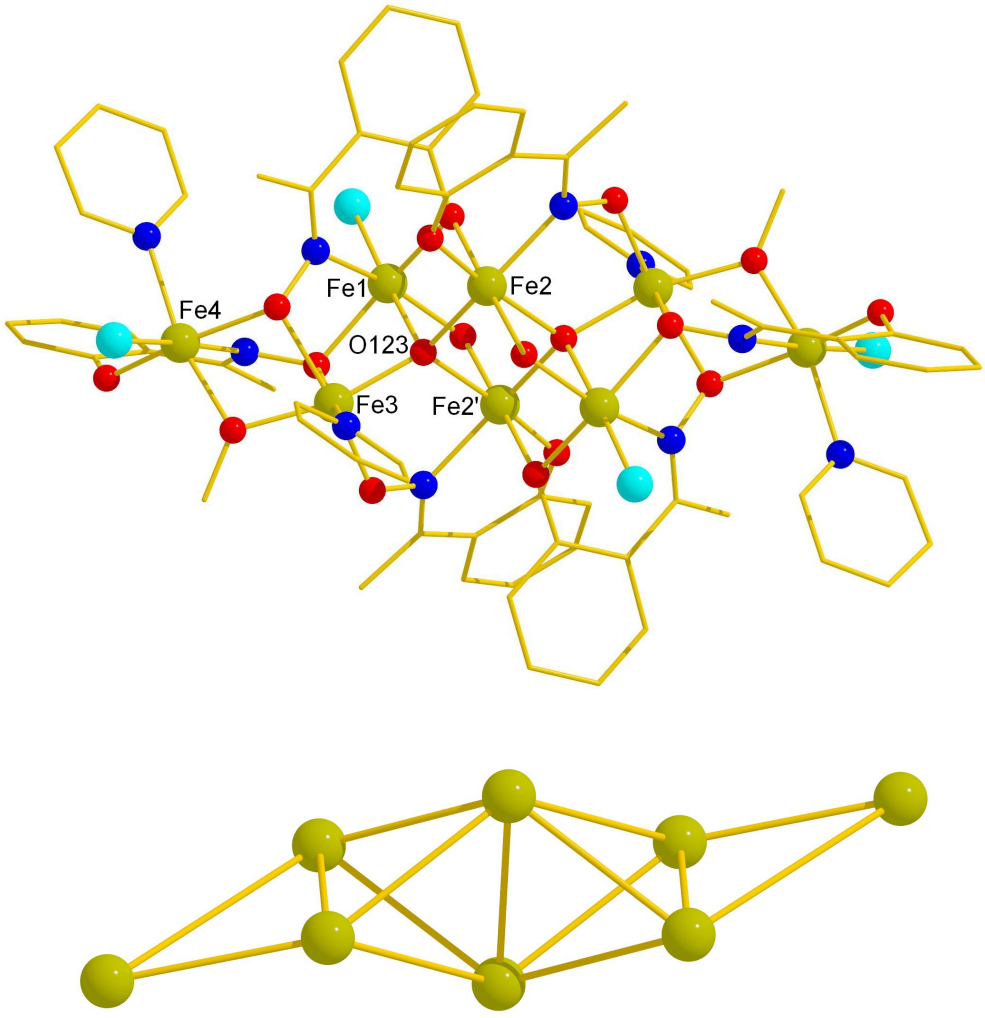

Fig. 7 The molecular structure of **10** (top) and its metallic core (bottom). Colour code: Fe = olive green; O = red; N = dark blue; C = gold; Br = light blue.

There are two symmetry inequivalent OMe^- ions; one bridges the edge-capping peripheral Fe^{3+} ion (Fe4) to the central tetrahedron (Fe3), and the other bridges across one edge of the central tetrahedron (Fe1-Fe2 and s.e). Each Fe^{3+} ion is in a distorted octahedral geometry (*cis*, 74.3(1)-107.1(1)°; *trans*, 156.4(1)-177.12(7)°) with FeO_5N (Fe2, Fe3), FeO_5Br (Fe1) and FeO_3N_2Br (Fe4) coordination spheres. The remaining coordination sites on Fe1, Fe3 and Fe4 are filled with a combination of terminally bonded Br^- ions and/or pyridine molecules.

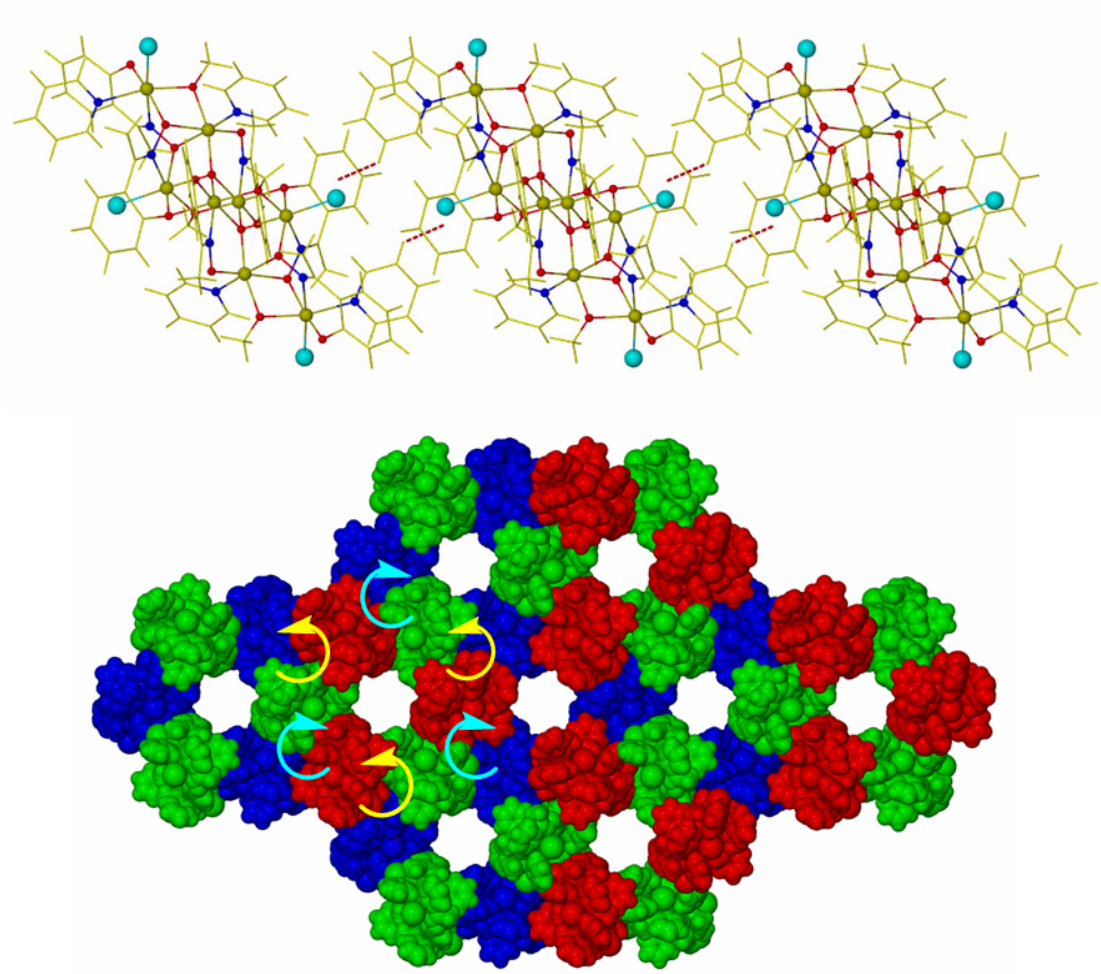

Fig. 8 The 1D chains of **10** along the c-axis formed through C-H…π interactions (top). Packing diagram of the chains of **10** (in red, blue and green) around the left handed (yellow arrow) and right handed (cyan) three-fold screw axes, emphasising the hexagonal cavities (bottom).

In the crystal, the molecules interact through two complementary C-H···π interactions [C5E-H5E···π (C1A, C2A, C3A, C4A, C5A, C6A), C···centroid 3.543 Å, C-H···centroid 124°] to form one dimensional (1D) chains running along the *c*-axis (Fig. 8). Despite the absence of any other inter-molecular hydrogen bonds or π···π interactions [the closest inter-molecular contacts being between the phenyl ring of the μ_4-Me-sao^{2-} ligand and a neighbouring pyridine molecule (C··C, 3.321(7) Å) and between methyl and phenyl groups on opposing μ_3-Me-sao^{2-} ligands (C···C, 3.362(5) Å)], when viewed down the *c*-axis the chains of **10** pack in groups of three around the three fold screw axes (either left or right handed) imposed by the rhombohedral lattice to create large hexagonal cavities approximately 11 Å in diameter (Fig. 8).

Complex **11** crystallises in the monoclinic space group $P2_1/c$ with two molecules in the unit cell (Fig. 9). The molecule differs only slightly from **10**. Besides the small changes in bond lengths and angles, the obvious differences are the replacement of the terminal bromide ions with terminally bonded azide ligands and the partial replacement of a μ-OMe^- bridge with an end-on μ-N_3^- bridge (15% on Fe1-Fe2). This is an interesting observation since the introduction of end-on bridging azides to Fe^{3+} cluster chemistry is likely to produce molecules exhibiting ferromagnetic nearest neighbour exchange.[22, 23] All Fe^{3+} ions have distorted octahedral geometries with *cis* angles in the range 74.09(9)-107.78(9)° and *trans* angles in the range 156.75(9)-179.4(1)°. There are no inter-molecular hydrogen bonds in the extended lattice with the closest contacts being between the phenyl ring of the μ_4-Me-sao^{2-} ligand and a neighbouring pyridine molecule (C···C 3.370(5) Å).

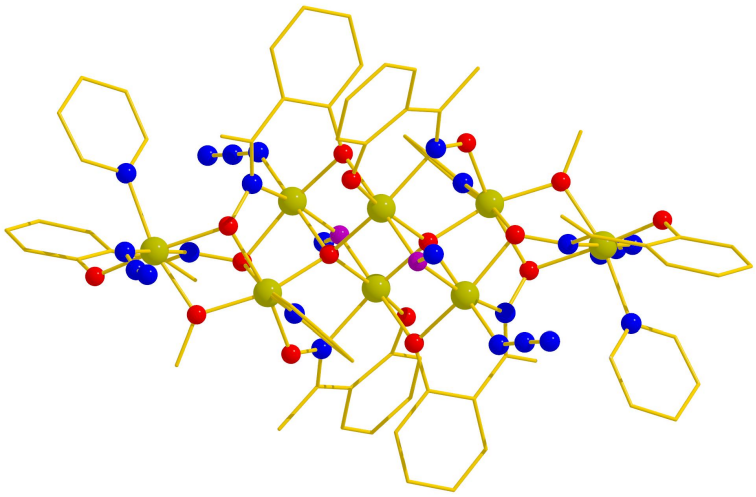

Fig. 9 The molecular structure of **11**. Colour code: Fe = olive green; O = red; N = dark blue; C = gold; partially occupied OMe^-/N_3^- site depicted at purple atom.

Complex **12** (Figure 10) crystallises in the triclinic space group *P*-1 with three molecules in the asymmetric unit and two asymmetric units in the unit cell. The metallic core consists of two edge-sharing (Fe3-Fe4) tetrahedra (Fe1, Fe3, Fe4, Fe5 and Fe2, Fe3, Fe4, Fe6), each housing a central μ_4-O^{2-} ion (O134, O234). The two tetrahedral subunits are joined together by the two η^1:η^1:η^2:μ_3-Me-sao^{2-} ligands bridging Fe1-Fe2 through their oximic NO moeities. The μ-oximic O-atom of one then bridges Fe1-Fe4 while the other bridges Fe2-Fe3. The four μ-O_2CPh-4-NO_2 and four μ-OMe^- ligands bridge the the remaining vertices, the carboxylates bridging Fe2-Fe3, Fe3-Fe5, Fe4-Fe5 and Fe4-Fe6 in their familiar syn, syn, μ-mode and the μ-OMe^- bridging Fe1-Fe5, Fe2-Fe3, Fe3-Fe5 and Fe4-Fe6. The two remaining coordination sites on Fe5 and Fe6 are both occupied with one pyridine molecule and one halide ligand. Each Fe^{3+} ion is a distorted octahedral geometry (*cis*, 77.9(1)-103.9(1)°; *trans*, 157.6(1)-177.7(1)°) with FeO_6 (Fe3, Fe4), FeO_5N (Fe1, Fe2) and FeO_4NCl (Fe5, Fe6) coordination spheres. In the crystal there are a number of inter-molecular interactions propagated through neighbouring 4-NO_2 groups of the carboxylates (O··O, 3.011(4)-3.184(4) Å) lattice, as well as between the chloride ions and neighbouring pyridine molecules (Cl···C, 3.400(6) Å).

Complex **13** crystallises in monoclinic *P21/c* space group with four molecules in the unit cell. **13** differs from **12** only in the identity of the phenolic oxime, Et-sao^{2-}

replacing Me-sao^{2-} and the intra-molecular bond lengths and angles are very similar in both compounds. In the crystal lattice there are inter-molecular hydrogen bonds between the 4-NO_2 group of carboxylate ligands and MeOH solvent molecules (O··C, 3.00(1) Å), with the shortest contact between neighbouring cluster molecules (3.40(1) Å) being between C-atoms on the phenyl rings of adjacent carboxylate and Me-sao^{2-} ligands.

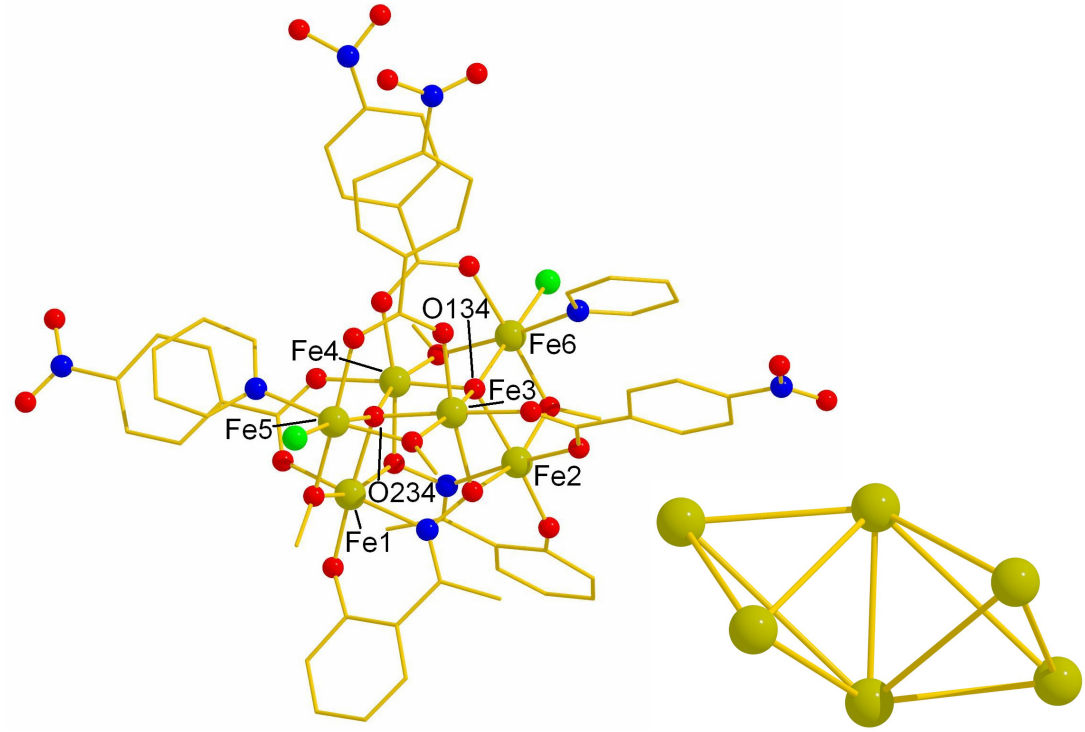

Fig. 10 The molecular structure of **13** (left) and its metallic core (right). Colour code: Fe = olive green; O = red; N = blue; C = gold; Cl = bright green.

Complex **15** (Figure 11) crystallises in the orthorhombic space group *Pbca* with four molecules in the unit cell. Its structure is analogous to that of **14** (but containing Et-sao^{2-} rather than Me-sao^{2-}), which we have reported in a previous paper.[16] **15** is another example of an $[Fe^{III}_6]$ cluster whose metallic core describes two edge sharing tetrahedra. The common edge is Fe1-Fe1' with an inversion centre at its midpoint. The tetrahedra are built upon two central μ_4-O^{2-} ions (O123 and s.e.) and connected via four μ-OMe^- ions (O1A, O14 and s.e.) creating a $[Fe_6O_2(OMe)_4]^{10+}$ core similar to that observed in **12** and **13**. The η^1:η^1:η^1:μ_3-SO_4^{2-} ligands cap the Fe1-Fe2-Fe3

(and s.e.) triangular face of a tetrahedron, whilst the four $\eta^1:\eta^1:\eta^1$:μ-Me-sao^{2-} ligands bridge the Fe1-Fe2 and Fe1-Fe3 (and s.e.) edges.

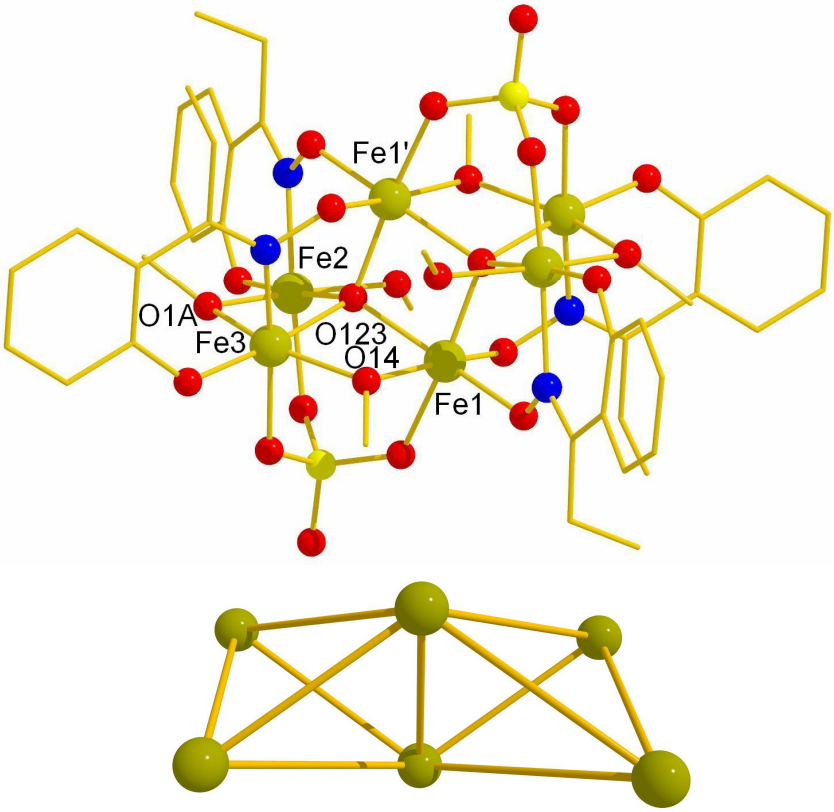

Fig. 11 The molecular structure of **15** (top) and its metallic core (bottom). Colour code: Fe = olive green; O = red; N = blue; C = gold; S = yellow.

A scheme depicting the observed bridging modes of the R-sao^{2-} ligands is given in Figure 12. The remaining coordination sites on Fe1 and Fe1' are filled by terminal MeOH molecules. The Fe^{3+} ions have FeO_6 (Fe1) or FeO_5N coordination spheres and lie in distorted octahedral geometries with *cis* angles in the range 76.9(2)-108.1(2)° and *trans* angles in the range 152.6(2)-175.4(2)°. An examination of the extended lattice reveals short contacts between the NEt_4^+ cation and the SO_4^{2-} (N···O, 2.82(1) Å), with the closest distances between neighbouring clusters being between the phenyl ring of the Et-sao^{2-} ligand and a SO_4^{2-} O-atom (C···O, 3.412(8) Å). There are also intra-molecular H-bonds present - between a terminally bonded MeOH molecule and an oximic O-atom (O···O, 2.737(6) Å).

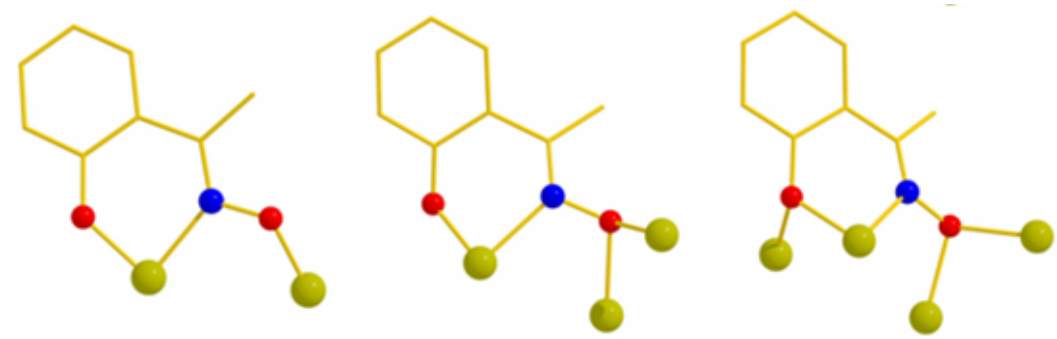

Fig. 12 The coordination modes of the phenolic oximes in complexes **1**- **15**. Colour code: Fe = olive green; O = red; N = blue; C = gold.

Table 1a. Crystallographic details for complexes **1**-**5**.

	1·2MeOH	**2**·Et_2O	**3**·1.5MeOH	**4**	**5**·2MeCN
M, $gmol^{-1}$	1009.29	1108.25	1508.71	1835.66	2235.32
crystal system	Monoclinic	Monoclinic	Monoclinic	Triclinic	Monoclinic
space group	*P* $2_1/c$	*P* $2_1/c$	*P* $2_1/c$	*P* - *1*	*P* $2_1/c$
a, Å	14.2027(3)	14.6095(5)	26.0878(16)	12.8061(8)	14.6892(6)
b, Å	18.0542(4)	18.2293(6)	20.7755(12)	13.5584(9)	19.6643(9)
c , Å	18.0473(4)	18.2766(6)	27.5991(17)	14.0247(9)	19.2762(9)
α, deg	90	90	90	71.209(4)	90
β, deg	98.0570(10)	98.945(2)	115.9810(10)	78.955(4)	104.153(2)
γ, deg	90	90	90	78.812(4)	90
V , $Å^3$	4581.98(17)	4808.2(3)	13446.6(14)	2239.6(3)	5399.0(4)
T , K	150	150	150	150	150
Z	4	4	8	1	2
$\rho_{, calc}$ [$g\ cm^{-3}$]	1.463	1.531	1.490	1.322	1.37
crystal shape and colour	Black rod	Black block	Black plate	Black block	Black block
crystal size [mm]	0.48 x 0.15 x 0.15	0.66 x 0.37 x 0.32	0.44 x 0.13 x 0.07	0.24 x 0.11 x 0.10	0.20 x 0.15 x 0.12
μ, [mm^{-1}]	1.110	2.608	0.923	1.015	0.859
unique data	42560	41924	72924	7881	11117
unique data, (I > 2σ(F))	7742	7249	14464	4615	6311
R_{int}	0.0518	0.0412	0.0870	0.065	0.096
R1[a], wR2[b]	0.0636, 0.1527	0.0421, 0.1073	0.0803, 0.1741	0.0617, 0.1741	0.0536, 0.1660
goodness of fit	1.142	1.030	1.118	0.9039	0.6354

[a] $R1)\ \sum(|Fo| - |Fc|)/\sum(|Fo|)$ for observed reflections. [b] $wR_2)\ \{\sum[w(Fo^2 - Fc^2)_2]/\sum[w(Fo^2)_2]\}^{1/2}$ for all data.

Table 1b. Crystallographic details for complexes **5**-**10**.

	6·4MeCN	**7**	**8**	**9**	**10**·2Et_2O·MeOH
M, $gmol^{-1}$	2250.90	2342.26	1753.41	3262.67	2314.13
crystal system	Triclinic	Monoclinic	Hexagonal	Monoclinic	Hexagonal
space group	*P - 1*	*P 2_1/c*	*P63/m*	*P2_1/c*	*R-3*
a, Å	12.272(5)	13.8956(6)	12.40610(10)	23.1511(7)	42.1099(11)
b, Å	14.458(4)	18.6592(8)	12.40610(10)	13.5740(4)	42.1099(11)
c , Å	16.754(7)	21.4730(9)	28.8478(6)	23.7570(8)	13.8971(4)
α, deg	69.97(8)	90	90	90	90
β, deg	71.74(8)	96.520(2)	90	95.223	90
γ, deg	69.68(6)	90	120	90	120
V , $Å^3$	2554.5(16)	5531.5(4)	3845.16(9)	7434.7(4)	21341.4(10)
T , K	173(2)	150	150	150	150
Z	1	2	2	2	9
$\rho_{, calc}$ [g cm^{-3}]	1.436	1.406	1.51	1.45	1.621
crystal shape and colour	Red rod	Black block	Red block	Dark red block	Black plate
crystal size [mm]	0.50 x 0.20 x 0.50	0.41 x 0.17 x 0.16	0.38 x 0.28 x 0.15	0.21 x 0.20 x 0.15	0.31 x 0.19 x 0.07
μ, [mm^{-1}]	7.366	0.844	1.199	1.227	2.943
unique data	34298	44591	3379	15221	12493
unique data, (I > 2σ(F))	8714	8893	2110	6186	7412
R_{int}	0.1478	0.065	0.066	0.157	0.0560
R1[a], wR2[b]	0.1084, 0.2984	0.0935, 0.1936	0.0297, 0.0322	0.0753, 0.2685	0.0466, 0.1181
goodness of fit	1.056	1.1351	0.9647	1.4701	0.929

[a] $R1$) $\sum(|Fo| - |Fc|)/\sum(|Fo|)$ for observed reflections. [b] wR_2) $\{\sum[w(Fo^2 - Fc^2)_2]/\sum[w(Fo^2)_2]\}^{1/2}$ for all data.

Table 1c. Crystallographic details for complexes **11**-**13**, **15**.

	11	**12**	**13**·2Et_2O·MeOH	**15**
M, $gmol^{-1}$	1985.63	1760.34	1891.41	1604.52
crystal system	Monoclinic	Triclinic	Monoclinic	Orthorhombic
space group	*P 2$_1$/c*	*P -1*	*P 21/c*	*Pbca*
a, Å	11.9923(4)	16.1705(4)	13.5512(19)	20.4582(4)
b, Å	28.0040(10)	27.5304(7)	29.198(4)	14.4149(3)
c , Å	13.3217(5)	29.7123(8)	21.050(3)	22.6752(4)
α, deg	90	114.5420(10)	90	90
β, deg	114.382(2)	90.8730(10)	101.368(6)	90
γ, deg	90	93.4590(10)	90	90
V , $Å^3$	4074.8(3)	11998.6(5)	8165(2)	6687.0(2)
T , K	150	100	100	150
Z	2	6	4	4
$\rho_{, calc}$ [g cm^{-3}]	1.618	1.462	1.539	1.594
crystal shape and colour	Black plate	Black block	Black plate	Black block
crystal size [mm]	0.43 x 0.28 x 0.12	0.44 x 0.44 x 0.26	0.28 x 0.25 x 0.08	0.26 x 0.24 x 0.15
μ, [mm^{-1}]	1.463	1.205	1.187	1.410
unique data	8336	48626	15647	5902
unique data, (I > 2σ(F))	6650	31507	9754	5602
R_{int}	0.0536	0.0531	0.0830	0.0689
R1[a], wR2[b]	0.0424, 0.1012	0.0508, 0.1284	0.0701, 0.2073	0.0826, 0.1547
goodness of fit	1.034	1.002	1.111	1.362

[a] $R1) \sum(|Fo| - |Fc|)/\sum(|Fo|)$ for observed reflections. [b] $wR_2) \{\sum[w(Fo^2 - Fc^2)_2]/\sum[w(Fo^2)_2]\}^{1/2}$ for all data.

2.2.3 Discussion

Following this work there are now a number of Fe^{3+}/R-saoH_2 clusters in the literature (Table 2).[7-16, 19, 32] They range in size ($\leq [Fe_{12}]$) and structure, but there are undoubtedly some pervading themes. The body of published work in this area (Table 2) clearly shows that, akin to Mn^{3+}/R-saoH_2 chemistry, the $[Fe_3(\mu_3\text{-}O)]^{7+}$ triangle is the most frequently encountered building block.[19] The related tetrahedral subunit $[Fe_4(\mu_4\text{-}O)]^{10+}$ is the next most common, and this has no counterpart in Mn^{3+} chemistry. The variance in size of the $[Fe_x]$ cluster can be attributed to a number of factors, including the presence or absence of co-ligand (here carboxylates and sulfates) and the steric bulk of the ketoxime group. This is another area in which we see a difference in comparison with the Mn^{3+} chemistry, where all of the above have little or no effect upon the products of the reaction.[5, 6, 33, 34] The addition of (relatively large) bridging co-ligands tends to favour smaller nuclearity clusters (they edge- and face-cap preventing further growth) and encourages the μ-bridging mode of the phenolic oxime. In the absence of such co-ligands higher order bridging modes of R-sao^{2-} are seen (and higher nuclearity clusters as a consequence) and in complexes **10** and **11** the μ_4-bridging mode is seen for the very first time. The bridging modes depicted in Figure 12 thus offer some insight into possible ligand bonding modes on lightly corroded iron surfaces when salicylaldoximes are used as anti-corrosives.[14]

Variations in the bulk of the ketoxime group can also change the topology of the cluster greatly in Fe^{3+} chemistry,[19] whereas in Mn^{3+} chemistry the $[M_3O(R\text{-}sao)_3]^+$ unit is almost always retained and the only differences observed appear to be in the twisting of the Mn-N-O-Mn torsion angles.[33] For example, both complex **10** and **2** are made by reacting $FeBr_3$ with the appropriate R-saoH_2 pro-ligand in a MeOH/pyridine solvent mix. The bulky Ph-sao^{2-} ligand restricts the size of the cluster to an $[Fe_3]$ triangle, but the Me-sao^{2-} ligand allows the growth of an octametallic cluster, $[Fe_8]$.

When employing carboxylates in Fe^{3+}/R-saoH_2 chemistry one might expect the structures to resemble the basic Fe^{3+} carboxylates of general formula $[Fe_3O(O_2CR)_6L_3]^+$ (L = solvent) in which $\mu_{2/3}$–bridging R-sao^{2-} ligands simply

replace the μ–bridging carboxylates. Indeed this is true in $[Fe_6]$ clusters where the $[Fe_3(\mu_3\text{-}O)]^{7+}$ building block predominates,[12, 13, 19] and the μ_3–bridging oxime promotes oligomerisation of the basic triangles. Complexes **12** and **13** differ; the major change in reaction conditions being the introduction of pyridine. This results in the formation of a cluster adopting a metallic skeleton comprising two edge-sharing tetrahedra. Pyridine is present in excess and thus acts as base, ligand and co-solvent – a strategy that has been shown previously to aid the growth of very large mineral-like Fe^{3+} clusters.[35]

Table 2. The structurally characterised Fe/R-sao^{2-} complexes in the CCDC database.

Molecule	Core	Oxime coordination	Reference
$[HNEt_3][Fe_2(OMe)(Ph\text{-}sao)_2(Ph\text{-}saoH)_2]\cdot 5MeOH$	$[Fe_2(OMe)(ON^-)_2]^{3+}$ dimer	2 x μ, 1 x NO^- chelate	**10**
$[Fe_2(sao)_3(tmtacn)]\cdot MeOH$	$[Fe_2(ON^-)_3]^{3+}$ dimer	3 x μ	**15**
$[Fe_2(3\text{-}5\text{-}di\text{-}^t but\text{-}sao)_3(tmtacn)]\cdot 3.5\ CHCl_3$	$[Fe_2(ON^-)_3]^{3+}$ dimer	3 x μ	**15**
$[Fe_3O(O_2CPh)_5(sao)(MeOH)_2]\cdot 1.25MeOH\cdot 1.05H_2O$	$[Fe_3(\mu_3\text{-}O)]^{7+}$ triangle	1 x μ	**13**
$[Fe_3O(O_2CPh)_5(sao)(EtOH)(H_2O)]\cdot EtOH$	$[Fe_3(\mu_3\text{-}O)]^{7+}$ triangle	1 x μ	**13**
$[Fe_3O\ (O_2CPh)_5(Et\text{-}sao)(MeOH)_2]\cdot 3MeOH$	$[Fe_3(\mu_3\text{-}O)]^{7+}$ triangle	1 x μ	**10**
$[Fe_3O(OMe)(Ph\text{-}sao)_2Cl_2(py)_3]\cdot 2MeOH$	$[Fe_3(\mu_3\text{-}O)]^{7+}$ triangle	1 x μ	**This work[19]**
$[Fe_3O(OMe)(Ph\text{-}sao)_2Br_2(py)_3]\cdot Et_2O$	$[Fe_3(\mu_3\text{-}O)]^{7+}$ triangle	1 x μ	**This work[19]**
$[HNEt_3][Fe_3O(salmpH_3)(sao)_2(saoH)].2H_2O$	$[Fe_3(\mu_3\text{-}O)]^{7+}$ triangle	1 x μ, 1 x NO^- chelate	**7**
$[Fe_4(Me\text{-}sao)_4(Me\text{-}saoH)_4]\cdot MeOH$	Distorted $[Fe_4(NO)_4]^{8+}$ cube	4 x μ_3, 4 x NO^- chelate	**10**
$[Fe_4(sao)_4(saoH)_4]\cdot saoH_2\cdot C_8H_{10}$	Distorted $[Fe_4(NO)_4]^{8+}$ cube	4 x μ_3, 4 x NO^- chelate	**14**
$[Fe_4(Ph\text{-}sao)_4F_4(py)_4]\cdot 1.5MeOH$	$[Fe_4(NO)_4F_4]$ square	4 x μ	**This work[19]**
$[Fe_4O_2(O_2CCH_3)_3(sao)_2(tmtacn)_2][PF_6]$	$[Fe_4(\mu_3\text{-}O)_2]^{8+}$ butterfly	2 x μ	**9**
$[Fe_4O_2(O_2CC(OH)Ph_2)_3(sao)_2(tmtacn)_2][ClO_4]$	$[Fe_4(\mu_3\text{-}O)_2]^{8+}$ butterfly	2 x μ	**8**
$[Fe_6O_2(O_2CPh)_{10}(sao)_2(MeCONH_2)2]\cdot 6MeCN$	2 x $[Fe_3(\mu_3\text{-}O)]^{7+}$ triangles	2 x μ_3	**12**
$[Fe_6O_2(O_2CPh)_{10}(sao)_2(H_2O)_2]\cdot 2MeCN\cdot 3H_2O$	2 x $[Fe_3(\mu_3\text{-}O)]^{7+}$ triangles	2 x μ_3	**12**
$[Fe_6O_2(OH)_2(O_2CPh)_6(Et\text{-}sao)_2(Et\text{-}saoH)_2]$	2 x $[Fe_3(\mu_3\text{-}O)]^{7+}$ triangles	2 x μ, 2 x μ_3	**This work[19]**
$[HNEt_3]_2[Fe_6O_2(OH)_2(O_2CPh(Me)_2)_6(Et\text{-}sao)_4]\cdot 2MeCN$	2 x $[Fe_3(\mu_3\text{-}O)]^{7+}$ triangles	2 x μ, 2 x μ_3	**This work[19]**
$[Fe_6Na_3O(OH)_4(OMe)_3(Me\text{-}sao)_6(H_2O)_3(MeOH)_6]\cdot MeOH$	2 x $[Fe_3(\mu_3\text{-}O)]^{7+}$ triangles	6 x μ	**This work[19]**
$[Fe_6O_2(O_2CPh)_{10}(3\text{-}^t but\text{-}5\text{-}NO_2\text{-}sao)_2(H_2O)_2].2MeCN$	2 x $[Fe_3(\mu_3\text{-}O)]^{7+}$ triangles	2 x μ	**This work[19]**
$[Fe_6O_2(O_2CCH_2Ph)_{10}(3\text{-}^t but\text{-}sao)_2(H_2O)_2].5MeCN$	2 x $[Fe_3(\mu_3\text{-}O)]^{7+}$ triangles	2 x μ	**This work[19]**
$[HNEt_3]_2[Fe_6O_2(OMe)_4(Me\text{-}sao)_4(SO_4)_2(MeOH)_2]$	2 x edge sharing $[Fe_4(\mu_4\text{-}O)]^{10+}$ tetrahedra	4 x μ	**10 / This work**
$[HNEt_3]_2[Fe_6O_2(OMe)_4(Et\text{-}sao)_4(SO_4)_2(MeOH)_2]$	2 x edge sharing $[Fe_4(\mu_4\text{-}O)]^{10+}$ tetrahedra	4 x μ	**This work[32]**
$[Fe_6O_2(O_2CPhNO_2)_4(OMe)_4(Me\text{-}sao)_2Cl_2(py)_2]$	2 x edge sharing $[Fe_4(\mu_4\text{-}O)]^{10+}$ tetrahedra	2 x μ_3	**This work[32]**

$[Fe_6O_2(OMe)_4(O_2CPhNO_2)_4(Et\text{-}sao)_2Cl_2(py)_2]\cdot 2Et_2O\cdot MeOH$	2 x edge sharing $[Fe_4(\mu_4\text{-}O)]^{10+}$ tetrahedra	2 x μ_3	**This work[32]**
$[Fe_8O_3(O_2CMe)_3(Me\text{-}sao)_3(tea)(teaH)_3]$	3 x common-edge sharing $[Fe_4(\mu_4\text{-}O)]^{10+}$ tetrahedra	3 x μ	**10**
$[Fe_8O_3(O_2CMe)_3(Et\text{-}sao)_3(tea)(teaH)_3]$	3 x common-edge sharing $[Fe_4(\mu_4\text{-}O)]^{10+}$ tetrahedra	3 x μ	**10**
$[Fe_8O_3(O_2CMe)_3(Ph\text{-}sao)_3(tea)(teaH)_3]$	3 x common-edge sharing $[Fe_4(\mu_4\text{-}O)]^{10+}$ tetrahedra	3 x μ	**10**
$[Fe_8O_4(sao)_8(py)_4]\cdot 4py$	4 x $[Fe_4(\mu_4\text{-}O)]^{10+}$ tetrahedra	4 x μ, 4 x μ_3	**11**
$[Fe_8O_2(OMe)_4(Me\text{-}sao)_6Br_4(py)_4]\cdot 2Et_2O\cdot MeOH$	2 x bicapped $[Fe_4(\mu_4\text{-}O)]^{10+}$ tetrahedra	2 x μ, 2 x μ_3, 2 x μ_4	**This work[32]**
$[Fe_8O_2(OMe)_{3.85}(N_3)_{4.15}(Me\text{-}sao)_6(py)_2]$	2 x bicapped $[Fe_4(\mu_4\text{-}O)]^{10+}$ tetrahedra	2 x μ, 2 x μ_3, 2 x μ_4	**This work[32]**
$[HNEt_3]_2[Fe_{12}Na_4O_2(OH)_8(OMe)_6(sao)_{12}(MeOH)_{10}]$	4 x $[Fe_3(\mu_3\text{-}O)]^{7+}$ triangles	6 x μ, 6 x μ_3	**This work[19]**

Abbreviations: $saoH_2$, Ph-$saoH_2$, see Fig 1. tmtacn, 1,4,7-trimethyl-1,4,7-triazacyclononane; $salmpH_3$, 2(bis(salicylideneamino)methyl)phenolate(−3); $teaH_3$, triethanolamine.

2.2.4 Magnetism

Direct current (dc) magnetic susceptibility studies were performed for microcrystalline samples of **1**, **3-6**, **8-10** and **12** in the 5-300 K range under an applied field of 0.1 T. The magnetic behaviour of complex **14** is analogous to that of complex **15** which we have reported before, so will not be repeated here.[10] For **1** (Fig. 13) the room temperature $\chi_M T$ value of approximately 4.8 cm^3 K mol^{-1} is lower than expected for three non-interacting Fe^{III} ions (~13 cm^3 K mol^{-1}). Upon cooling, the value of $\chi_M T$ initially decreases to approximately ~4.3 cm^3 K mol^{-1} at 125 K before increasing to a value of ~4.5 cm^3 K mol^{-1} at 25 K. Below this temperature there is a rapid decrease to approximately 4.1 cm^3 K mol^{-1} at 5 K - presumably due to inter-molecular interactions and/or Zeeman effects. This behaviour is indicative of antiferromagnetic exchange between the metal centres and an S = 5/2 ground state. The data for **1** was simulated employing the spin-Hamiltonian ($J_1 = J_2 \neq J_3$) $\hat{H} = -2J_1(\hat{S}_1 \cdot \hat{S}_2 + \hat{S}_1 \cdot \hat{S}_3) - 2J_2(\hat{S}_2 \cdot \hat{S}_3)$ affording the parameters S = 5/2, g = 2.02, J_1 = -40.0

cm^{-1}, J_2 = -5.5 cm^{-1}. Magnetic measurements were not made on **2** as it is isostructural with **1** differing only in the nature of the coordinating halides.

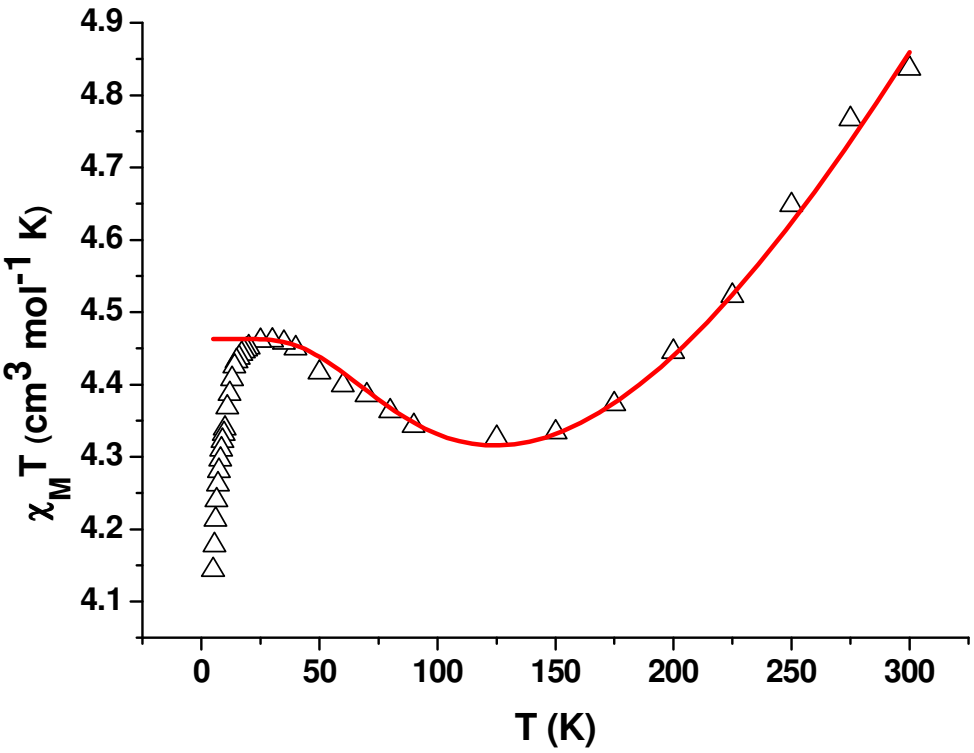

Fig. 13 Plot of $\chi_M T$ *vs* T for complex **1**. The solid red line represents the simulation of the experimental data - see text for details.

For complex **3** (Fig. 14) the room temperature $\chi_M T$ value of approximately 15 cm^3 K mol^{-1} is lower than expected for four non-interacting Fe^{III} ions (~17.5 cm^3 K mol^{-1}). Upon cooling, the value of $\chi_M T$ decreases almost linearly to approximately ~2 cm^3 K mol^{-1} at 5 K, indicative of relatively strong antiferromagnetic exchange with a diamagnetic ground state. Despite appearing to be a very simple molecule, each of the Fe-Fe interactions is unique and there are in fact two different [Fe_4] clusters per unit cell, requiring a total of eight separate J-values. Attempts to fit the data employing simple 1, 2 and 3J models all failed to produce a satisfactory result.

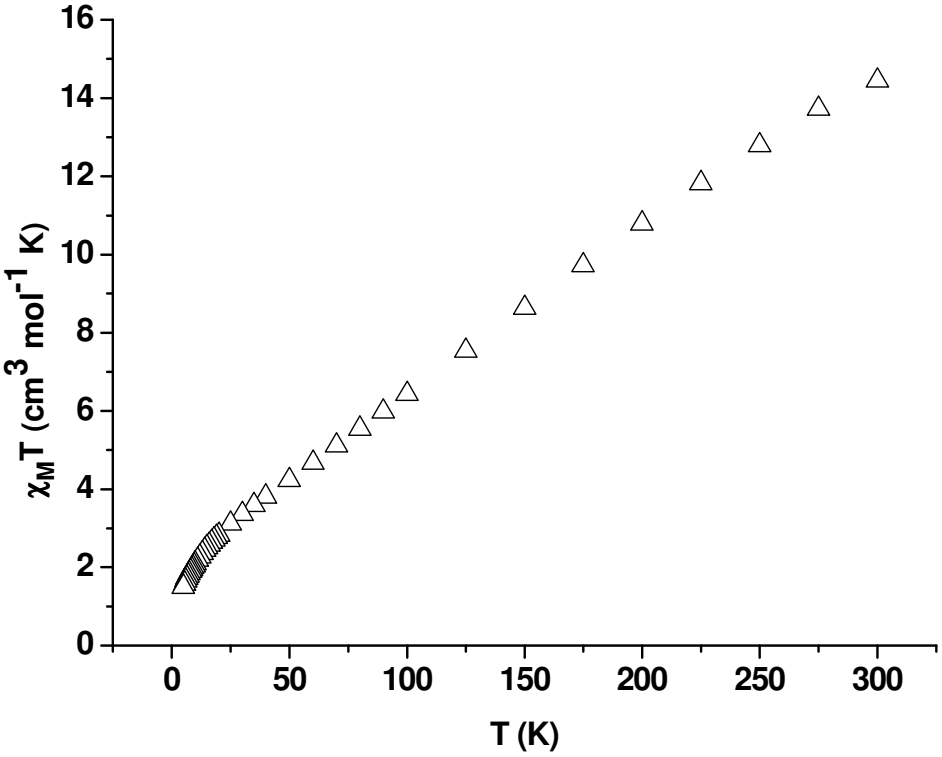

Fig. 14 Plot of χ_MT vs T for complex **3**.

For complexes **4-6**, **8**-**9** (Fig. 15) the room temperature $\chi_M T$ values of approximately 6.4, 6.1, 5.2, 11.0 and 10.2 cm^3 K mol^{-1} respectively are lower than that expected for six non-interacting Fe^{III} ions (26.25 cm^3 K mol^{-1}). On cooling, the values of $\chi_M T$ decrease to approximately 0.3, 1.1, 0.6, 0.26 and 0.22 cm^3 K mol^{-1} at 5 K respectively. This behaviour is consistent with antiferromagnetic exchange between the metal centres and $S = 0$ ground states.

The complexity of structures of **4-6**, **8** and **9** precludes the fitting of the susceptibility data by standard procedures.

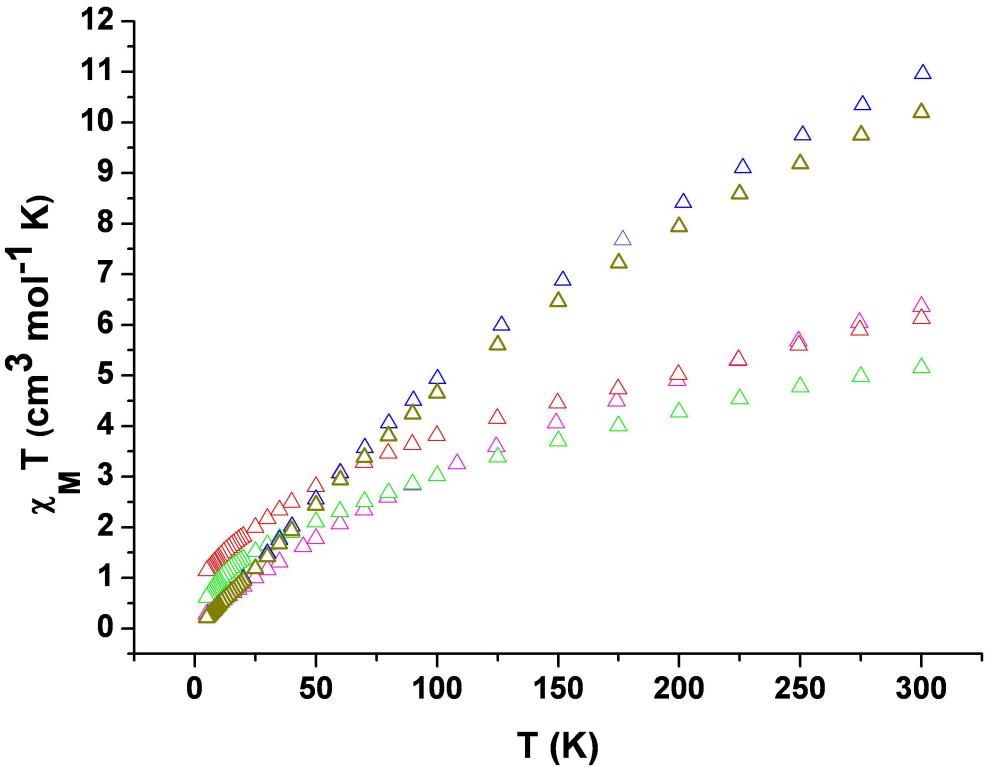

Fig. 15 Plot of $\chi_M T$ vs T for complexes **4** (magenta); **5** (red); **6** (green); **8** (blue); and **9** (olive).

For **10** (Fig. 16) the room temperature $\chi_m T$ value of 12.38 cm^3 K mol^{-1} is significantly below the value of 35 cm^3 K mol^{-1} expected for eight non-interacting high spin (S = 5/2) Fe^{3+} ions, indicative of relatively strong antiferromagnetic exchange interactions. The $\chi_m T$ value decreases steadily with decreasing temperature reaching 0.79 cm^3 K mol^{-1} at 5 K, indicative of an S = 0 ground state. A plot of $1/\chi_m$ vs T affords θ = -115 K. The room temperature $\chi_m T$ value of complex **12** (Fig. 16) is 11.23 cm^3 K mol^{-1}, lower than the expected value for six non-interacting Fe^{3+} ions (26.25 cm^3 K mol^{-1}). The $\chi_m T$ value then decreases constantly with decreasing temperature to a value of 0.25 cm^3 K mol^{-1}. This is again indicative of antiferromagnetic exchange interactions between the Fe^{3+} ions and the stabilisation of a diamagnetic ground state. A Curie-Weiss analysis of the $1/\chi_m$ vs T plot affords θ = -386 K. The complex nature of the structures again precludes fitting of the susceptibility data by standard procedures. Of the thirty two complexes listed in Table 2 only two structural types (and a total of eight molecules) have been reported

to possess non-zero spin ground states - the [Fe_3] triangles and complexes **14** and **15**. Both are the result of spin frustration effects from antiferromagnetic exchange within symmetric metallic cores. This suggests that future attempts to build Fe^{3+}/R-sao^{2-} clusters with non-zero spin ground states should focus on the use of high temperature / high pressure (e.g. solvothermal or microwave) reaction conditions which are likely to produce highly symmetric molecules.[36]

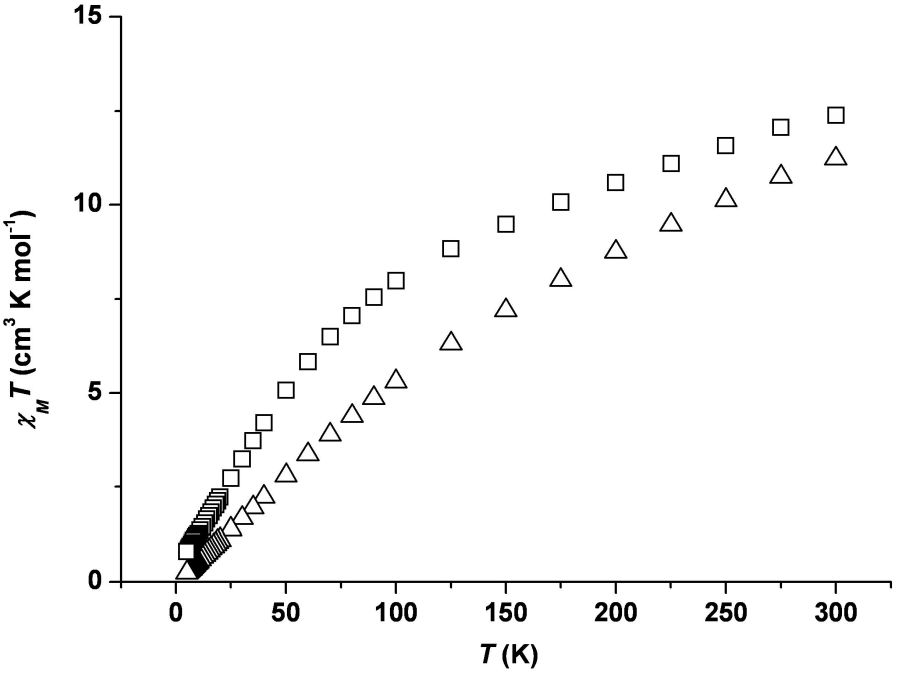

Fig 16. Plot of $\chi_M T$ vs T for complexes **10** (squares) and **12** (triangles).

2.4 Conclusions

The fifteen iron(III) cluster compounds assembled using salicylaldoxime derivatives range in nuclearity from three to twelve. The results support the proposition that salicylaldoximates favour the formation of polynuclear complexes with higher oxidation state transition metal ions, whilst the coordination chemistry with M^{2+} ions is dominated by mononuclear complexes.[37] The predominant building block in the new clusters – as also seen in Mn^{3+} chemistry[5, 6, 34, 38]– appears to be the triangular [Fe_3O(R-sao)$_3$]$^+$ species, which can assemble into more elaborate arrays depending on reaction conditions. An interesting observation is that R-saoH$^-$/R-sao^{2-}

ligand system tends to adopt coordination modes similar to carboxylates, and given that the latter have been deployed successfully in making magnetically interesting molecules, it is timely to extend that range of oximate-based Fe(III) clusters. The most unusual molecule is **3** which contains the $[Fe_4F_4]$ molecular square. Whilst Cl^- and Br^- appear to act only as terminal ligands, the F- ions bridge thus making a major impact on molecular structure and topology – affording the square rather than the "expected" (oxo-centered) triangles. F^- bridges have been used with great success in recent Cr(III) chemistry[39, 40] but their use in building Fe(III) clusters is extremely rare,[41] again suggesting potential future routes to novel Fe molecules.

Complexes **10**-**15** all have a different common building block, the tetrahedral $[Fe_4O]^{10+}$ moiety. Each contains a central core of two such edge-sharing tetrahedra, with **10** and **11** having two vertices additionally capped by Fe^{3+} ions, as a result of a unique μ_4-Me-sao^{2-} coordination mode. In contrast to Mn^{3+} complexes, the self-assembly of these Fe^{3+} molecules – and the coordination mode of the phenolic oxime ligand – appears to be highly dependent upon the presence of co-ligands and the steric bulk of the ketoxime group. The magnetic behaviour of all complexes is [perhaps unsurprisingly] dominated by relatively strong antiferromagnetic exchange interactions, as seen for almost all reported Fe^{3+}/R-$saoH_2$ complexes. However, the observation in complex **11** of the partial replacement of a μ–bridging OMe^- ion with an end-on μ–N_3^- ion, and the symmetric cores of complexes **14** and **15**, suggests targeting both azide-based clusters and highly symmetric complexes, since they may pave the way for isolating compounds displaying frustration effects, and/or ferro- or ferrimagnetic exchange interactions.

2.5 References

1. C. J. Milios, A. Vinslava, A. G. Whittaker, S. Parsons, W. Wernsdorfer, G. Christou, S. P. Perlepes and E. K. Brechin, *Inorg. Chem.*, 2006, **45**, 5272.
2. C. J. Milios, I. A. Gass, A. Vinslava, L. Budd, S. Parsons, W. Wernsdorfer, S. P. Perlepes, G. Christou and E. K. Brechin, *Inorg. Chem.*, 2007, **46**, 6215.
3. R. Inglis, S. J. Dalgarno and E. K. Brechin, *Dalton Trans.*, 2010, **39**, 4826.
4. R. Inglis, L. F. Jones, G. Karotsis, A. Collins, S. Parsons, S. P. Perlepes, W. Wernsdorfer and E. K. Brechin, *Chem. Commun.*, 2008, 5924.
5. R. Inglis, L. F. Jones, K. Mason, A. Collins, S. A. Moggach, S. Parsons, S. P. Perlepes, W. Wernsdorfer and E. K. Brechin, *Chem. Eur. J*, 2008, **14**, 9117.
6. L. F. Jones, R. Inglis, M. E. Cochrane, K. Mason, A. Collins, S. Parsons, S. P. Perlepes and E. K. Brechin, *Dalton Trans.*, 2008, **44**, 6205.
7. E. Bill, C. Krebs, M. Winter, M. Gerdan, A. X. Trautwein, U. Flörke, H.-J. Haupt and P. Chaudhuri, *Chem. Eur. J*, 1997, **3**, 193.
8. P. Chaudhuri, E. Rentschler, F. Birkelbach, C. Krebs, E. Bill, T. Weyhermüller and U. Flörke, *Eur. J. Inorg. Chem.*, 2003, **2003**, 541.
9. P. Chaudhuri, M. Winter, P. Fleischhauer, W. Haase, U. Flörke and H.-J. r. Haupt, *Inorg. Chim. Acta*, 1993, **212**, 241.
10. I. A. Gass, C. J. Milios, A. Collins, F. J. White, L. Budd, S. Parsons, M. Murrie, S. P. Perlepes and E. K. Brechin, *Dalton Trans.*, 2008, **15**, 2043.
11. I. A. Gass, C. J. Milios, A. G. Whittaker, F. P. A. Fabiani, S. Parsons, M. Murrie, S. P. Perlepes and E. K. Brechin, *Inorg. Chem.*, 2006, **45**, 5281.
12. C. P. Raptopoulou, A. K. Boudalis, Y. Sanakis, V. Psycharis, J. M. Clemente-Juan, M. Fardis, G. Diamantopoulos and G. Papavassiliou, *Inorg. Chem.*, 2006, **45**, 2317.
13. C. P. Raptopoulou, Y. Sanakis, A. K. Boudalis and V. Psycharis, *Polyhedron*, 2005, **24**, 711.
14. J. M. Thorpe, R. L. Beddoes, D. Collison, C. D. Garner, M. Helliwell, J. M. Holmes and P. A. Tasker, *Angew. Chem. Int. Ed*, 1999, **38**, 1119.
15. C. N. Verani, E. Bothe, D. Burdinski, T. Weyhermüller, U. Flörke and P. Chaudhuri, *Eur. J. Inorg. Chem.*, 2001, **2001**, 2161.
16. P. Chaudhuri, M. Hess, E. Rentschler, T. Weyhermuller and U. Flörke, *New J. Chem.*, 1998, **22**, 553.
17. W. R. Dunstan and T. A. Henry, *J. Chem. Soc., Trans.*, 1899, **75**, 66.
18. I. A. Gass, PhD Thesis, University of Edinburgh, 2008.
19. K. Mason, I. A. Gass, S. Parsons, A. Collins, F. J. White, A. M. Z. Slawin, E. K. Brechin and P. A. Tasker, *Dalton Trans.*, 2010, **39**, 2727.
20. V. Anuradha, P. V. Srinivas, P. Aparna and J. M. Rao, *Tetrahedron Lett.*, 2006, **47**, 4933.
21. R. R. Bak and A. J. Smallridge, *Tetrahedron Lett.*, 2001, **42**, 6767.
22. G. De Munno, T. Poerio, G. Viau, M. Julve and F. Lloret, *Angew. Chem. Int. Ed*, 1997, **36**, 1459.
23. K. R. Reddy, M. V. Rajasekharan and J. P. Tuchagues, *Inorg. Chem.*, 1998, **37**, 5978.
24. A. W. Addison, T. N. Rao, J. Reedijk, J. van Rijn and G. C. Verschoor, *J. Chem. Soc., Dalton. Trans.*, 1984, 1349.
25. I. D. Brown and D. Altermatt, *Acta Cryst.*, 1985, **41**, 244.
26. H. H. Thorp, *Inorg. Chem.*, 1992, **31**, 1585.
27. D. W. Aldous, N. F. Stephens and P. Lightfoot, *Dalton Trans.*, 2007, 2271.
28. R. Basta, B. G. Harvey, A. M. Arif and R. D. Ernst, *J. Am. Chem. Soc.*, 2005, **127**, 11924.

29. A. Böttcher, H. Elias, J. Glerup, M. Neuburger, C. E. Olsen, H. Paulus, J. Springborg and M. Zehnder, *Acta Chem. Scand.*, 1994, **48**, 967.
30. W. S. Sheldrick, *J. Fluorine Chem.*, 1974, **4**, 415.
31. D. A. Straus, M. Kamigaito, A. P. Cole and R. M. Waymouth, *Inorg. Chim. Acta*, 2003, **349**, 65.
32. K. Mason, I. A. Gass, F. J. White, G. S. Papaefstathiou, E. K. Brechin and P. A. Tasker, *Dalton Trans.*, 2011, **40**, 2875.
33. R. Inglis, L. F. Jones, C. J. Milios, S. Datta, A. Collins, S. Parsons, W. Wernsdorfer, S. Hill, S. P. Perlepes, S. Piligkos and E. K. Brechin, *Dalton Trans.*, 2009, **18**, 3403.
34. R. Inglis, C. J. Milios, L. F. Jones, S. Piligkos and E. K. Brechin, *Chem. Commun.*, 2011, *Advanced Article*. And references therein.
35. G. W. Powell, H. N. Lancashire, E. K. Brechin, D. Collison, S. L. Heath, T. Mallah and W. Wernsdorfer, *Angew. Chem. Int. Ed*, 2004, **43**, 5772.
36. R. Shaw, R. H. Laye, L. F. Jones, D. M. Low, C. Talbot-Eeckelaers, Q. Wei, C. J. Milios, S. Teat, M. Helliwell, J. Raftery, M. Evangelisti, M. Affronte, D. Collison, E. K. Brechin and E. J. L. McInnes, *Inorg. Chem.*, 2007, **46**, 4968.
37. A. G. Smith, P. A. Tasker and D. J. White, *Coord. Chem. Rev.*, 2003, **241**, 61.
38. C. C. Stoumpos, R. Inglis, G. Karotsis, L. F. Jones, A. Collins, S. Parsons, C. J. Milios, G. S. Papaefstathiou and E. K. Brechin, *Cryst. Growth Des.*, 2008, **9**, 24.
39. L. P. Engelhardt, C. A. Muryn, R. G. Pritchard, G. A. Timco, F. Tuna and R. E. P. Winpenny, *Angew. Chem. Int. Ed*, 2008, **47**, 924.
40. S. T. Ochsenbein, F. Tuna, M. Rancan, R. S. G. Davies, C. A. Muryn, O. Waldmann, R. Bircher, A. Sieber, G. Carver, H. Mutka, F. Fernandez-Alonso, A. Podlesnyak, L. P. Engelhardt, G. A. Timco, H. U. Güdel and R. E. P. Winpenny, *Chem. Eur. J*, 2008, **14**, 5144.
41. A. Bino, M. Ardon, D. Lee, B. Spingler and S. J. Lippard, *J. Am. Chem. Soc.*, 2002, **124**, 4578.

Chapter 3
Introducing Co-ligands to Fe^{III} clusters built with Salicylaldoximes

3.1 Introduction

In the previous chapter we have explored the effects of systematically altering the reaction conditions within the rather simple Fe^{III}/R-saoH_2 reaction scheme, and have garnered a plethora of cages ranging in nuclearity from two to eight.[1-12] Common to all the metallic skeletons are the triangular $[Fe_3O]^{7+}$ and tetrahedral $[Fe_4O]^{10+}$ building blocks. In the present work we employ co-ligands such as tacn, hmpH and pdmH_2 (Figure 1) in the expectation that introducing molecules that can compete with the phenolic oximes for the metal coordination sites will result in the formation of novel clusters. The co-ligands were chosen because they have been shown previously to promote formation of Fe^{III} clusters.[13-22] For example, the ligand tacn was used in the synthesis of the first recognised Fe^{III} single molecule magnet, $[Fe_8]$,[23, 24] and hmpH and pdmH_2 have both been used extensively in metal cluster synthesis.[13-15, 18, 19, 25-34]

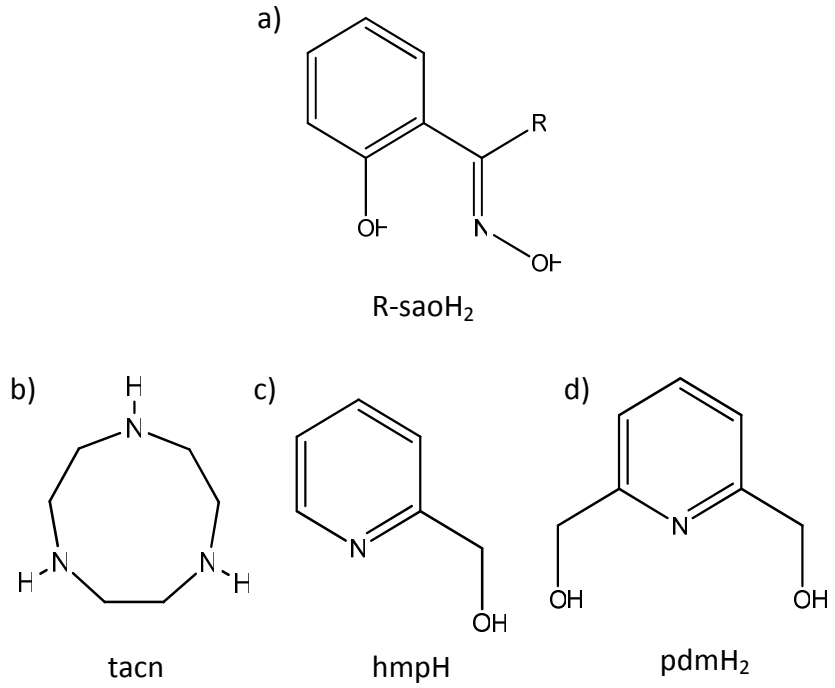

Fig. 1 The ligands (a) salicylaldoxime, R = H, saoH_2; R = Me, Me-saoH_2; R = Et, Et-saoH_2; R= Ph, Ph-saoH_2. (b) 1,4,7-triazacyclononane, tacn. (c) 2-(hydroxymethyl)pyridine, hmpH. (d) 2,6-pyridinedimethanol, pdmH_2.

3.2 Experimental

3.2.1 Syntheses

All manipulations were performed under aerobic conditions using chemicals as received, unless otherwise stated. 2-hydroxyacetophenone oxime (Me-saoH_2) and 2-hydroxypropiophenone oxime (Et-saoH_2) were synthesised *via* the reaction of the appropriate ketone with hydroxylamine and sodium acetate as described in the literature.[35] tacn was prepared as previously described.[36]

[Fe_4O_2(sao)$_4$(tacn)$_2$]·2MeOH·H_2O (**16**·2MeOH·H_2O).

$FeCl_2.4H_2O$ (198 mg, 1 mmol) and saoH_2 (205 mg, 1.5 mmol) were stirred in a 1:1 mixture of MeOH and CH_2Cl_2 (25ml). In a separate flask tacn.3HBr (279 mg, 0.75 mmol) and NEt_3 (6 ml, 54 mmol) were stirred in 5 ml of a 1:1 EtOH/CH_2Cl_2 mix. After 30 minutes the two independent solutions were mixed and stirred for a further 18 hours, after which the solution was filtered and left to evaporate slowly. X-ray quality crystals were present after 2 days in ~40% yield. Elemental analysis: found (calc. %) for $C_{40}H_{50}Fe_4N_{10}O_{10}$: C 45.23 (45.57), H 4.67 (4.78), N 13.21 (13.29).

[Fe_4O_2(Me-sao)$_4$(tacn)$_2$]·2MeCN (**17**·2MeCN).

Procedure as for **16**, replacing saoH_2 with Me-saoH_2 (226 mg, 1.5 mmol) and MeOH with MeCN. Yield ~40%. Elemental analysis found (calc %) for $C_{44}H_{58}Fe_4N_{10}O_{10}$: C 47.46 (47.59), H 5.03 (5.26), N 12.25 (12.61).

[Fe_4O_2(Et-sao)$_4$(tacn)$_2$]·MeOH (**18**·MeOH).

Procedure as for complex **16**, replacing saoH_2 with Et-saoH_2 (165 mg, 1mmol). X-ray quality crystals were grown by Et_2O diffusion into the MeOH solution in ~40% yield after 1 week. Elemental analysis: found (calc %) for $C_{48}H_{66}Fe_4N_{10}O_{10}$: C 49.11 (49.42), H 5.52 (5.70), N 11.47 (12.01).

$[Fe_9NaO_4(Et\text{-}sao)_6(hmp)_8]$·3MeCN·$Et_2O$ (**19**·3MeCN·Et_2O).

$FeCl_2.4H_2O$ (298 mg, 1.5 mmol), Et-saoH_2 (165 mg, 1 mmol), hmpH (163 mg, 1.5 mmol) and NaOMe (135 mg, 2.5 mmol) were stirred in MeCN for 18 hours. The solution was filtered and then diffused with Et_2O. X-ray quality crystals grew during 5 days in approximately 30% yield. Elemental analysis: found (calc %) for $C_{99.50}H_{102}Fe_9N_{13}NaO_{25.20}$: C 49.21 (49.61), H 3.92 (4.27), N 7.25 (7.56).

$[Fe_4(Et\text{-}sao)_4(hmp)_4]$·Et-sao$H_2$ (**20**·Et-saoH_2).

$FeCl_2.4H_2O$ (298 mg, 1.5 mmol), Et-saoH_2 (165 mg, 1 mmol), hmpH (163 mg, 1.5 mmol) and $Ca(OMe)_2$ (255 mg, 2.5 mmol) were stirred in MeCN for 18 hours. After filtration the solution was left to evaporate slowly, producing X-ray quality crystals after 5 days. Yield ~25%. Elemental analysis: found (calc %) for $C_{69}H_{71}Fe_4N_9O_{14}$: C 56.16 (56.23), H 4.64 (4.86), N 8.31 (8.55).

$[Fe_4(Ph\text{-}sao)_4(hmp)_4]$·6MeCN (**21**·6MeCN).

$FeCl_2.4H_2O$ (397 mg, 2 mmol), Ph-saoH_2 (416 mg, 2 mmol), hmpH (327 mg, 3 mmol) and NaOMe (162 mg, 3 mmol) were stirred in MeCN for 18 hours. The solution was filtered and left to evaporate slowly for 3 days, during which time X-ray quality crystals grew in ~25% yield. Elemental analysis: found (calc %) for $C_{80}H_{60}Fe_4N_8O_{12}$: C 62.43 (62.04), H 4.02 (3.90), N 7.40 (7.23).

$[Fe_9O_3(sao)(pdm)_6(N_3)_7(H_2O)]$ (**22**).

$Fe(BF_4)_2.6H_2O$ (337 mg, 1 mmol), saoH_2 (68 mg, 0.5 mmol), pdmH_2 (278 mg, 2 mmol) and NaN_3 (130 mg, 2 mmol) were stirred in a 50:50 mix of MeCN/MeOH (30ml). The solution was heated to 50˚C and stirred for a further 3 hours. After filtering off a brown precipitate, the solution was allowed to evaporate slowly. X-ray quality crystals grew during three days in ~20% yield. Elemental analysis found (calc. %) for $C_{49}H_{49}Fe_9N_{28}O_{18}$: C 32.53 (32.32), H 3.09 (2.71), N 21.28 (21.54).

3.2.2 Physical Measurements

Elemental analyses were performed by the EaStCHEM microanalysis service. Direct current magnetic susceptibility measurements were carried out on a Quantum Design MPMS-XL SQUID magnetometer equipped with a 7T magnet. Eicosane was used to restrain the microcrystalline samples and diamagnetic corrections were applied using Pascal's constants. Single crystal X-ray crystallography was performed using a Bruker SmartApex CCD diffractometer equipped with an Oxford Cryosystems LT device, using Mo-Kα radiation. Data collection parameters and structure solution and refinement details are listed in Table 1a and 1b. Full details can be found in the CIF files provided in the attached CD.

3.3 Results and Discussion

3.3.1 Synthesis

The general synthetic strategy adopted in this work was the introduction co-ligands into our previously successful reaction schemes that examined the coordination chemistry of R-saoH_2 ligands with Fe^{III} ions, in order to understand the effect of those co-ligands on the structural identity of the resultant cluster compound.[1-12]

The reaction of $FeCl_2.4H_2O$, saoH_2 and tacn in MeOH/CH_2Cl_2 with an excess of NEt_3 affords the tetranuclear 'butterfly' complex **16**. In the absence of the tacn co-ligand, there are no direct comparisons but the only clusters stabilised purely by R-saoH_2 ligands are two Fe_4 cubes, $[Fe_4(Me\text{-}sao)_4(Me\text{-}saoH)_4]\cdot MeOH$ and $[Fe_4(sao)_4(saoH)_4]\cdot saoH_2\cdot C_8H_{10}$.[4, 11]

The same reaction, employing Me-saoH_2 and Et-saoH_2 instead of saoH_2 and with the CH_2Cl_2 replaced with MeCN affords the structurally analogous complexes **17** and **18**, respectively. It is therefore clear to see that the change in the phenolic oxime, the change of solvent and indeed any change to the ratio of reactants employed, has no effect on the identity of the product, suggesting that the rigid, triangular face-capping tacn ligand is the dominant structural player. This contrasts

sharply to reactions performed in the absence of tacn, in which all these reaction variables do have prominent effects on the identity of the product. [1-12]

The reaction of $FeCl_2.4H_2O$, Et-saoH_2, hmpH and NaOMe in MeCN yields the large and very unusual nonanuclear complex **19**. The reaction can be considered *similar* to that which produced the butterfly complexes **16**-**18**, but in which the tacn has been replaced by hmpH. The molecule, **19**, therefore represents the difference between employing a rigid chelating ligand with one dominant coordination mode versus a flexible ligand which can possess numerous coordination modes – both chelating and bridging. The presence of a single Na^+ ion at the centre of the cluster suggested that the identity of the alkali metal ion used in the base would also have an important structure-directing role. Unfortunately we failed to isolate crystalline material from the use of other group 1 alkali metal cations, but the use of $Ca(OMe)_2$ did, with the isolation of the tetranuclear square complex **20** in which there is no Ca^{2+} present. Interestingly, although highly unusual, the [Fe^{III}_4] square topology is reminiscent of another oxime based, F-bridged square we published recently (*vide infra*).[17]

Repetition of the reaction which produces complex **20**, but replacing Et-saoH_2 with other R-saoH_2 family members does not produce any crystalline material, but perhaps somewhat oddly, repetition of the reaction which produces complex **19**, but replacing Et-saoH_2 with Ph-saoH_2 does produce the [Fe^{III}_4] square, **21**. In this instance we presume that it is the steric bulk of the oximic Ph-group that is the dominant structural factor. Indeed a close inspection of nonanuclear complex **18** suggests that the replacement of the Et- group with a Ph-group would likely be problematic from a simple steric consideration. This therefore gives us two routes to change from the large [Fe_9] complex to the smaller [Fe_4] complex: changing the charge on the cation, and/or increasing the bulk of the ketoxime group.

Switching from the hmpH ligand to the closely related pdmH_2 produces a second nonanuclear cage. The reaction of $Fe(BF_4)_2.6H_2O$, saoH_2, pdmH_2 and NaN_3 in MeOH/MeCN yields complex **22**. A direct comparison of the formulae of **19** and

22 suggests the pdm^{2-} ligand to be more dominant than the hmp- ligand; the pdm^{2-}:R-sao^{2-} ratio being 6:1 and the hmp^{-}:R-sao^{2-} ratio being 1.33:1.

3.3.2 Description of Structures

The molecular structures of complexes **16**-**18** are analogous, differing only in the identity of the R-sao^{2-} ligand, and so for the sake of brevity we describe only complex **16**. Centrosymmetric complex **16** (Figure 2) crystallises in the triclinic space group *P*-1 with two (analogous) $[Fe_4]$ molecules present in the unit cell. The metallic skeleton describes two edge-sharing $[Fe^{III}_3]$ triangles or, perhaps more conventionally, a $[Fe^{III}_4]$ 'butterfly'. Each triangle is scalene by strict definition, but isosceles based on ligand bridging modes. Central to each triangle is one μ_3-O^{2-} ion, forming the common $[Fe^{III}_3O]^{7+}$ moiety (or the $[Fe^{III}_4O_2]^{8+}$ butterfly), with the two unshared edges of the triangle bridged by sao^{2-} ligands in a familiar η^1:η^1:η^1:μ-mode. These lie alternately above and below the $[Fe^{III}_4]$ plane. The two η^3-tacn ligands each chelate a 'wing-tip' Fe^{III} ion completing the $[O_3N_3]$ donor set at this ion. These ions lie in distorted octahedral geometries that are perhaps best described as trigonal antiprisms.

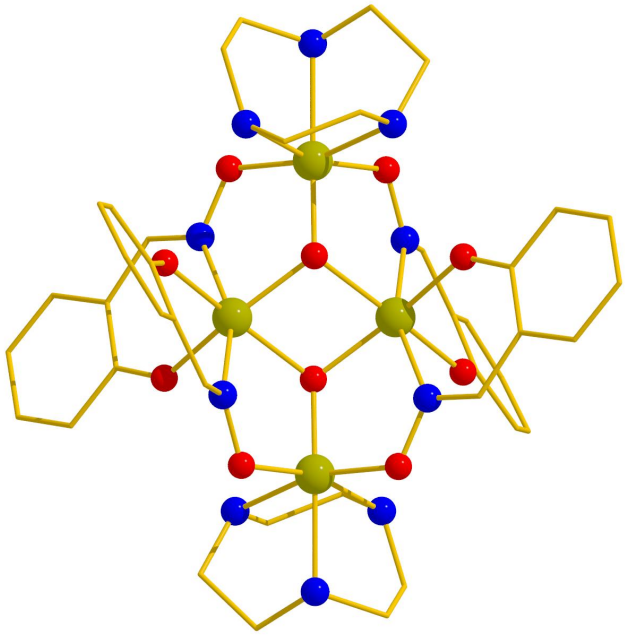

Fig. 2 The molecular structure of **16**. Colour code: Fe = olive green, O = red, N = blue, C = gold. H-atoms have been omitted for clarity.

The face-capping tacn ligands forcing a trigonal distortion (Fe…N, ~2.2 Å; Fe…O, ~1.9 Å). The 'body' Fe^{III} ions have $[O_4N_2]$ donor sets and lie in distorted octahedral environments with the four 'equatorial' Fe…O distances measuring ~2.0 Å, and the two 'axial' Fe…N distances being ~2.2 Å.

There are four intra-molecular H-bonds between the monodentate phenolic O-atoms of the sao^{2-} ligands and the N-atoms of the tacn ligands (O···N, 2.878-3.035 Å). The N-atoms and the oximic O-atoms are also involved in H-bonding to the H_2O and MeOH molecules in the lattice (2.754 – 3.062 Å). The closest cluster…cluster interactions occur between c-atoms in the phenolic oxime ligands at a distance of ~3.3 Å.

Complex **17** is the Me-sao^{2-} analogue and complex **3** the Et-sao^{2-} analogue of **16**. There are no significant structural differences between the three complexes. Both **17** and **18** however crystallise in the monoclinic space group $P2_1/c$ and this affords differences in the manner that the molecules pack in the crystal. The closest literature precedent for **16**-**18** are the complexes $[Fe_4O_2(tacn)_2(sao)_2(O_2CR)_2]$ reported by Chaudhuri and co-workers in which carboxylates bridge wing-tip and body Fe ions.[2, 3]

Complex **19** crystallises in the triclinic space group *P-1* (Fig. 3). The metallic skeleton (Fig. 3c) comprises a series of edge- and vertex-sharing $[Fe^{III}_3]$ triangular moieties. When also considering the four O^{2-} ions (2 x μ_4, 2 x μ_3) the core of the molecule can be described as two central $[Fe^{III}_3NaO]^{8+}$ tetrahedra sharing an edge, with both corners (at Fe6 and Fe2) connected to a peripheral $[Fe^{III}_3O]^{7+}$ triangle (Fig. 3d). The triangular units contain the $[Fe^{III}_3O(sao)_3]^+$ building block, commonly observed in M^{III}/R-sao^{2-} coordination chemistry. Each triangle is linked to a tetrahedron through a $\eta^1:\eta^1:\eta^2:\mu_3$- Et-$sao^{2-}$ (Fe2-Fe3 and Fe6-Fe7) ligand and one $\eta^1:\eta^2:\mu$ hmp^- ligand (Fe3-Fe4 and Fe7-Fe8). The additional edges on each triangle (Fe8-Fe9 and Fe4-Fe5) are bridged *via* one $\eta^1:\eta^1:\eta^1:\mu$-Et-sao^{2-} and one $\eta^1:\eta^2:\mu$-hmp^-. All remaining bridging within the central tetrahedra are *via* $\eta^1:\eta^1:\mu$-hmp^- ligands (Fe3-Na1, Fe1-Fe2, Fe1-Fe6 and Fe7-Na1).

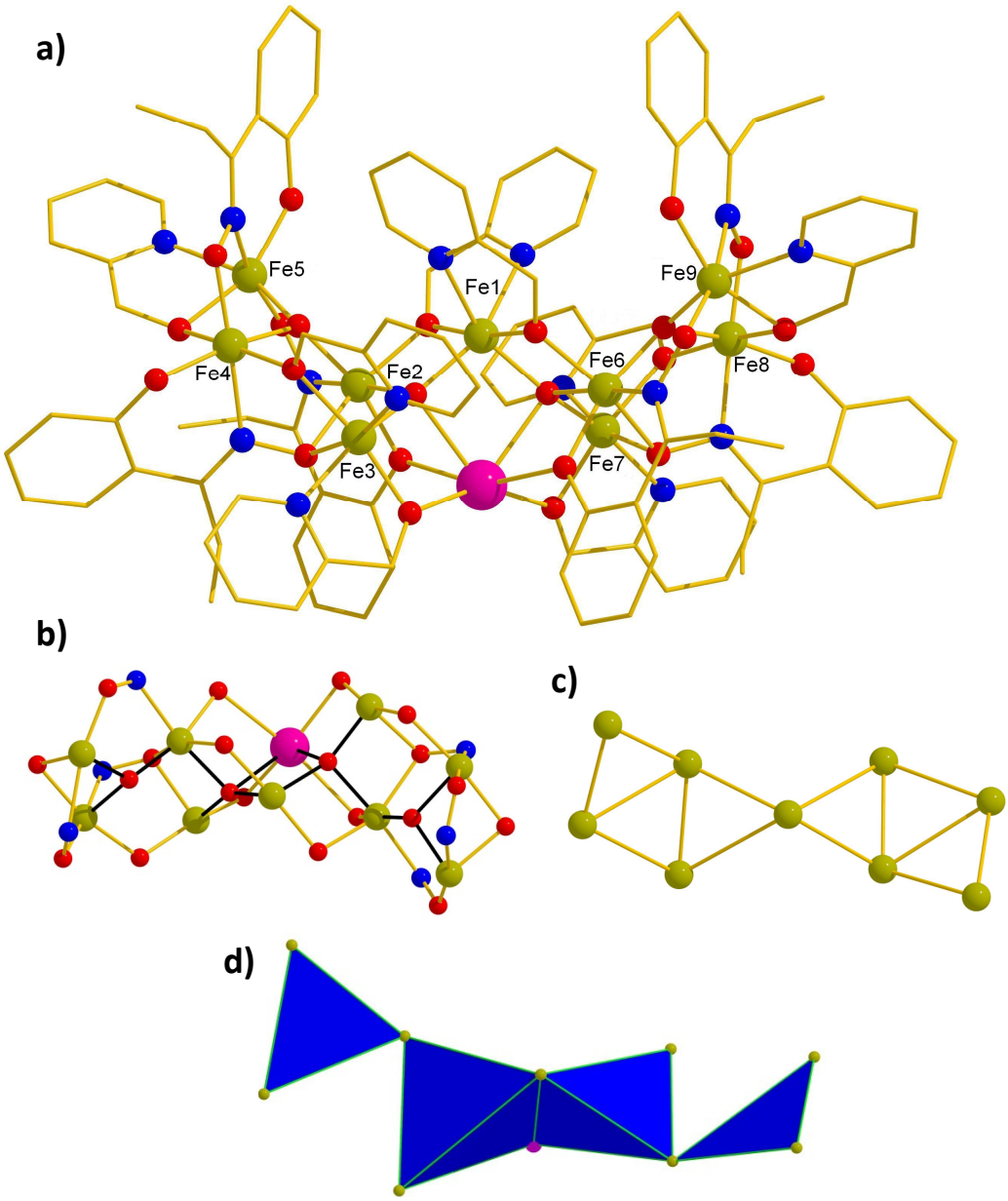

Fig. 3 (a)The molecular structure of **19**. (b) The ligand core with black bonds between central oxides. (c) Fe^{III} metallic core. (d) Triangular and tetrahedral building blocks based on oxide centres. Colour code: Fe = olive green; O = red; N = blue; C = gold; Na = magenta. H atoms have been removed for clarity.

All the Fe^{III} ions lie in distorted octahedral geometries with *cis* angles in the range 73.54-114.17˚ and *trans* angles in the range 152.17-176.60˚. There are two different coordination spheres present for the Fe^{III} ions: $[O_5N]$ for Fe4, Fe2, Fe6 and Fe8 and $[O_4N_2]$ for Fe5, Fe3, Fe1, Fe7 and Fe9. The Na^+ ion is six coordinate and in

a very distorted environment, coordinated to six O-atoms with bond lengths of ~2.3 Å to the two hmp^- O-atoms, ~2.4 Å to the two O^{2-} ions and ~2.6 Å to the phenolic O-atoms of the Et-sao^{2-} ligand. There are no intra- or inter-molecular H-bonds, with the shortest inter-molecular interactions occuring between phenolic O-atoms from the Et-sao^{2-} ligands and C-atoms on the pyridyl ring of the hmp^- ligands, at a distance of approximately 3.2 Å.

19 now becomes the largest nuclearity cluster to be synthesised containing the R-$saoH_2$ ligands and joins a relatively uncommon nuclearity group of Fe_9. A CCDC database search reveals only 73 Fe_9 molecules in comparison with the 535 Fe_6 molecules for example.

Complex **20** (Figure 4) crystallises in the triclinic space group *P-1* with one Fe cluster and one Et-$saoH_2$ ligand in the asymmetric unit. The metallic core of **20** describes a distorted [Fe^{III}_4] square with Fe…Fe lengths of 3.459-3.474 Å and Fe-Fe-Fe angles of 86.97-88.53˚. Each edge is bridged by a combination of one Et-sao^{2-} ligand bridging in a $\eta^1:\eta^1:\eta^1:\mu$- fashion and one hmp^- ligand bridging in a $\eta^1:\eta^2:\mu$- fashion mode. These lie alternately above and below the [Fe^{III}_4] 'plane'. In fact the [Fe4] square is very distorted and non-planar as can be seen from Fig. 4c.

Each iron is in the 3+ oxidation state lies in an octahedral geometry with a [O_4N_2] donor set, with *cis* angles of 75.55-105.18° and *trans* angles of 152.32-175.39°. There is an inter-molecular H-bond to the co-crystallised Et-$saoH_2$ molecule in the lattice, between the phenolic O-atom of the coordinated oxime ligand and the oximic O-atom of the non-coordinated Et-$saoH_2$ molecule (O…O, 2.691 Å). The closest cluster…cluster interactions are of the order of 3.4 Å between C-atoms on neighbouring Et-sao^{2-} ligands.

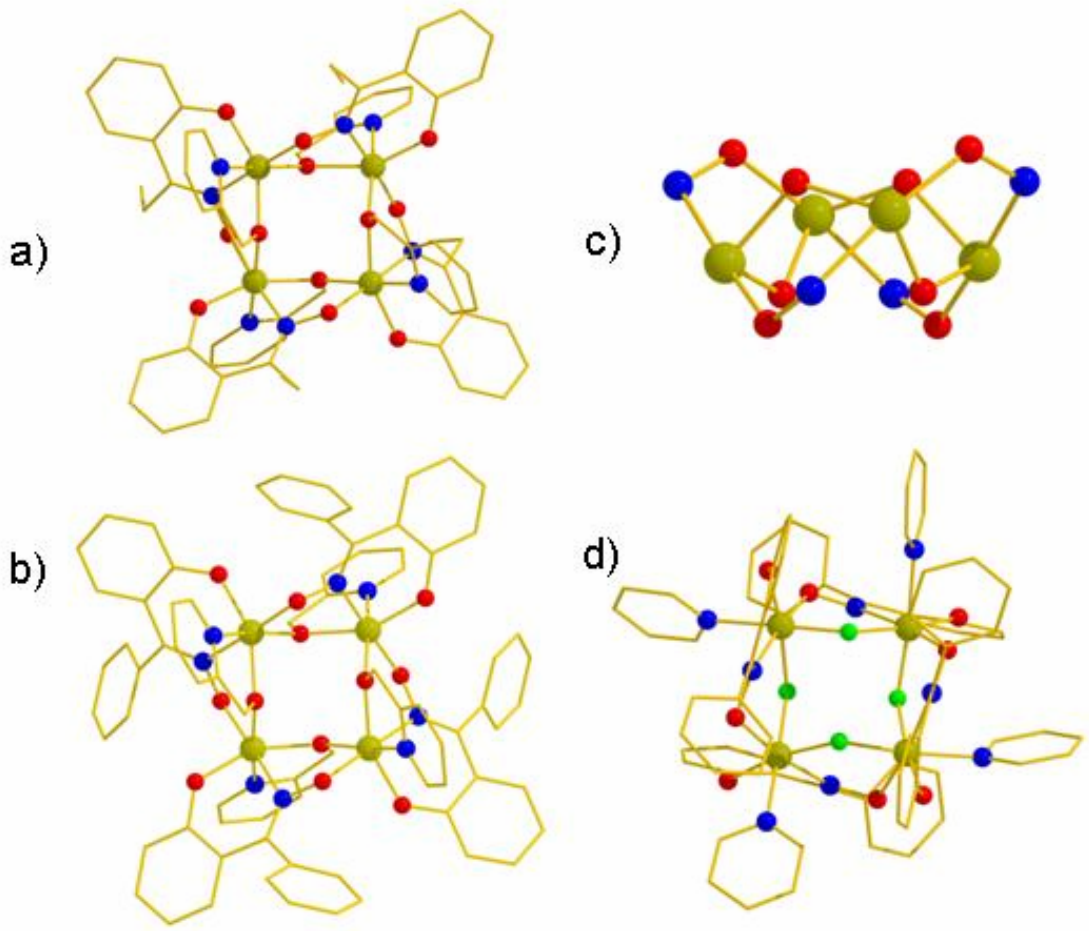

Fig. 4 The molecular structures of complexes (a) **20** and (b) **21** viewed perpendicular to the $[Fe_4]$ face. (c) The structure of **6** viewed parallel to the $[Fe_4]$ face highlighting the non-planar nature of the square. (d) The structure of the complex **3**, $[Fe_4F_4(Ph\text{-}sao)_4(py)_4]$.

Complex **21** crystallises in the tetragonal space group $I4_1/a$ with one molecule in the asymmetric unit and four within the unit cell (Fig. 4). The cluster is isostructural with complex **20**, differing only in the identity of the R-saoH_2 ligand. Symmetry now forces all of the Fe…Fe distances to be equivalent (3.451 Å) and the Fe-Fe-Fe angles are 86.33˚ - again describing a distorted non-planar $[Fe_4]$ square. The octahedral Fe^{III} ions have *cis* angles in the range 80.25-104.6° and *trans* angles in the range 154.89-173.52°. There are a number of inter molecular interactions within the crystal lattice, most noticeably π-π stacking between two neighbouring hmp^- ligands (C···C, ~3.3 Å), with the shortest inter-molecular distance being

between a phenolic O-atom and the pyridyl C-atoms of an hmp^- ligand (O···C 3.208 Å).

Clusters with the $[Fe^{III}_4]$ square topology are very rare – indeed a search of the CCDC database returns only 8 hits when all bridges are the same (47 total). Interestingly however, complexes **20** and **21** are very similar to the complex **3**, $[Fe_4F_4(Ph\text{-}sao)_4(py)_4]$ from chapter one.[7] A comparison of the structures is given in Figure 4. It is easy to see that the μ-F and the terminally bonded pyridine in the latter complex have simply been replaced by the hmp^- ligand in **20** and **21** which combines both coordination modes.

Complex **22** crystallises in the orthorhombic space group $Pna2_1$ (Figure 5). The metallic skeleton consists of six fused $[Fe^{III}_4]$ tetrahedra with each tetrahedron sharing a face with its neighbour. Central to the molecule are three O^{2-} ions, two bonding in a μ_4-fashion and one bonding in a μ_3-fashion (Fig. 5b). The core can thus be described as two $[Fe^{III}_4O^{2-}]^{10+}$ tetrahedra sharing a vertex (at Fe4) with an additional $[Fe^{III}_3O^{2-}]^{7+}$ triangle sharing a vertex at Fe2. Only one sao^{2-} ligand is present in the molecule, bridging in a $\eta^1{:}\eta^1{:}\eta^1{:}\mu$ mode between Fe5 and Fe6. The more prevalent ligand is the pdm^{2-} ligand, with six present in the molecule, all bridging in a $\eta^2{:}\eta^1{:}\eta^2{:}\mu_3$-mode except from the one bridging Fe7-Fe8 which only bridges two metals in a $\eta^1{:}\eta^1{:}\eta^2{:}\mu_3$-mode. The four remaining edges are bridged by end-on N_3^- ligands, with three terminally bonded N_3^- ligands filling the remaining coordination sites on the Fe centres. The end-on azide bridge between Fe^{III} centres is particularly rare with a CCDC search revealing only two diiron complexes, each of which displays ferromagnetic exchange.[37, 38] Our previous efforts to incorporate azide bridges resulted in only a partial displacement (15%) of a μ-OMe^- bridge in the molecule $[Fe_8O_2(OMe)_{3.85}(N_3)_{4.15}(Me\text{-}sao)_6(py)_2]$ from chapter one. This makes **22** the first cluster to contain end-on azide bridges of nuclearity greater than two.

Eight of the Fe^{III} ions lie in distorted octahedral geometries with *cis* angles of 73.63-128.39° and *trans* angles of 138.45-177.71°. The remaining Fe ion (Fe4) is in a pentagonal bipyramidal geometry; equatorial angles between adjoining points on

the pentagon are in the range 69.22-79.16°, angles between axial and equatorial sites are in the range 73.44-105.20° and the angle between the axial-axial sites is 176.79°.

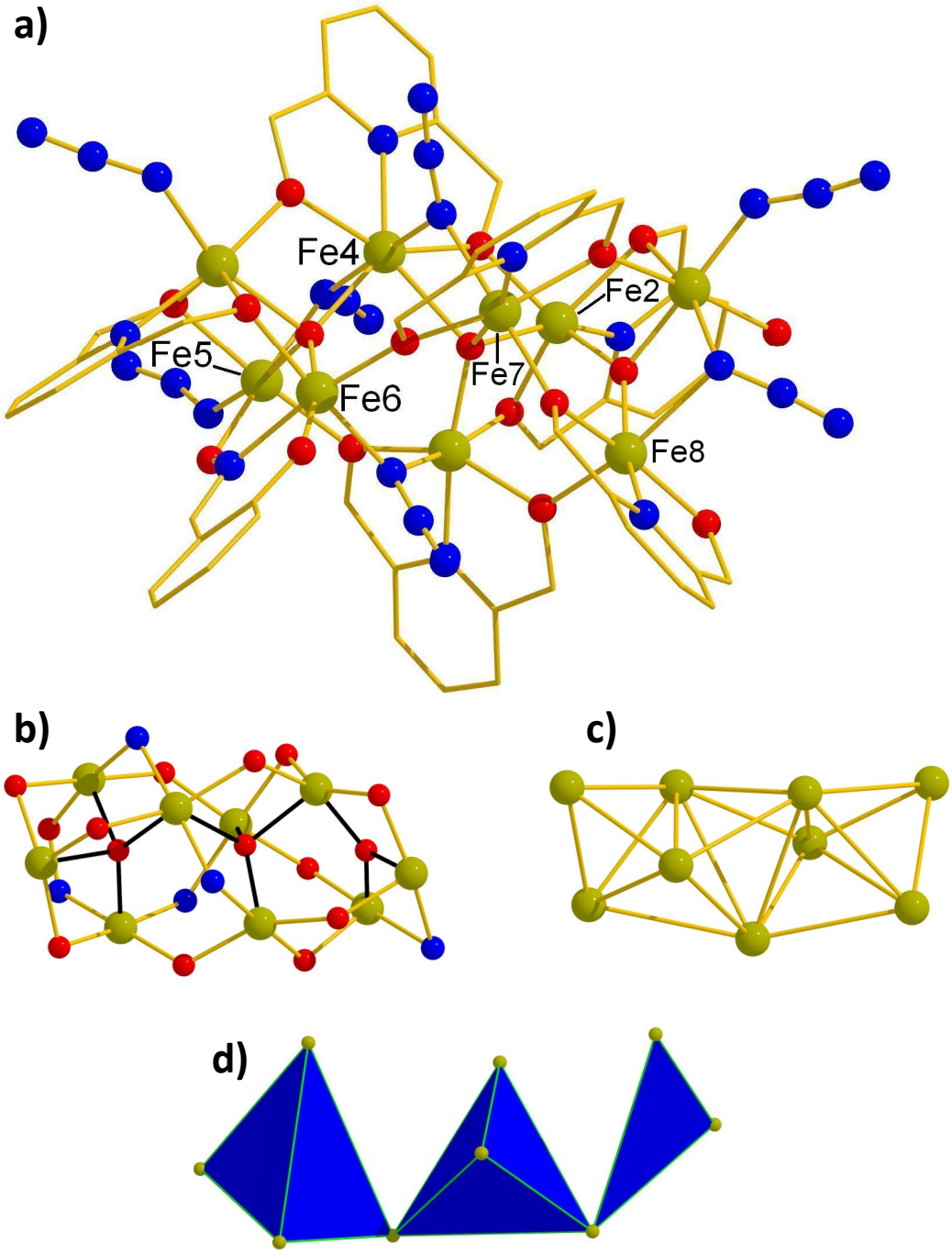

Fig. 5 (a) The molecular structure of **22**. (b) The ligand core with black bonds between central oxides. (c) Fe^{III} metallic core. (d) Triangular and tetrahedral building blocks based on oxide centres. Colour code: Fe = olive green; O = red; N = blue; C = gold. H atoms have been removed for clarity.

All of the octahedral Fe^{III} centres have a $[O_4N_2]$ donor set and the pentagonal bipyramidal Fe^{III} centre has a $[O_5N_2]$ donor set. There are no inter molecular hydrogen bonds, with the shortest contacts between neighbouring molecules being between a bridging azide ions and the pyridyl ring of a pdm^{2-} ligand (C···N 3.033 Å).

Table 1a Crystallographic details for complexes **16**-**19**

	16·2MeOH·H_20	**17**·2MeCN	**18**·MeOH	**19**·3MeCN·Et_2O
M, $gmol^{-1}$	1136.40	1274.60	1197.25	2606.07
crystal system	Triclinic	Monoclinic	Monoclinic	Triclinic
space group	*P-1*	$P2_1/c$	$P2_1$/c	*P-1*
a, Å	11.7667(14)	12.4265(3)	15.0460(3)	16.3371(5)
b, Å	11.9297(15)	14.7726(4)	16.9478(4)	17.1987(11)
c , Å	17.708(2)	16.5738(5)	21.1677(5)	25.7824(9)
α, deg	77.837(6)	90	90	88.455(4)
β, deg	76.857(6)	106.032(3)	102.437(2)	71.706(3)
γ, deg	76.716(6)	90	90	64.484(4)
V , $Å^3$	2322.6(5)	2924.14(14)	5271.0(2)	6157.5(6)
T , K	100	100	100	100
Z	2	2	2	2
$\rho_{, calc}$ [g cm^{-3}]	1.625	1.448	1.490	1.41
crystal shape and colour	black block	brown block	black block	black block
crystal size [mm]	0.13 x 0.13 x 0.13	0.23 x 0.14 x 0.12	0.20 x 0.15 x 0.04	0.52 x 0.33 x 0.21
μ, [mm^{-1}]	1.300	1.040	9.207	8.876
unique data	9510	6595	10298	13409
unique data, (I >	7739	5212	5332	11558
R1[a], wR2[b]	0.0578, 0.1592	0.0430, 0.0716	0.0740, 0.0648	0.0655, 0.0622
goodness of fit	1.104	1.151	1.1218	1.2051

[a] $R1$) $\sum(|Fo| - |Fc|)/\sum(|Fo|)$ for observed reflections. [b] wR_2) $\{\sum[w(Fo^2 - Fc^2)_2]/\sum[w(Fo^2)_2]\}^{1/2}$ for all data.

Table 1b Crystallographic details for complexes **20**-**22**

	20·Et-saoH$_2$	**21**·6MeCN	**22**
M, gmol^{-1}	1473.75	1756.07	1820.73
crystal system	Triclinic	Tetragonal	Orthorhombic
space group	*P-1*	*I4$_1$/a*	*Pna2$_1$*
a, Å	12.4159(7)	18.619(4)	29.2462(9)
b, Å	16.4389(7)	18.619(4)	17.0864(6)
c , Å	17.9303(9)	25.806(5)	14.8911(6)
α, deg	73.102(4)	90	90
β, deg	89.225(4)	90	90
γ, deg	68.303(5)	90	90
V , Å^3	3235.3(3)	8946(3)	7441.3(5)
T , K	150(2)	100	100
Z	2	4	4
ρ, calc [g cm^{-3}]	1.513	1.304	1.625
crystal shape and colour	black block	black block	black block
crystal size [mm]	0.45 × 0.17 × 0.05	0.11 x 0.09 x 0.07	0.07 x 0.04 x 0.04
μ, [mm^{-1}]	7.669	0.702	14.339
unique data	8912	3913	9362
unique data, (I >	7314	2906	7278
R1[a], wR2[b]	0.0359, 0.0797	0.0688, 0.0684	0.0953, 0.0982
goodness of fit	1.021	1.0533	1.1201

[a] $R1$) $\sum(|Fo| - |Fc|)/\sum(|Fo|)$ for observed reflections. [b] wR_2) $\{\sum[w(Fo^2 - Fc^2)_2]/\sum[w(Fo^2)_2]\}^{1/2}$ for all data.

3.3.3 Magnetism

Direct current (dc) magnetic susceptibility studies were performed for complexes **17**, **19**, **21** and **22** between 5-300 K with an applied field of 0.1 T. These are plotted as the $\chi_M T$ product versus T in Figure 6.

Complex **17** lower than the expected value for four non-interacting Fe^{III} centres (17.5 cm^3 K mol^{-1}), suggestive of strong antiferromagnetic exchange. The value of $\chi_M T$ continues to drop with decreasing temperature, reaching 0 cm^3 K mol^{-1} at ~25 K. The data can be fitted (blue line in Figure 6) with a simple isotropic (g = 2.00) Hamiltonian that assumes all the Fe…Fe interactions are equivalent ($\hat{H} = -2J(\hat{S}_1 \cdot \hat{S}_2 + \hat{S}_1 \cdot \hat{S}_3 + \hat{S}_2 \cdot \hat{S}_3 + \hat{S}_2 \cdot \hat{S}_4 + \hat{S}_3 \cdot \hat{S}_4)$. This affords J = -61 cm^{-1}. The S = 0 ground spin state is S = 0 has an energy level of -2897.5 cm^{-1} with the first excited (S = 1) state 122 cm^{-1} higher in energy (Figure 7). For comparison the similar complex $[L_2Fe_2(\mu_3\text{-}O)_2(salox)_2(diphenylglycolate)_3Fe_2](ClO_4)$ (L = 1,4,7-trimethyl-1,4,7-triazacyclononane) made by Chaudhuri *et al*[2] quotes a J value of 41.4 cm-1 and all published J values fall in the range -33 to -46 cm-1 for J interactions.[39, 40]

Complex **19** and **22** are described together as both display similar properties. **19** and **22** have room temperature $\chi_M T$ values of 12.43 cm^3 mol^{-1} K and 14.9 cm^3 mol^{-1} K which are lower than the expected value for nine non-interacting Fe^{III} centres at this temperature (39.375 cm^3 mol^{-1} K). This immediately indicates the presence of dominant antiferromagnetic exchange between the centres. As the temperature is decreased the magnetic susceptibility decreases to lows at 4.49 cm^3 mol^{-1} K for **19** and 4.1 cm^3 mol^{-1} K for **22** at 5 K. This would point to a spin ground state of 5/2 for both, an expected result for an odd-membered Fe^{III} cluster. The size of the metallic core and number of exchange pathways present rules out simulations using our available software. We could however fit the field dependant magnetisation at low temperature to confirm S = 5/2 ground states and produce values for **19** (Figure 9) of g = 2.05 and D = 0.653 and for **22** (Figure 10) of g = 1.95 and D = 0.301. The relatively small values for **22** point to the presence of low lying excited states, and we can assume the partial occupancy of the S = 3/2 excited state. A plot of $1/\chi_M$ vs.

T affords θ = -206.64 K for **19** and θ = -467.2 K for **22** again indicative of strong antiferromagnetic exchange.

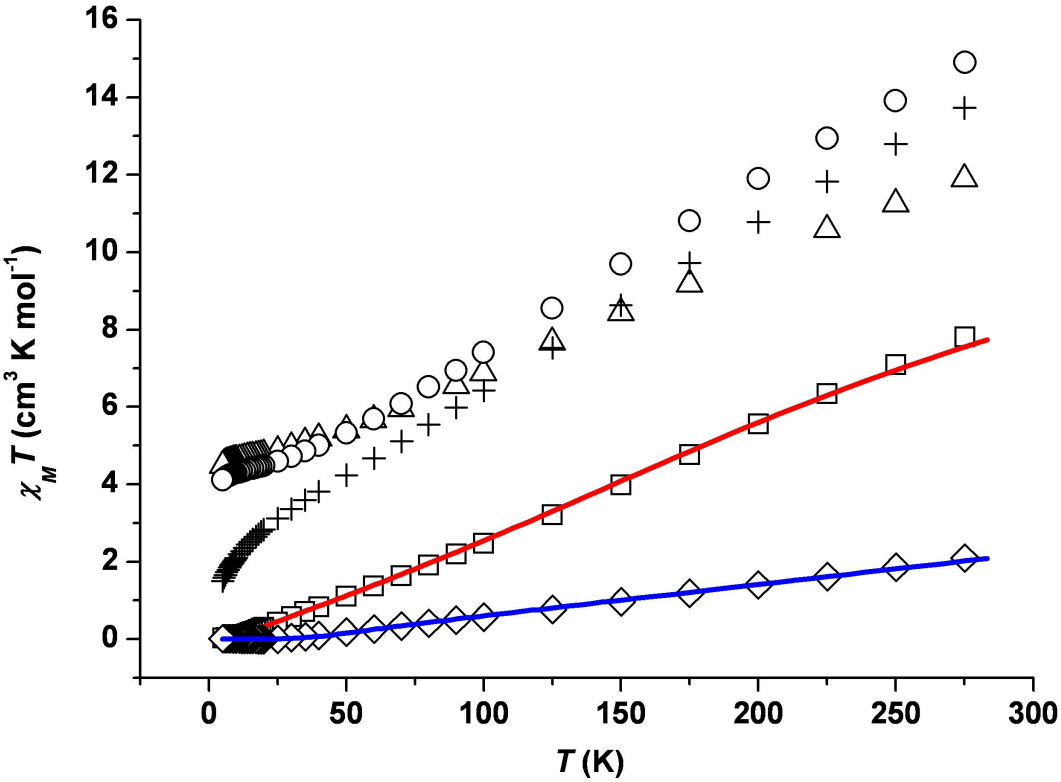

Fig. 6 Plot of χ_MT vs T for complexes **17** (diamonds) and **19** (triangles), **21** (squares) and **22** (circles). The solid blue and red lines represent a simulation of the experimental data of **17** and **21** respectively, as detailed in the text. A plot of complex **3** is shown again for comparison (crosses).

Complex **21** has a room temperature χ_MT value of 7.8 cm^3 mol^{-1} K, lower than the expected value for four non-interacting Fe^{III} centres (17.5 cm^3 K mol^{-1}). The χ_MT value decreases with decreasing temperature reaching 0 cm^3 K mol^{-1} by 10 K, indicative of a diamagnetic ground state.

The data can be fitted to a simple isotropic (g = 2.00) Hamiltonian assuming the Fe…Fe interactions around the square are equivalent ($\hat{H}$ = -2J($\hat{S}_1 \cdot \hat{S}_2$ + $\hat{S}_1 \cdot \hat{S}_3$ + $\hat{S}_2 \cdot \hat{S}_4$ + $\hat{S}_3 \cdot \hat{S}_4$). This affords an exchange interaction of J = -13.6 cm^{-1} with first excited (S = 1) state 27.2 cm^{-1} above the S = 0 ground state (Figure 8).

It is interesting to compare the exchange interactions for complexes **17** (mediated by oxime -N-O- and O^{2-}) and **19** (mediated by oxime -N-O- and ^{-}OR), with the former almost five times stronger than the latter, simply reflecting the presence of oxide versus alkoxide.[41] We can also compare the data for **19** to that previously reported for the complex $[Fe_4F_4(Ph\text{-}sao)_4(py)_4]$. The presence of more than one $[Fe_4]$ molecule in the unit cell of the latter complex precluded any fitting of the data, but a simple qualitative comparison of the data in Figure 6 suggests that the exchange mediated by the F-bridges is rather weaker than that mediated by the alkoxides.

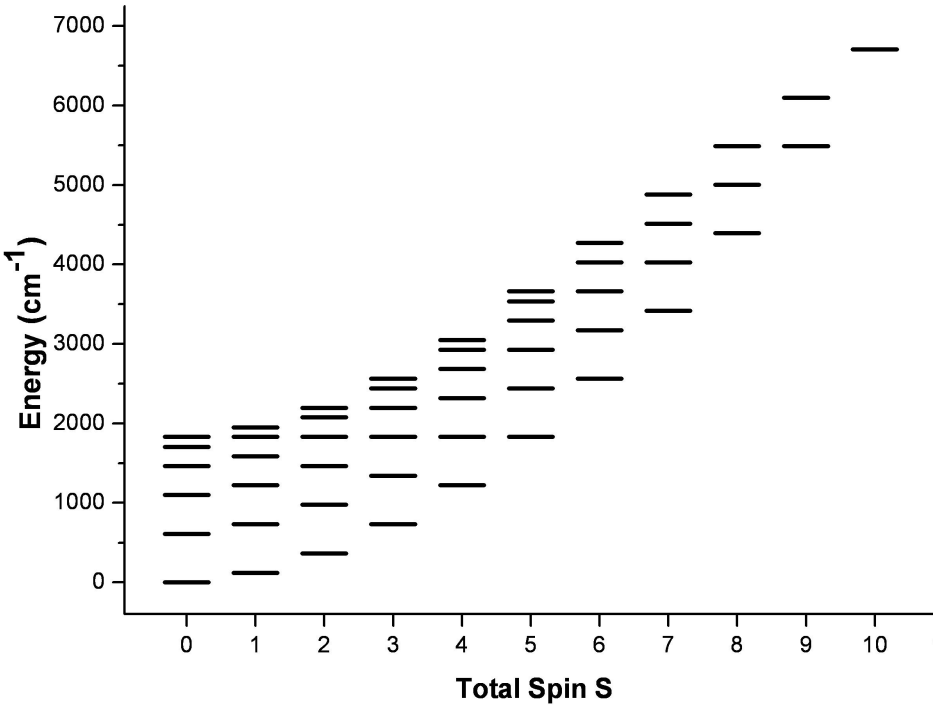

Fig. 7 E vs total S for complex **17**. Lowest energy level set to zero.

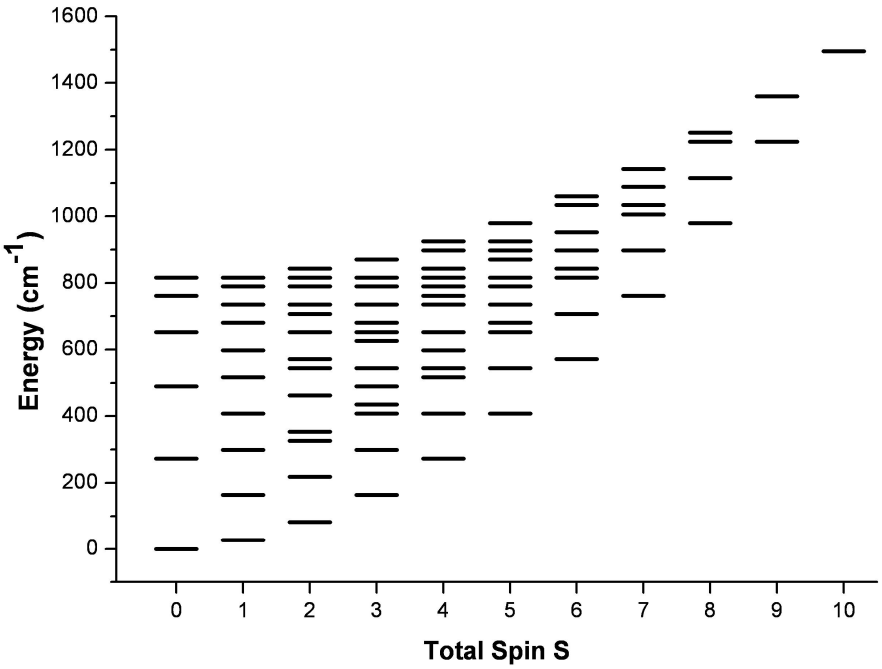

Fig. 8 E vs total S for complex **21**. Lowest energy level set to zero.

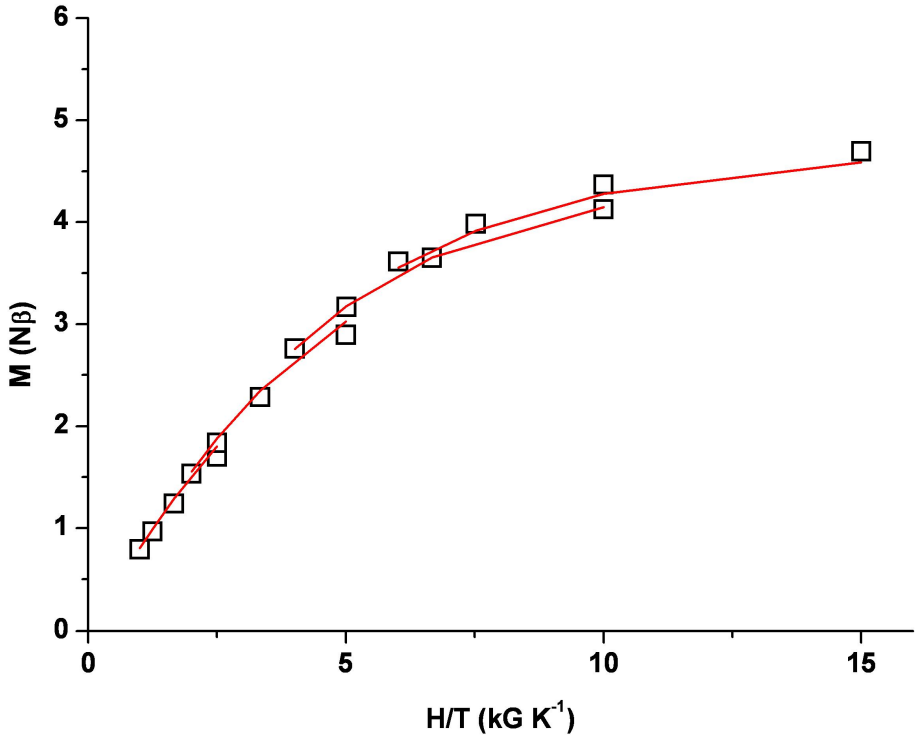

Fig. 9 M vs H/T for complex **19**. The red line indicates a theoretical fit of the data. Both the data is fitted to four fields between 5 and 30 kG with a temperature range of 2-5 K.

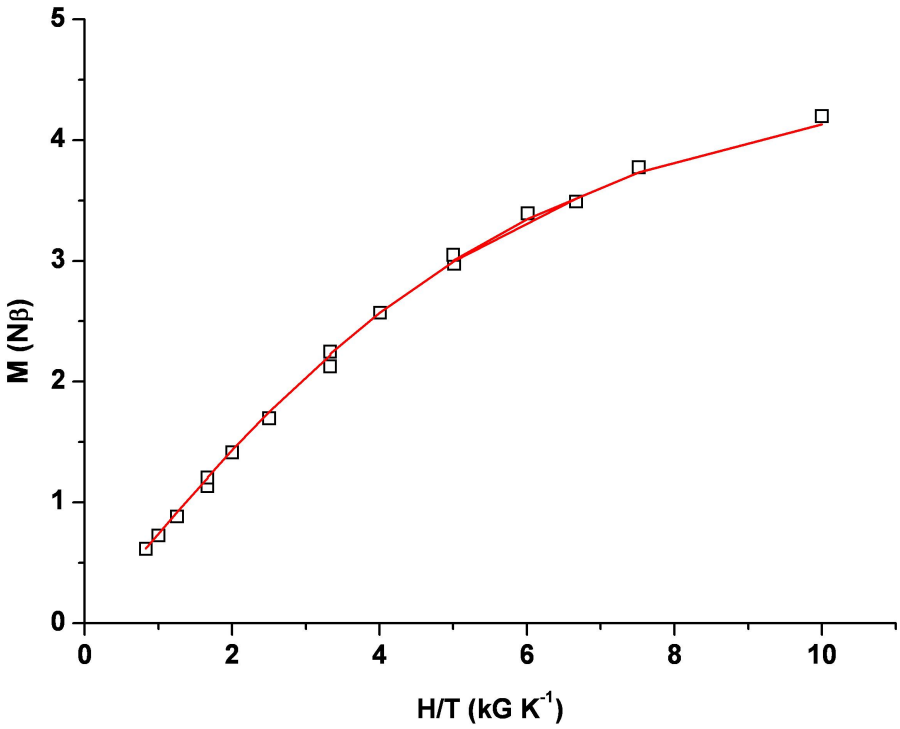

Fig. 10 M vs H/T for complex **22**. The red line indicates a theoretical fit of the data. The data is fitted to four fields between 5 and 30 kG with a temperature range of 3-6 K.

3.4 Conclusions

Seven new clusters have been added to the Fe-salicylaldoxime family synthesised by employing co-ligands (namely tacn, hmpH and $pdmH_2$) that are able to compete with the oxime ligands for the Fe coordination sites. This has resulted in a set of tetranuclear 'butterfly' clusters with the ligand tacn that display very strong antiferromagnetic exchange interactions and diamagnetic ground states. The pro-ligand hmpH produced three clusters; two tetranuclear squares formed *via* two entirely different routes and an unusual nonametallic cage. The related pro-ligand $pdmH_2$ stabilised another intriguing [Fe_9] cluster containing some structural oddities, including a rare example of Fe^{III} ions bridged by end-on azides that has only been observed prior in two dinuclear Fe^{III} clusters and the first occurrence of a pentagonal bipyramidal geometry Fe^{III} centre in Fe-salicylaldoxime chemistry.

The results continue to highlight the predominance of the triangular $[Fe_3O]^{7+}$ and tetrahedral $[Fe_4O]^{10+}$ building blocks, especially in the two Fe_9 complexes, **19** and **22**, where we see the co-ligands working with the phenolic oxime to form clusters that at first viewing appear peculiar and complicated but can be broken down into a series of the defined building blocks. **19** and **22** are now the largest nuclearity clusters built with phenolic oximes and they display an $S = 5/2$ ground state.

3.5 References

1. E. Bill, C. Krebs, M. Winter, M. Gerdan, A. X. Trautwein, U. Flörke, H.-J. Haupt and P. Chaudhuri, *Chem. Eur. J*, 1997, **3**, 193.
2. P. Chaudhuri, E. Rentschler, F. Birkelbach, C. Krebs, E. Bill, T. Weyhermüller and U. Flörke, *Eur. J. Inorg. Chem.*, 2003, **2003**, 541.
3. P. Chaudhuri, M. Winter, P. Fleischhauer, W. Haase, U. Flörke and H.-J. r. Haupt, *Inorg. Chim. Acta*, 1993, **212**, 241.
4. I. A. Gass, C. J. Milios, A. Collins, F. J. White, L. Budd, S. Parsons, M. Murrie, S. P. Perlepes and E. K. Brechin, *Dalton Trans.*, 2008, **15**, 2043.
5. I. A. Gass, C. J. Milios, A. G. Whittaker, F. P. A. Fabiani, S. Parsons, M. Murrie, S. P. Perlepes and E. K. Brechin, *Inorg. Chem.*, 2006, **45**, 5281.
6. K. Mason, J. Chang, E. Garlatti, A. Prescimone, S. Yoshii, H. Nojiri, J. Schnack, P. A. Tasker, S. Carretta and E. K. Brechin, *Chem. Commun.*, 2011, **47**, 6018.
7. K. Mason, I. A. Gass, S. Parsons, A. Collins, F. J. White, A. M. Z. Slawin, E. K. Brechin and P. A. Tasker, *Dalton Trans.*, 2010, **39**, 2727.
8. K. Mason, I. A. Gass, F. J. White, G. S. Papaefstathiou, E. K. Brechin and P. A. Tasker, *Dalton Trans.*, 2011, **40**, 2875.
9. C. P. Raptopoulou, A. K. Boudalis, Y. Sanakis, V. Psycharis, J. M. Clemente-Juan, M. Fardis, G. Diamantopoulos and G. Papavassiliou, *Inorg. Chem.*, 2006, **45**, 2317.
10. C. P. Raptopoulou, Y. Sanakis, A. K. Boudalis and V. Psycharis, *Polyhedron*, 2005, **24**, 711.
11. J. M. Thorpe, R. L. Beddoes, D. Collison, C. D. Garner, M. Helliwell, J. M. Holmes and P. A. Tasker, *Angew. Chem. Int. Ed*, 1999, **38**, 1119.
12. C. N. Verani, E. Bothe, D. Burdinski, T. Weyhermüller, U. Flörke and P. Chaudhuri, *Eur. J. Inorg. Chem.*, 2001, **2001**, 2161.
13. E. K. Brechin, M. J. Knapp, J. C. Huffman, D. N. Hendrickson and G. Christou, *Inorg. Chim. Acta*, 2000, **297**, 389.
14. C. A. Christmas, H. L. Tsai, L. Pardi, J. M. Kesselman, P. K. Gantzel, R. K. Chadha, D. Gatteschi, D. F. Harvey and D. N. Hendrickson, *J. Am. Chem. Soc.*, 1993, **115**, 12483.
15. J. M. Clemente-Juan, C. Mackiewicz, M. Verelst, F. Dahan, A. Bousseksou, Y. Sanakis and J.-P. Tuchagues, *Inorg. Chem.*, 2002, **41**, 1478.
16. S. Drüeke, K. Wieghardt, B. Nuber, J. Weiss, E. L. Bominaar, A. Sawaryn, H. Winkler and A. X. Trautwein, *Inorg. Chem.*, 1989, **28**, 4477.
17. P. Poganiuch, S. Liu, G. C. Papaefthymiou and S. J. Lippard, *J. Am. Chem. Soc.*, 1991, **113**, 4645.
18. T. Taguchi, T. C. Stamatatos, K. A. Abboud, C. M. Jones, K. M. Poole, T. A. O'Brien and G. Christou, *Inorg. Chem.*, 2008, **47**, 4095.

19. T. Taguchi, M. S. Thompson, K. A. Abboud and G. Christou, *Dalton Trans.*, 2010, **39**, 9131.
20. K. Wieghardt, U. Bossek and W. Gebert, *Angew. Chem. Int. Ed*, 1983, **22**, 328.
21. K. Wieghardt, K. Pohl and W. Gebert, *Angew. Chem. Int. Ed*, 1983, **22**, 727.
22. K. Wieghardt, K. Pohl, I. Jibril and G. Huttner, *Angew. Chem. Int. Ed*, 1984, **23**, 77.
23. A. L. Barra, A. Caneschi, A. Cornia, F. Fabrizi de Biani, D. Gatteschi, C. Sangregorio, R. Sessoli and L. Sorace, *J. Am. Chem. Soc.*, 1999, **121**, 5302.
24. A.-L. Barra, F. Bencini, A. Caneschi, D. Gatteschi, C. Paulsen, C. Sangregorio, R. Sessoli and L. Sorace, *ChemPhysChem*, 2001, **2**, 523.
25. C. Boskovic, E. K. Brechin, W. E. Streib, K. Folting, J. C. Bollinger, D. N. Hendrickson and G. Christou, *J. Am. Chem. Soc.*, 2002, **124**, 3725.
26. C. Boskovic, W. Wernsdorfer, K. Folting, J. C. Huffman, D. N. Hendrickson and G. Christou, *Inorg. Chem.*, 2002, **41**, 5107.
27. N. C. Harden, M. A. Bolcar, W. Wernsdorfer, K. A. Abboud, W. E. Streib and G. Christou, *Inorg. Chem.*, 2003, **42**, 7067.
28. L. Lecren, O. Roubeau, C. Coulon, Y.-G. Li, X. F. Le Goff, W. Wernsdorfer, H. Miyasaka and R. Clérac, *J. Am. Chem. Soc.*, 2005, **127**, 17353.
29. M. Murugesu, M. Habrych, W. Wernsdorfer, K. A. Abboud and G. Christou, *J. Am. Chem. Soc.*, 2004, **126**, 4766.
30. E. C. Sañudo, E. K. Brechin, C. Boskovic, W. Wernsdorfer, J. Yoo, A. Yamaguchi, T. R. Concolino, K. A. Abboud, A. L. Rheingold, H. Ishimoto, D. N. Hendrickson and G. Christou, *Polyhedron*, 2003, **22**, 2267.
31. T. C. Stamatatos, K. A. Abboud, W. Wernsdorfer and G. Christou, *Angew. Chem. Int. Ed*, 2006, **45**, 4134.
32. T. C. Stamatatos, K. M. Poole, K. A. Abboud, W. Wernsdorfer, T. A. O'Brien and G. Christou, *Inorg. Chem.*, 2008, **47**, 5006.
33. T. C. Stamatatos, G. C. Vlahopoulou, C. P. Raptopoulou, A. Terzis, A. Escuer and S. P. Perlepes, *Inorg. Chem.*, 2009, **48**, 4610.
34. E.-C. Yang, W. Wernsdorfer, L. N. Zakharov, Y. Karaki, A. Yamaguchi, R. M. Isidro, G.-D. Lu, S. A. Wilson, A. L. Rheingold, H. Ishimoto and D. N. Hendrickson, *Inorg. Chem.*, 2005, **45**, 529.
35. W. R. Dunstan and T. A. Henry, *J. Chem. Soc., Trans.*, 1899, **75**, 66.
36. H. Koyama and T. Yoshino, *Bull. Chem. Soc. Jpn.*, 1972, **45**, 481.
37. G. De Munno, T. Poerio, G. Viau, M. Julve and F. Lloret, *Angew. Chem. Int. Ed*, 1997, **36**, 1459.
38. K. R. Reddy, M. V. Rajasekharan and J. P. Tuchagues, *Inorg. Chem.*, 1998, **37**, 5978.
39. T. Cauchy, E. Ruiz and S. Alvarez, *J. Am. Chem. Soc.*, 2006, **128**, 15722.
40. S. Gomez-Coca, T. Cauchy and E. Ruiz, *Dalton Trans.*, 2010, **39**, 4832.
41. H. Weihe and H. U. Güdel, *J. Am. Chem. Soc.*, 1997, **119**, 6539.

Chapter 4
Linking [M^{III}_3] triangles with “double-headed” Phenolic oximes

4.1 Introduction

The development of crystal engineering and the synthesis of porous materials having metal organic frameworks (MOFs) has made extensive use of metal complexes as connecting nodes in lattices.[1-8] Transition metal complexes of phenolic oximes have great potential as building blocks in supramolecular chemistry because they form two very stable types of platform which are easily functionalised *via* the benzene rings (Fig. 1a and 1b).[9] In this chapter we aim to expand on the 'simple' phenolic oxime and strap two units together in the 3-position, using ligands with aliphatic α,Ω-aminomethyl links (Fig. 1c). This allows the assembly of polynuclear complexes which bring together the most common building blocks previously discussed and seen in Fig. 1. [10, 11]

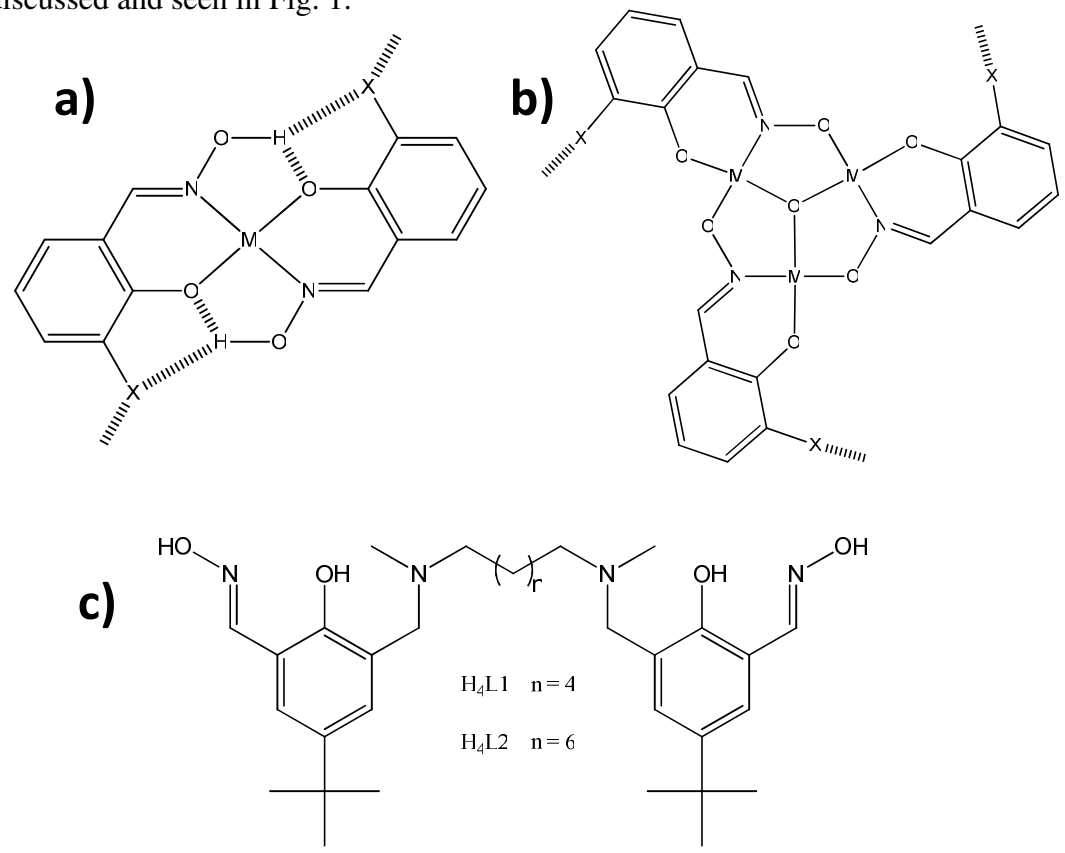

Fig. 1 (a) The planar mononuclear complex [M(saoH)$_2$] with 2-fold symmetry relating the X-substituents of the salicylaldoximate(-1) units. (b) Structure of the ligands H_4L1 and H_4L2. (c) The planar trinuclear complex [$M^{III}_3O(sao)_3]^+$ of trivalent metal cations with 3-fold symmetry relating the X-substituents of the salicylaldoximate(-2) units.

Copper(II) and nickel(II) form cages with *pseudo* 2-fold symmetry (Fig. 2a), which tightly and selectively bind anions (X) in the protonated cavities.[11] Here we consider the formation of higher nuclearity complexes [of Fe(III) and Mn(III)] using the strapped ligands H_4L1 and H_4L2 (Fig. 1c). One of the features of interest is the extent to which the length and flexibility of the straps control the approach of triangular units to each other (*i.e.* the cavity size) and the how this in turn influences the ability of the molecule to accommodate anions and/or paramagnetic metal ions that can modify the magnetic exchange between triangles, as shown schematically in Fig. 2b.

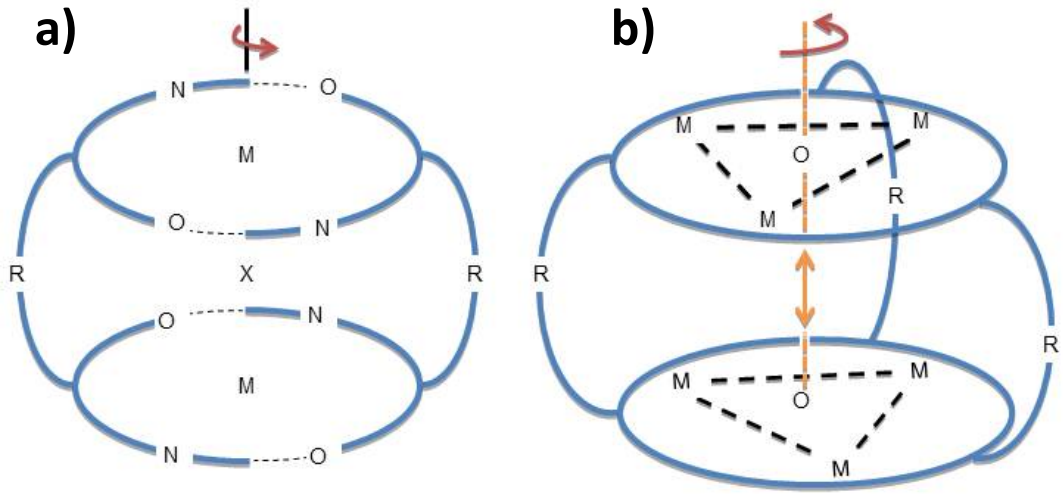

Fig. 2 Cage structures with 2-fold symmetry (a) which encapsulate anions when the straps (R) are protonated α,Ω-aminomethylalkanes. Structures with 3-fold symmetry (b) in which the separation of the trinuclear metal units is related to the twist about the 3-fold axis allowed by the flexible α,Ω-diaminomethylalkane straps.

4.2 Experimental

4.2.1 Syntheses

All manipulations were performed under aerobic conditions using chemicals as received, unless otherwise stated.

H_4L1 [N,N'-dimethyl-N,N'-hexamethylenedi(3-hydroxyiminomehyl-2-hydroxy-5-*tert*-butylbenzylamine)] was prepared as described in the literature.[12]

H_4L2 [N,N'-Dimethyl-N,N'-octamethylenedi(3-hydroxyiminomehyl-2-hydroxy-5-*tert*-butylbenzylamine].

To a mixture of potassium hydrogen carbonate (1.550 g, 15.5 mmol) and N,N'-dimethyl-1,8-octanediamine (0.946 g, 5.5 mmol) in acetonitrile (60 ml) was added an acetonitrile solution (60 ml) of 3-bromo-5-tertbutylsalicylaldehyde (3.186 g, 11.8 mmol) under nitrogen. The mixture was put under reflux for 16 hours to produce a yellow solution with white precipitate. The precipitate was filtered and the filtrate concentrated on a rotary evaporator, before being loaded into a silica gel column and eluted with 50% ethyl acetate/n-hexane. The first yellow band was collected and reduced to dryness to give the dialdehyde precursor as an orange oil. The oil was dissolved in absolute ethanol (50 ml) to give a yellow solution, to which was added freshly generated hydroxylamine - prepared from hydroxylamine hydrochloride (0.941 g, 13.5 mmol) and potassium hydroxide (0.712 g, 12.7 mmol) in absolute ethanol (60 ml). The mixture was put under reflux for 6 hours and then filtered. The resulting white precipitate was filtered, washed with (i) water, (ii) ice-cold ethanol, (iii) diethylether and then dried under reduced pressure. Yield = 2.301 g, 72 %. LRMS(FAB+): $[M+H]^+$ calc. for $C_{34}H_{55}N_4O_4$ 583.42; found 583.30. NMR: ^{1}H NMR (DMSO- d_6, 500 MHz): δ 1.27 (m, 22H, C**H**$_2$CH$_2$CH$_2$CH$_2$N, (C**H**$_3$)$_3$C), 1.28 (m, 4H, CH$_2$C**H**$_2$CH$_2$CH$_2$N), 1.51 (m, 4H, CH$_2$CH$_2$C**H**$_2$CH$_2$N), 2.23 (s, 6H, C**H**$_3$N), 2.44 (t, 4H, $^3J_{HH}$ = 7.3 Hz), 3.69 (s, 4H, NC**H**$_2$Ar), 7.18, 7.50 (d, 4H, $^4J_{HH}$ = 2.4 Hz, Ar-**H**), 8.32 (s, 2H, C**H**NOH). ^{13}C NMR (DMSO- d_6, 125 MHz): δ 26.1, 26.4, 28.6 ((**C**H$_2$)$_3$CH$_2$N), 31.1 ((**C**H$_3$)$_3$C), 33.6 ((CH$_3$)$_3$**C**), 40.8 (**C**H$_3$N), 56.0 ((CH$_2$)$_3$**C**H$_2$N), 59.1 (Ar**C**H$_2$N), 117.6, 121.1, 122.8, 126.8, 140.6, 145.4 (Ar-**C**), 153.5 (**C**HNOH).

CHN: calculated (found) for $C_{34}H_{54}N_4O_4$: C: 70.07 (69.57), H: 9.34 (9.09), N 9.61 (9.51).

$[Fe_7O_2(OH)_6(H_2L1)_3(py)_6](BF_4)_5 \cdot 6H_2O \cdot 14MeOH$ (**23**·$6H_2O$·14MeOH).

$Fe(BF_4)_2 \cdot 6H_20$ (338 mg, 1 mmol) and H_4L1 (277 mg, 0.5 mmol) were dissolved in MeOH (25 ml) and after 5 minutes stirring pyridine (2 ml) was added. The dark red solution was stirred for a further 180 minutes then filtered and left to evaporate slowly. X-ray quality crystals were produced after 3 days with an approximate yield of 30%. Elemental Analyses, calculated (found) for $C_{129}H_{198}B_5F_{20}Fe_7N_{18}O_{29}$ (**1**·$6H_2O$·3MeOH): C: 47.09 (46.64), H: 6.07 (5.59), N: 7.66 (7.88). BF_4^- content: anion content was determined to be five BF_4^- ions per cluster by performing ion exchange chromatography on a Dionex ICS-1100 chromatography system with data analysis by Chromeleon software package. All equipment and parts were supplied by Dionex. The system utilises 4.5 mM sodium carbonate/1.4 mM sodium hydrogen carbonate eluent and 4-mm IonPac AS-22 anion exchange column was chosen for the analysis. The column temperature was set at 30 °C, flow rate at 1.2 mL/min, and a sample size of 25 µL. Detection method was by suppressed conductivity with a 4-mm ASRS 300 suppressor. Chromeleon version 6.8.

$[Fe_6O(OH)_7(H_2L2)_3](BF_4)_3 \cdot 4H_2O \cdot 9MeOH$ (**24**·$4H_2O$·9MeOH).

$Fe(BF_4)_2 \cdot 6H_20$ (338 mg, 1 mmol) and H_4L2 (291 mg, 0.5 mmol) were dissolved in MeOH (25 ml) and after 5 minutes stirring pyridine (2 ml) was added. The dark red solution was stirred for a further 180 minutes then filtered and left to evaporate slowly. X-ray quality crystals were produced after 3 days with an approximate yield of 30%. Elemental Analyses, calculated (found) for $C_{111}H_{207}B_3F_{12}Fe_6N_{12}O_{33}$ (**2**·$6H_2O$·3MeOH): C: 47.05 (46.96), H: 7.36 (6.97), N: 5.93 (6.31).

$[Mn_6O_2(OH)_2(H_2L1)_3(py)_4(MeCN)_2(NO_3)](BF_4)_5 \cdot 3MeCN \cdot H_2O \cdot 5py$

(**25**·3MeCN·H_2O·5py).

$Mn(NO_3)_2 \cdot 4H_2O$ (126 mg, 0.5 mmol), H_4L1 (139 mg, 0.25 mmol) and $NaBF_4$ (110 mg, 1 mmol) were dissolved in MeCN (25 ml). After full dissolution to a yellow/brown solution, pyridine was added (2 ml) and the subsequent dark green solution stirred for 2 hours. The resulting solution was then diffused with Et_2O and X-ray quality crystals were produced after 4 days with an approximate yield of 25%. Elemental Analyses, calculated (found) for $C_{151}H_{208}B_5F_{20}Mn_6N_{27}O_{20}$ (**3**·3MeCN·H2O·5py) C: 52.04 (52.34), H: 6.02 (5.69), N: 10.85 (10.68).

4.2.2 Physical Measurements

Elemental analyses (C, H, N) were performed by the EaStCHEM microanalysis service. Variable temperature magnetic susceptibility measurements were made on powdered polycrystalline samples restrained in eicosane using a Quantum Design MPMS-XL SQUID magnetometer equipped with a 7 T magnet. Diamagnetic corrections were applied using Pascal's constants. Single crystal X-ray crystallography was performed using a Bruker Smart Apex CCD diffractometer equipped with an Oxford Cryosystems LT device, using Mo-Kα radiation. Data collection parameters and structure solution and refinement details are listed below. Full details can be found in the CIF files provided on the attached CD.

Crystal data for (**23**·6H_2O·14MeOH): $C_{140}H_{242}B_5F_{20}Fe_7N_{18}O_{40}$, M = 3642.50, Dark Red Rod, 0.15 x 0.08 x 0.06 mm, monoclinic, space group $P2_1/n$, a =16.9480(11), b = 32.864(2), c = 31.135(2) Å, β = 94.336(4)°, V=17291.7(20)Å^3, Z=4, Bruker Apex II CCD, Mo-Kα radiation, λ=0.71073Å, T=150(2)K, 2θmax=53.006°, 110344 reflections collected, 36222 unique (Rint = 0.106). Final GooF = 1.0984, R_1 =0.1166, wR2=0.1115, R indices based on 17942 reflections with I > 2σ(I) (refinement on F^2). The "SQUEEZE procedure[13] has been used to treat the solvent and the remaining BF_4^- anion region. 1142 e-/cell were found therefore 285 e-/cluster unit had to be assigned to solvent molecules as thirteen MeOH, one water (244 e-) plus one BF_4 (41 e-).

Crystal data for (**24**·4H_2O·9MeOH): $C_{111}H_{207}B_3F_{12}Fe_6N_{12}O_{33}$, M = 2821.28, Black Block, 0.16 x 0.25 x 0.27 mm, trigonal, space group *R-3c*, a, b =26.5317(4), c = 101.306(2) Å, V=61758.3(19)Å^3, Z=18, SuperNova, Dual, Cu at zero, Atlas, Cu-Kα radiation, λ=1.5418Å, T=100(2)K, 2θmax=51.6473°, 115307 reflections collected, 7558 unique (Rint = 0.1257). Final GooF = 1.0511, R_1 =0.1468, wR2=0.1769, R indices based on 6609 reflections with I > 2σ(I) (refinement on F). The "SQUEEZE procedure[13] has been used to treat the solvent region. 2981 e-/cell were found therefore 165 e-/cluster unit had to be assigned to solvent molecules as nine MeOH (162 e-).

Crystal data for (**25**·3MeCN·H2O·5py): $C_{151}H_{208}B_5F_{20}Mn_6N_{27}O_{20}$, M = 3485.07, Black block, 0.09 x 0.11 x 0.11 mm, monoclinic, space group *P2$_1$/c*, a = 32.9404(6), b = 18.7090(3), c = 28.3771(5) Å, β= 111.947(2)°, V= 16220.9(6) Å^3, Z=4, SuperNova, Dual, Cu at zero, Atlas, Cu-Kα radiation, λ=1.5418Å, T=100(2)K, 2θmax= 73.724°, 94960 reflections collected, 31620 unique (Rint = 0.042). Final GooF = 1.0970, R_1 =0.1377, wR2=0.1548, R indices based on 19343 reflections with F>4σ(F) (refinement on F^2). The "SQUEEZE procedure[13] has been used to treat the solvent region. 859 e-/cell were found therefore 212 e-/cluster unit had to be assigned to solvent molecules as five pyridine molecules (210 e-).

4.3 Results and Discussion

The new clusters **23**-**25** have the expected architectures shown in Fig 2b. Whilst they all contain two μ_3-oxo trinuclear units linked by three ligand straps, there are significant differences in their dispositions. These differences, which are compared in the conclusions section, can be characterised by the parameters in Table 1: (i) the variations in the distance between the central μ_3-oxygen atoms, (ii) the extents to which the units are parallel to each other, (iii) the extents to which the two triangular units are twisted relative to one another and (iv) whether the cavities between them are large enough to accommodate an additional metal ion and additional ligands bridging this to the metals ions in the triangular faces.

	23	**24**	**25**	**26**
μ_3-O…μ_3-O distance (Å)	6.920	2.526	5.188	7.237
Angle between least square planes defined by the μ_3-OM_3 units (°)	2.8	0.3	34.7	3.4
Twist angles M-O…O-M defined by the phenolate oxygen atoms in strapped ligands	68.7 69.6 68.6	111.2[a] 114.1[a] 114.1[a]	95.7 103.1 97.2	59.2 59.1 59.3
Mean value	69.0	113.1	98.6	59.2

Table 1. Parameters defining the shapes of the clusters **23** – **26**. [a]The ligand straps in this cluster do not define the shortest Fe…Fe distances between atoms in the two triangular faces (see Fig 4) but instead span diagonals of the rectangular faces of the trigonal prism. The Fe-O…O-Fe twist angles associated with the *sides* of the rectangles linking the triangular face are 5.42, 7.62 and 7.62°.

The reaction of $Fe(BF_4)_2{\cdot}6H_2O$ and H_4L1 in MeOH/py solvent mixture produces dark red/black crystals of complex **23** that are in the monoclinic space group *P2₁/n*. The metallic skeleton of the cation of **23** (Fig. 3) describes a $[Fe^{III}_3]_2$ trigonal antiprism consisting of two $[Fe^{III}_3(\mu_3\text{-}O)]^{7+}$ triangles linked centrally through the presence of a $[Fe(OH)_6]^{3-}$ moiety ($Fe_{triangle}$-OH-$Fe_{central}$, 133.37-135.75º) and peripherally by three helically twisted phenolic oxime ligands. Each oxime moiety bridges in a η^1: η^1: η^2: μ-mode along the edges of the $[Fe_3(\mu_3\text{-}O^{2-})]^{7+}$ triangles (Fe-N-O-Fe, 2.57-20.68°) in a fashion entirely analogous to that previously seen for

salicylaldoximate-bridged [Mn^{III}_3] and [Mn^{III}_6] clusters.[14-17] The "doubled-headed" oximes are present as H_2L^{2-} in which the oximic and phenolic O-atoms are deprotonated and the amino N-atoms protonated. The N-atoms H-bond to three H_2O molecules which fill the remaining available space within the central cavity of the cluster (N...O, 2.849-2.969 Å), with the latter further H-bonding to both the central OH^- ions and the oximic O-atoms (2.770-2.891 Å). The helical twisting of the organic strap linking the two bridging head groups results in a staggered antiprismatic arrangement of the iron atoms, with the planes of the two [Fe_3O] triangles sitting approximately parallel to each other (Fig. 3 and Table 1). The distance between the two mean planes of the [Fe^{III}_3] triangles is approximately 6 Å and the distance between the [Fe^{III}_3] triangles and the central Fe^{III} ion is ~3 Å. The O^{2-} ions do not sit directly in the [Fe_3] triangular planes, but instead are displaced (0.352, 0.318 Å) out of the plane, pointing away from the centre of the molecule. The six axial coordination sites on the faces of the triangles are filled by pyridine solvent molecules, which complete the octahedral [O_4N_2] geometry at these Fe^{III} ions. The central iron atom has an approximately octahedral [O_6] donor set with Fe-O distances of 1.921± 0.014 Å and *trans* and *cis* O-Fe-O angles falling in the ranges 176.0(2) – 177.7(2) and 87.9(2) – 93.3(2)° respectively.

Charge balance is ensured by the presence of five BF_4^- ions per cluster. In the crystal the closest inter-cluster interactions occur between neighbouring H_2L1^{2-} ligands, with C…C distances of the order of ~4 Å.

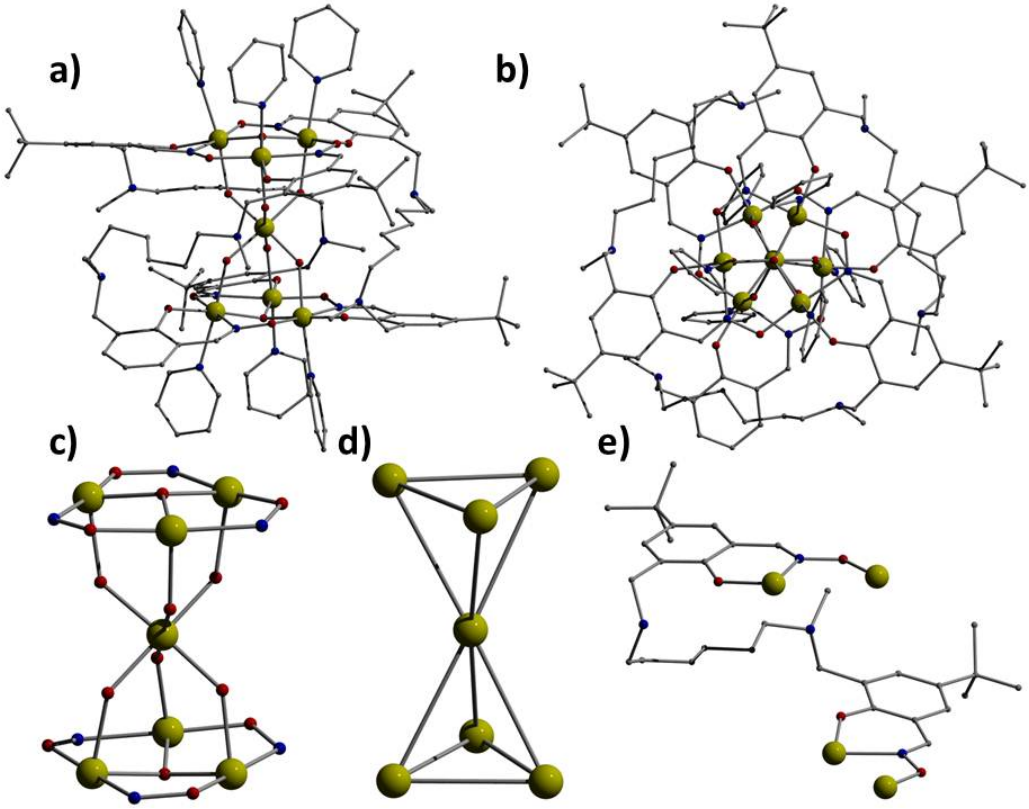

Fig. 3 Molecular structure of the cation of **23** viewed parallel (a) and perpendicular (b) to the [Fe_3] planes. The magnetic core (c) and the metallic skeleton (d). (e) The coordination mode of H_2L1^{2-}. Colour code: Fe = yellow, O = red, N = blue, C = grey. H-atoms and anions omitted for clarity.

If the reaction that produced **23** is repeated, but employing H_4L2 instead of H_4L1 the related complex $[Fe_6O(OH)_7(H_2L2)_3](BF_4)_3$ (**24**) is formed (Fig. 4). Interestingly the use of a longer, more flexible strap produces a smaller cluster in which the central cavity-filling Fe^{III} ion is no longer present. **24** crystallises in the trigonal space group *R-3c* with the metallic skeleton comprising a $[Fe^{III}_3]_2$ triangular prism. The two [Fe_3] triangles are not fully eclipsed, having Fe-O…O-Fe dihedral angles in the range ~5-8°. The two triangles are linked to each other *via* a total of six OH^- bridges (Fe-O-Fe, 102-104°), two on each vertex, and three helical H_2L2^{2-} ligands. The six OH^- ions form an internal hexagon with O…O distances of ~2.4 Å between atoms bridging the same two Fe atoms and ~2.7 Å between neighbouring pairs. The coordination mode of the phenolic oxime ligands are exactly the same as

that seen for H_2L1^{2-} in complex **23** (Fe-N-O-Fe, 15.87-26.33), although the twisting of the strap between the triangles is somewhat different. This is best observed when viewing the complex perpendicular to the two triangular faces of the prism (Fig. 4b). For **24** the atoms bridging across each edge in the "upper" triangle follow the clockwise sequence Fe-N-O-Fe. In the lower triangle the atom sequence is reversed, Fe-O-N-Fe. This contrasts to complex **23** in which the Fe-N-O-Fe clockwise sequence is observed for both triangles. Again the μ_3-O atoms at the centre of the [Fe_3] triangles are displaced from the [Fe_3] plane (0.317 Å), but this time they point inwards, toward the "empty" cavity between the two [Fe_3] triangles and the six OH^- ions. The distance between these two O-atoms is just 2.526 Å, suggesting the presence of a shared proton and thus a $[O\ldots H\ldots O]^{3-}$ unit. Indeed this is confirmed by BVS calculations which reveal a value of ~1.5 for each O-atom. The result is that the bridging -N-O- moieties from the H_2L2^{2-} ligands are now also displaced out of [the other side of] the [Fe_3] plane by approximately 1.3 Å, and there are no terminally coordinated pyridine ligands. This is in contrast to complex **23** in which the -N-O- moieties and [Fe_3] triangles are co-planar. Each Fe^{III} ion thus has a [O_5N] donor set and lies in distorted octahedral geometry. The N-atoms in the straps are again protonated and each H-bond to a phenolic O-atom (O…O, ~3 Å) and to a water molecule of crystallisation (N…O, 2.749 – 2.848 Å) that lies in the bowl-shaped cavities formed from the puckered phenolic oxime head groups. The latter also H-bond to both the oximic and phenolic O-atoms (O…O, ~2.56 – 2.98 Å). The distance between the two [Fe_3] mean planes is ~3 Å. Charge balance is maintained by the presence of three BF_4^- ions per cluster.

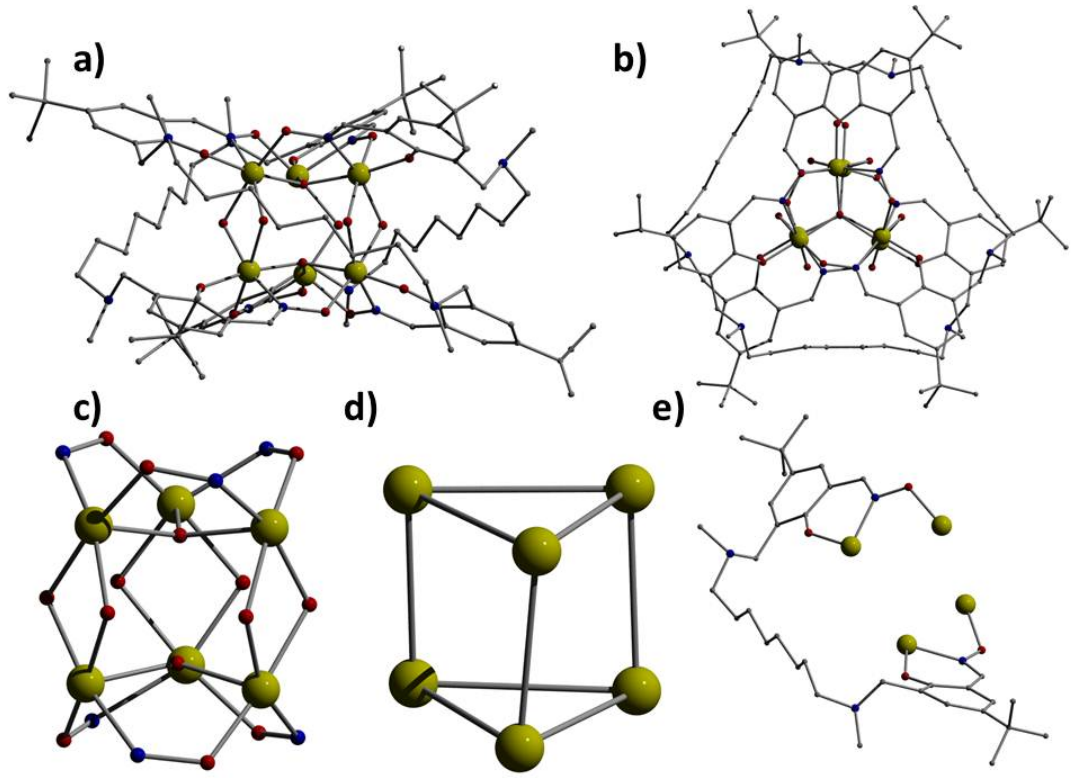

Fig. 4 Molecular structure of the cation of **24** viewed parallel (a) and perpendicular (b) to the [Fe_3] planes. The magnetic core (c), and the metallic skeleton (d). (e) The coordination mode of H_2L2^{2-}. Colour code as Fig. 3.

There are numerous close contacts between adjacent cluster cations, with the closest intermolecular interactions between N- and C-atoms on neighbouring H_2L2^{2-} ligands (~3.6 – 3.9 Å). The cluster cations pack in layers down the *c*-axis, with each [Fe_6] cluster forming a [Fe_6]$_3$ wheel with its two neighbouring clusters in the *ab*-plane. The BF_4^- anions reside both within the cavity formed at the centre of this wheel and in the planes between the layers of clusters. The result is the formation of an aesthetically pleasing honeycomb-like framework when viewed down the *c*-axis (Fig. 5).

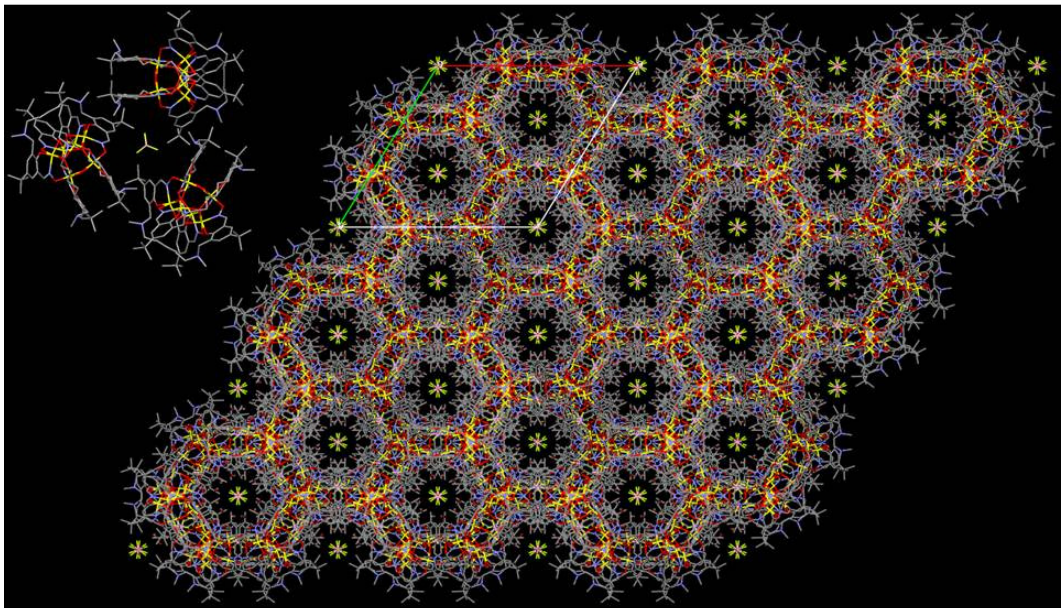

Fig. 5 The packing of **24** in the crystal viewed down the c-axis. The inset (top left) shows the triangular wheel motif the cluster cations form with their two nearest neighbour clusters.

The reaction of $Mn(NO_3)_2{\cdot}4H_2O$, H_4L1 and $NaBF_4$ in MeCN produces green/black crystals of $[Mn^{III}_6O_2(OH)_2(H_2L)_3(py)_4(MeCN)_2(NO_3)](BF_4)_5{\cdot}3MeCN{\cdot}H_2O{\cdot}5py$ (**25**·$3MeCN{\cdot}H_2O{\cdot}5py$) that are in the monoclinic space group $P2_1/c$. The metallic skeleton of the cationic cluster describes a very distorted trigonal prism, with the molecule perhaps better described as possessing a clam-shell like structure (Fig. 6) consisting of two $[Mn_3O]^{7+}$ triangles linked to each other through two hinge-like OH^- ions (Mn-O-Mn, 141.39º, 145.54º; Mn-O, 2.158-2.315 Å) and three helical H_2L1^{2-} ligands. Each phenolic oxime moiety bridges in a η^1: η^1: η^2: μ-mode along the edges of the $[Mn^{III}_3(\mu_3\text{-}O^{2-})]^{7+}$ triangles, in a manner identical to that observed for **23** and **24**. The planes of the two $[Mn_3O]$ triangles sit at an angle of ~34.5º with respect to each other (Fig. 6), with the metal atoms twisted [Mn-O…O-Mn] by approximately ~21° away from a trigonal prismatic arrangement – as can be seen when viewing the molecule perpendicular to the $[Mn_3O]$ planes.

As for complex **24**, the atoms bridging across each edge in the "upper" triangle follow the clockwise sequence Mn-N-O-Mn, with the sequence reversed, Mn-O-N-Mn in the "lower" triangle. The O^{2-} ions are displaced out of the $[Mn_3]$

plane (0.219, 0.224 Å). The "upper" and "lower" coordination sites on the triangular faces pointing away from the central cavity are occupied by a combination of terminally bonded py (x4) and MeCN (x2) molecules.

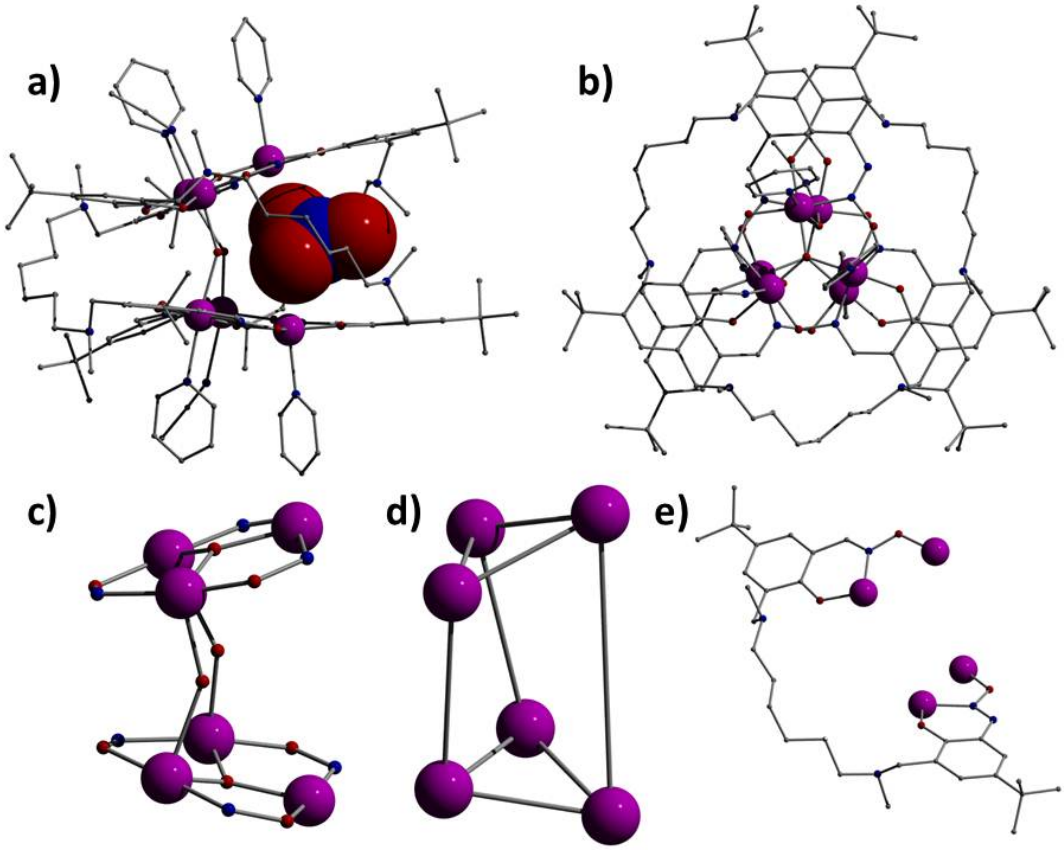

Fig. 6 Molecular structure of the cation of **25** viewed parallel (a) and perpendicular (b) to the [Fe_3] planes. The magnetic core (c), and the metallic skeleton (d). (e) The coordination mode of H_2L1^{2-}. Colour code as Fig. 3. Mn = purple.

The four Mn ions at the hinge of the clamshell are six-coordinate and in distorted octahedral geometries with the Jahn-Teller axes defined by the N(solvent)-Mn-OH(hinge) vector. The two Mn ions at the open end of the clamshell are five-coordinate and square-based pyramidal in geometry with four short equatorial bonds and one long axial bond to the N-atom of a py molecule (Mn…N, 2.188, 2.252 Å). The vacant "inner" coordination sites result in the presence of a cavity between the planes that has an approximate volume of ~60 $Å^3$ and which is occupied by a single NO_3^- anion. A space-filling representation (Fig. 6a) clearly shows this to be a good fit to the cavity size. The O-atoms of the NO_3^- anion are H-bonded to the OH^- hinges

(O…O, ~2.75 Å) and to the protonated amino N-atom of the organic strap (O…N, ~2.96 Å), with the latter also H-bonded to the terminally bonded phenolic O-atoms (~2.78 Å). They are also in close proximity to the phenolic and oximic O-atoms of the H_2L^{2-} ligands (O…O, ~2.85 Å) above and below. The inter-triangular metal-metal distances measure ~4.2 Å across the hinge and ~5.9 Å across the open face of the clam-shell. Charge balance is maintained by the presence of five BF_4^- anions per cluster. In the crystal the closest inter-cluster interactions occur between neighbouring H_2L1^{2-} ligands, with C…C distances of the order of ~4 Å, and *via* π…π stacking of adjacent py molecules. The clusters pack in regular sheets in the *ac* plane with the anions filling the spaces between these sheets.

Intriguing questions arise from the formation of complex **25**: a) why does the cluster form in a "squashed" clamshell topology in which the [Mn^{III}_3] triangles are relatively closely spaced and in which the organic straps are not "fully" extended? b) Why is a NO_3^- anion incorporated in the cavity when the "pocket" appears to be ideally sized for the introduction of a seventh metal(III) ion, as is the case in the Fe_7 system, **23**, especially since the cluster requires the presence of *six* counter anions for charge balance? It is possible that a Jahn-Teller distorted ion such as Mn(III) will not sit comfortably within an octahedral cavity of the type observed in **23** (see above) created by two antiprismatic [Mn_3O] triangles and it was more likely that a Mn(II) ion could be housed. We have previously shown that triangular face-capping Mn(II) ions can easily be added to oxime-based [Mn^{III}_3] triangles through the simple addition of N_3^-,[18] and indeed repetition of the reaction that produces **3** but in the presence of NaN_3 rather than $NaBF_4$ produces green/black crystals that are in the triclinic space group *P-1* of a complex formulated as $[Mn^{III}_6Mn^{II}O_2(N_3)_6(H_2L)_3(MeCN)_6]^{4+}$ (**26**) (Fig. 7). Unfortunately the X-ray data does not permit the identification of any counter ions and/or solvent molecules as the diffraction quality decreases very sharply below 1.0 Å of resolution. This is a clear indication of a very disordered structure although the connectivity of the cationic cluster could be clearly established as even the conformational disorder of one of the oximic ligands could be modelled. Repetition of the synthesis of the complex has

proven difficult, resulting in an inability to isolate, purify and analyse by other methods. Consequently we include only a brief description of the structure of the cation of **26**. The Mn_7 cluster (Fig. 8), like the Fe_7 system **23,** has an trigonal antiprismatic arrangement of the two $[M^{III}_3O]^{7+}$ triangles which are linked to each other through three greatly extended helical H_2L1^{2-} ligands. The extended columnar cavity is occupied by a single Mn(II) ion, linked to the upper and lower [Mn^{III}_3] triangles by six (end-on) μ-bridging N_3^- ions (Mn^{III}-N-Mn^{II}, ~121-131°). The coordination mode of the phenolic oxime ligands (Fig. 7e) is the same as that seen for H_2L1^{2-} in complex **23** in which the bridging ligands define twist angles of 59º between the triangular faces of the antiprism.

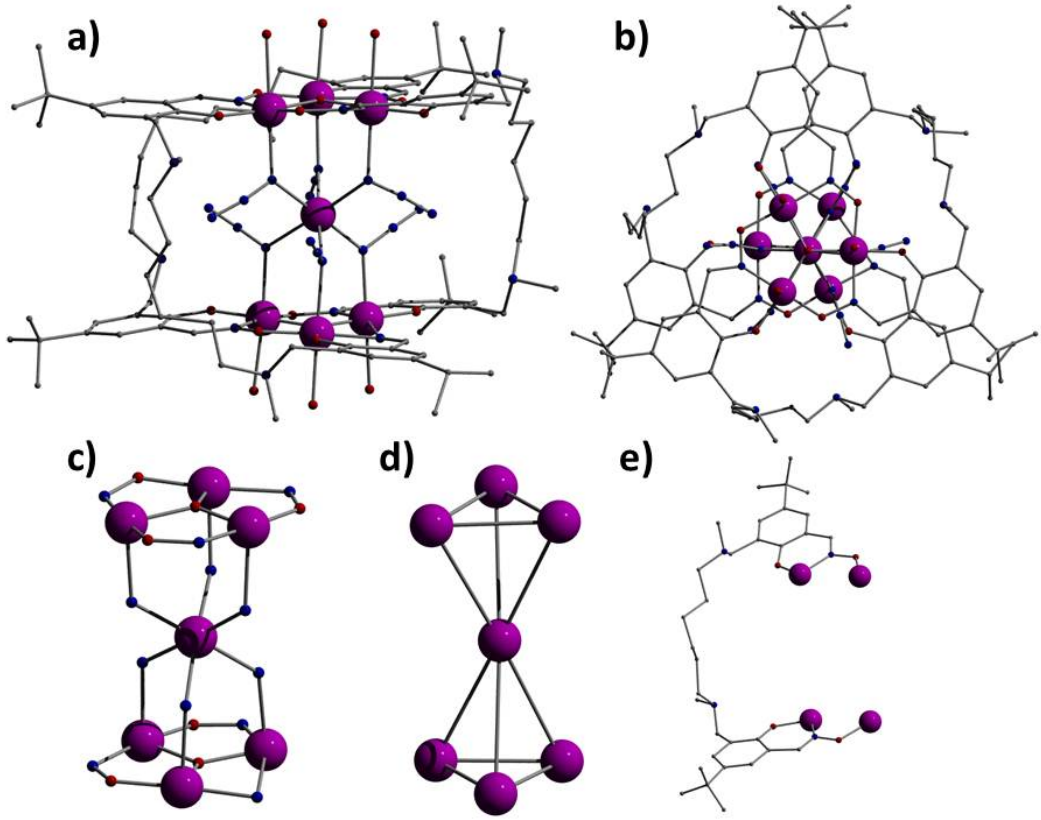

Fig. 7 Molecular structure of the cation **26** viewed parallel (a) and perpendicular (b) to the [Fe_3] planes. The magnetic core (c) and the metallic skeleton (d). (e) The coordination mode of H_2L1^{2-}.

The distance between the two mean planes of the co-planar [Mn^{III}_3] triangles of the upper and lower faces of the prism is ~7 Å, with the Mn(III) ions now fully

staggered (Mn-O-O-Mn, ~61°). All Mn ions have distorted octahedral geometries with the coordination sites on the faces of the [Mn_3] triangles completed by terminally bonded solvent molecules. The central Mn(II) ion has a [N_6] coordination sphere, coordination sphere with Mn-O distances of 2.137 ± 0.051 Å and *trans* and *cis* O-Mn-O angles falling in the ranges 177.31 – 179.49 and 87.33 – 92.92° respectively. The Mn(III) ions have [O_4N_2] donor sets with their Jahn-Teller extended axes perpendicular to the [Mn_3] triangles (N(azide)-Mn-O(solvent)).

4.4 Magnetism

The magnetic properties of **23**, **24** and **25** have been investigated by measuring the temperature-dependence of magnetic susceptibility χ (Fig. 8-10). All the compounds are characterized by a monotonic decrease of χT down to low temperatures suggesting the presence of sizeable antiferromagnetic (AF) interactions in all the compounds. Also the fact that the room-temperature value of χT is significantly smaller than that corresponding to non-interacting ions (especially in **23** and **24**) points to the presence of significant exchange couplings.

As a first approximation, the magnetic properties of **23**, **24** and **25** can be modelled by the isotropic Heisenberg spin Hamiltonian:

$$H = \sum_{i>j} J_{ij} \boldsymbol{S}_i \cdot \boldsymbol{S}_j + g\,\mu_B \boldsymbol{B} \cdot \sum_i \boldsymbol{S}_i \qquad (1)$$

(S_i = 5/2 for Fe^{3+} and S_i = 2 for Mn^{3+}). The last term accounts for the Zeeman interaction with the applied magnetic field *B*. The patterns of exchange constants are illustrated in the insets of Fig. 8-10. Being Fe^{3+} characterized by a half-filled d-electron shell, anisotropic exchange and crystal-field interactions in **23** and **24** are expected to be small and *H* should provide a very good description of these molecules. Conversely, further anisotropic terms could be important in **25**, especially to describe the low-temperature behaviour.

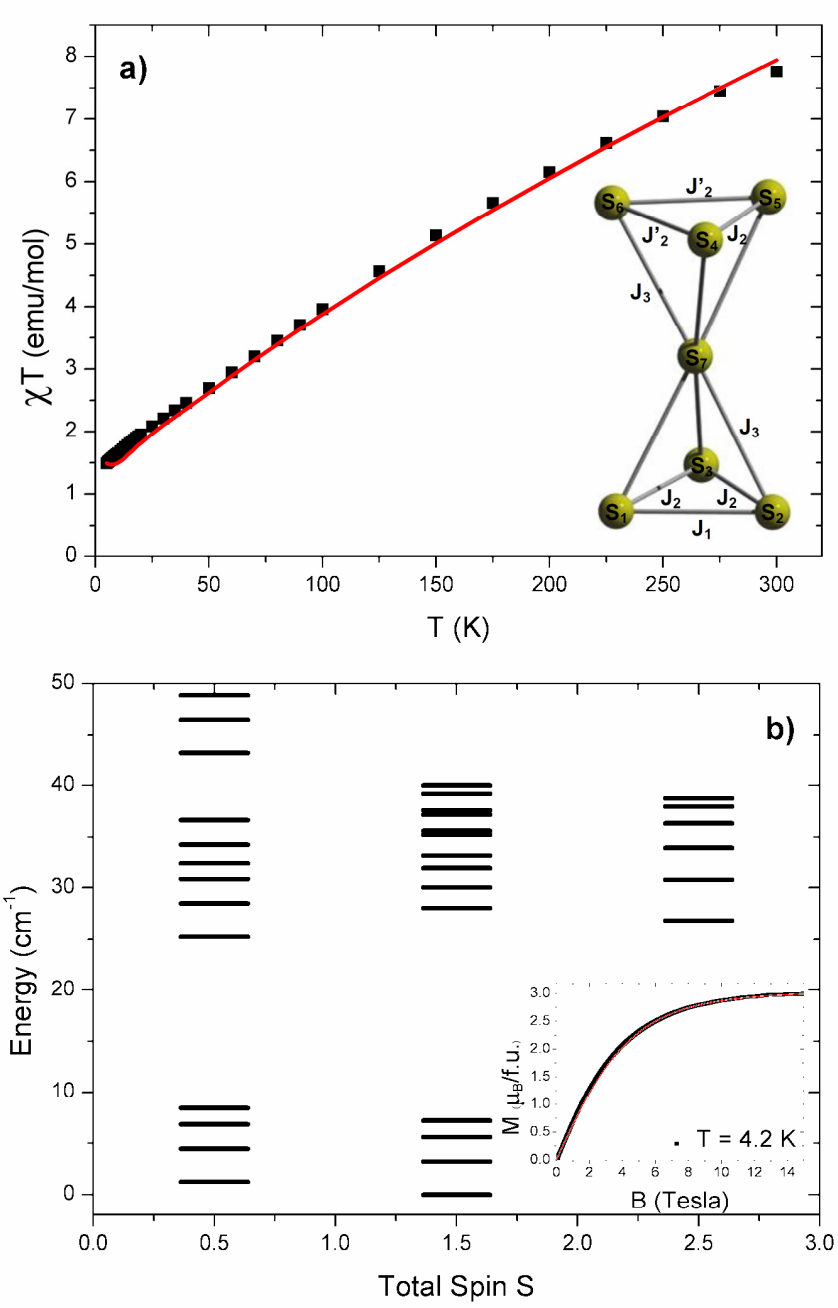

Fig. 8. a) Measured temperature dependence of the magnetic susceptibility of **23** reported as χT (black squares). The red line represents the calculation with J_1 = 55 cm^{-1}, J_2 = 61 cm^{-1}, J'_2 = 61.8 cm^{-1}, J_3 = 49.5 cm^{-1} and g = 2. Inset: schematic representation of the seven Fe^{3+} ions and of the exchange couplings. b) Exchange energy of the lowest total spin multiplets calculated with the spin Hamiltonian *H* and the above exchange constants. The ground state energy is set to zero. Inset: experimental field-dependence of the low temperature magnetization (black line) and that predicted by the model (red line). The fitting of the magnetic data within the present model is not unique. Hence, we have chosen a representative set of exchange constants characterized by the same hierarchy as the inverse of the Fe-Fe distances.

The simplest-conceivable models of these molecules are characterised by two exchange constants only, one describing intra-triangle exchange couplings and one describing the other bonds (see insets in Fig. 8-10), but these models are not adequate to describe the observed magnetic behaviour. Indeed, the structures of **23**, **24** and **25** allow for several distinct exchange parameters. In the following we assume simple models allowing to describe the temperature-dependence of magnetic susceptibility.

The low-T value of χT in **23** points to a low total-spin S ground state and to the presence of low-lying excited states (the measured value is smaller than that corresponding to an isolated S= 3/2 multiplet). Fig. 8 shows that magnetic measurements can be well reproduced by a model characterized by strong AF exchange couplings both within the upper and lower Fe triangles and between these triangles and the central Fe ion.

The presence of these competing interactions leads to a low-spin ground multiplet and to several low-lying excited manifolds (Fig. 8 b). The lowest S = 5/2 sextet is expected to be well separated in energy from the ground state as confirmed by the measured field-dependence of the magnetization which at low-T saturates to 3 μ_B until high fields (inset of Fig.8 b).

The low-temperature value of χT in **24** suggests a non-magnetic S= 0 ground state very close to a magnetic S= 1 triplet. The observed magnetic behaviour of **24** is reproduced by assuming strong AF couplings within the two triangles and weak inter-triangles interactions (see Fig. 9). Hence, also this system is characterized by the presence of competing interactions. The presence of strong AF interactions in both **23** and **24** explains the large room-temperature reduction of the effective moment in these compounds with respect to that of uncoupled ions. Fig. 9b shows that the present model is characterized by a singlet ground state and by an excited triplet well separated by the other excited levels (Fig. 9b).

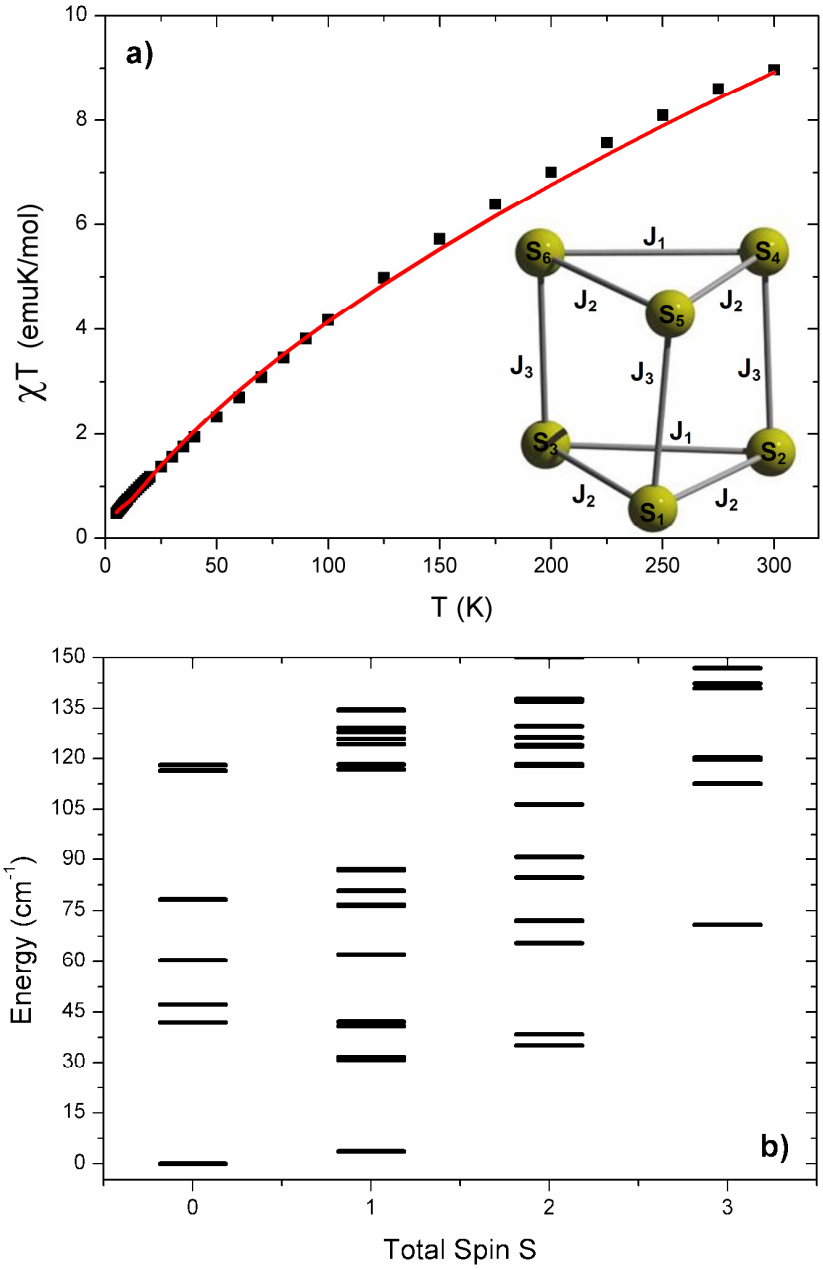

Fig. 9. a) Measured temperature dependence of the magnetic susceptibility of **24** reported as χT (black squares). The red line is obtained with J_1 = 43 cm^{-1}, J_2 = 56 cm^{-1}, J_3 = 0.6 cm^{-1} and g = 2. Inset: schematic representation of the six Fe^{3+} ions and of the exchange couplings. b) Exchange energy of the lowest total spin multiplets calculated with the spin Hamiltonian *H* and the exchange constants reported above. The ground state energy is set to zero.

The temperature-dependence of the magnetic susceptibility of **25** can be reproduced with Eq 1, as shown in Fig. 10a. The model is characterized by sizeable AF exchange interactions within the two Mn triangles and by vanishing couplings

between the triangles. The resulting energy of the lowest-lying multiplets is reported in Fig. 10b as a function of their total spin. The presence of low-lying magnetic states is necessary to account for the measured low-temperature susceptibility. As stated above, sizeable anisotropic interactions can be expected in **25**, but single-crystal measurements are needed to address this issue.

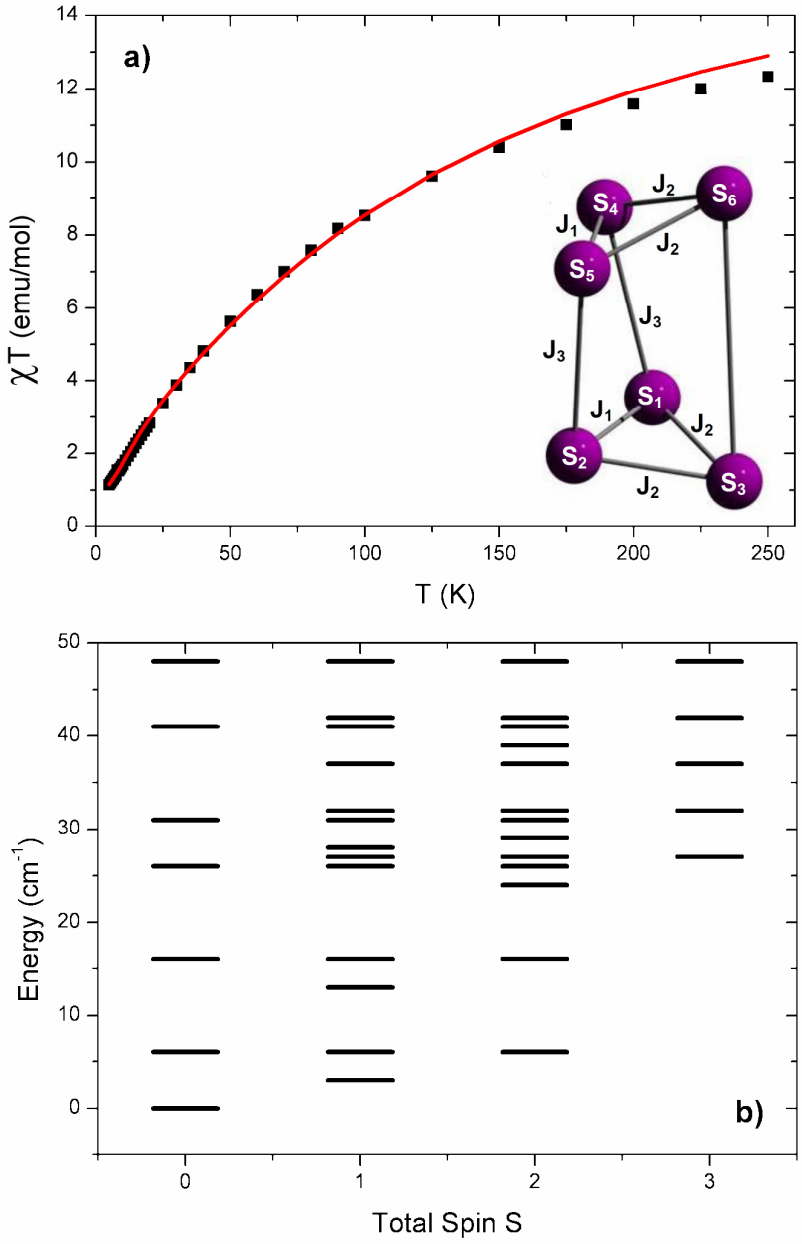

Fig. 10. a) Measured temperature dependence of the magnetic susceptibility of **25** reported as χT (black squares). The red line is calculated with J_1 = 18 cm^{-1}, J_2 = 13 cm^{-1}, J_3 = 0 cm^{-1} and g = 2. Inset: schematic representation of the six Mn^{3+} ions and of the exchange couplings. b) Exchange energy of the lowest total spin multiplets calculated with the spin Hamiltonian *H* and the above exchange constants. The ground state energy is set to zero.

4.5 Conclusions

The extent to which the structures of the clusters are controlled by the requirements of the strapped ligands, the metal ions' best use of bridging anions and the optimisation of forms of secondary bonding inside and outside the cavities containing the clusters can be compared using Table 1. The largest μ_3-O… μ_3-O separations are found in the Fe_7 and Mn_7 clusters, **23** and **26**, (6.920 and 7.237 Å). These allow the cavities defined by the triangular faces and the three aliphatic straps to accommodate $Fe(OH)_6^{3-}$ and $Mn(N_3)_6^{4-}$ units. These octahedral central bridging units transmit an approximately 60° twist to the two triangular μ_3-OM_3 units, resulting in an anti-prismatic arrangement with mean twist angles of 69° and 59°.

The shortest μ_3-O…μ_3-O distance, 2.526 Å, is present in the Fe_6 cluster, **24**. This allows each iron atom in one triangular face to form two μ_2 -OH bridges to an iron atom in the other triangular face (see Fig 4), and results in the two triangular μ_3-OFe_3 units forming a prismatic arrangement. Unlike the other clusters which contain H_2L1^{2-}, the longer straps of H_2L2^{2-} do not define the shortest Fe…Fe distances between atoms in the two triangular faces (see Fig 4). They span a rectangular face of the trigonal prism in such a way that the Fe-O…O-Fe twist angles defined by the phenolate oxygen atoms of strapped ligands approach 120°.

The Mn_6 cluster, **25**, is the least regular, principally because the two trianglar μ_3-OMn_3 units are not parallel. Their least squares planes are inclined at ~34.5°. Two Mn atoms in each triangular unit closely approach Mn atoms in the adjacent unit to form μ_2-OH bridges. The remaining Mn atoms in each triangle are more widely separated, accommodating a non-coordinated nitrate between them. It seems likely that this arrangement better suits the Jahn-Teller distorted Mn(III) atoms than the formation of a more compacted trigonal prism with six bridging hydroxides between the two triangular faces (as in the Fe^{III}_6 cluster, **24**) or of an extended trigonal antiprism with a bridging $Mn^{III}(OH)_6^{3-}$ unit between the two triangular faces (as in the Fe^{III}_7 cluster, **23**).

It is clear that the very flexible straps in the double headed phenolic oximes, H_4L1 and H_4L2, allow deprotonated forms to provide a range of clusters which can

be represented by the schematic structure shown in Fig 2b. Their flexibility appears to ensure that the clusters which are isolated meet the electronic requirements of the M(III) ions which are present in the key μ_3-OM_3 building blocks which define their pseudo C_3 symmetry.

4.6 References

1. D. Bradshaw, J. B. Claridge, E. J. Cussen, T. J. Prior and M. J. Rosseinsky, *Acc. Chem. Res.*, 2005, **38**, 273.
2. A. K. Cheetham, C. N. R. Rao and R. K. Feller, *Chem. Commun.*, 2006, 4780.
3. M. Eddaoudi, D. B. Moler, H. Li, B. Chen, T. M. Reineke, M. O'Keeffe and O. M. Yaghi, *Acc. Chem. Res.*, 2001, **34**, 319.
4. S. Kitagawa, R. Kitaura and S.-i. Noro, *Angew. Chem. Int. Ed*, 2004, **43**, 2334.
5. X. Lin, J. Jia, P. Hubberstey, M. Schroder and N. R. Champness, *CrystEngComm*, 2007, **9**, 438.
6. B. Moulton and M. J. Zaworotko, *Chem. Rev.*, 2001, **101**, 1629.
7. J. J. Perry IV, J. A. Perman and M. J. Zaworotko, *Chem. Soc. Rev.*, 2009, **38**, 1400.
8. D. J. Tranchemontagne, Z. Ni, M. O'Keeffe and O. M. Yaghi, *Angew. Chem. Int. Ed*, 2008, **47**, 5136.
9. P. A. Tasker, P. G. Plieger and L. C. West, *Comprehensive Coordination Chemistry II*, 2004, **9**, 759.
10. M. Wenzel, R. S. Forgan, A. Faure, K. Mason, P. A. Tasker, S. Piligkos, E. K. Brechin and P. G. Plieger, *Eur. J. Inorg. Chem.*, 2009, **2009**, 4613.
11. M. Wenzel, G. B. Jameson, L. A. Ferguson, Q. W. Knapp, R. S. Forgan, F. J. White, S. Parsons, P. A. Tasker and P. G. Plieger, *Chem. Commun.*, 2009, 3606.
12. P. G. Plieger, P. A. Tasker and S. G. Galbraith, *Dalton Trans.*, 2004, 313.
13. P. van der Sluis and A. L. Spek, *Acta Cryst.*, 1990, **46**, 194.
14. R. Inglis, L. F. Jones, C. J. Milios, S. Datta, A. Collins, S. Parsons, W. Wernsdorfer, S. Hill, S. P. Perlepes, S. Piligkos and E. K. Brechin, *Dalton Trans.*, 2009, **18**, 3403.
15. R. Inglis, C. J. Milios, L. F. Jones, S. Piligkos and E. K. Brechin, *Chem. Commun.*, 2011, *Advanced Article*. And references therein.
16. R. Inglis, S. M. Taylor, L. F. Jones, G. S. Papaefstathiou, S. P. Perlepes, S. Datta, S. Hill, W. Wernsdorfer and E. K. Brechin, *Dalton Trans.*, 2009, **42**, 9157.
17. C. J. Milios, S. Piligkos and E. K. Brechin, *Dalton Trans.*, 2008, 1809.
18. C. J. Milios, R. Inglis, L. F. Jones, A. Prescimone, S. Parsons, W. Wernsdorfer and E. K. Brechin, *Dalton Trans.*, 2009, 2812.

Chapter 5
Conclusions

The main aims of this thesis were to define how the nuclearity and structures of iron(III) clusters can be varied using simple phenolic oxime derivatives and "strapped" ligands in which two phenolic oximes are linked to assemble larger clusters from smaller components. The interest for the industrial partner was due to the potential use of polynuclear iron complexes as pigmentary materials and there is also a considerable interest in their magnetic properties and their formation when ligands of this type are used as corrosion inhibitors.

The synthetic work in the thesis has significantly extended the range of structural types of Fe^{III} polynuclear complexes of oxime ligands. Clusters containing 3 to 9 iron(III) atoms have been structurally characterised which contain doubly deprotonated phenolic oximes. The key building blocks in these clusters are the bridging N-O^- oximato unit and the triangular μ_3-oxo and tetrahedral μ_4-oxo $[Fe_3O]^{7+}$ and $[Fe_4O]^{10+}$ units. The structure of the isolated complex appears to be very dependent on the nature of the ketoxime group. Replacement of the phenyl group in the phenolic oxime in **2** with a less bulky methyl group allows isolation of clusters with a nuclearity of 3 to 8.

A new μ_4-coordination mode has been observed for the phenolic oxime in **10** and **11**. The range of polynucleating modes for phenolic oximates in complexes of iron(III) provides an explanation for why hydrophobic derivatives can protect lightly corroded iron surfaces by providing a very stable polymeric coating which prevents ingress of water or water borne reagents. The considerable variations in the nuclearity and core structures of the Fe^{III} clusters described in this thesis (see Table 2, pages 62-63) are not seen with Mn and similar ligands. The number of structurally characterised oxime structures of manganese is very large due to their use as SMMs but despite considerable variations in preparative conditions their structures are predominantly based on a $[Mn_3(R\text{-}sao^{2-})_3]^{3+}$ unit.

Introduction of co-ligands to the synthesis of clusters to compete with the phenolic oxime ligands for metal coordination sites extends the range of structures obtained. The structures are characterised by having more edge and vertex sharing

between the key $[Fe_3O]^{7+}$ and $[Fe_4O]^{10+}$ building blocks than those formed in the absence of co-ligands.

Using bifunctional phenolic oxime ligands in which two salicylaldoximes are linked by a flexible strap, failed to assemble very large clusters by crosslinking polynuclear units formed by "simple" phenolic oximes. Very interesting cage structures were formed instead in which two triangular $[Fe_3O]^{7+}$ units are brought together by three straps. These cages are capable of incorporating an additional Fe^{III} ion *via* μ–OH links to Fe atoms in the triangles. The isolation of these structures underlines the intrinsic stability of the $[M_3O]^{7+}$ unit and similar cage clusters were also formed by Mn^{3+}. The identity of the metal ion and the length of the straps connecting the salicylaldoxime units have a major impact on the nuclearity and topology of the resultant complex, with, perhaps counter-intuitively, the longer straps producing the "smallest" clusters.

The initial proposal of these complexes as pigmentary materials has been examined with limited results. The problem of yield could be solved by solid state synthesis and initial results could indicate that simply grinding two starting materials of iron(II) acetate and phenolic oxime ligand together could generate a polynuclear iron complex as the acetate is protonated and is expelled as acetic acid. IR results appear to show the formation of a polynuclear species but nothing conclusive. Attempts at recrystallising the solid product failed and further techniques such as mass spectrometry provided no successful evidence as it became clear there was a mixture of product and starting materials.

There is almost a limitless potential for synthesising further Fe-salicylaldoxime complexes when we start to introduce co-ligands. This thesis has identified the cores and common units which these structures will contain. Use of strapped ligands provides the most scope for future work as we have only employed very flexible straps with only minor differences - length. Continuing work will employ derivatives with more rigid straps in an attempt to control the cavity size and contents.